Chapter 11
Tire Models

The global mechanical behavior of the wheel with tire has been addressed in Chap. 2. Basically, we have first found a way to describe the kinematics of a wheel with tire. This effort has led to the definition of the tire *slips*, as quantities that measure how far a tire is from pure rolling conditions. Then, the forces and couples that a tire receives from the road have been defined. The final step has been to investigate experimentally the link between these kinematic parameters and forces/couples.

In Chap. 2 no attempt was made to analyze what happens in the contact patch. That is, how the forces and couples are built by the elementary actions that arise at each point of the contact patch. This kind of analysis, however, is quite relevant for a real comprehension of the subtleties of vehicle set-up.

In this chapter, what happens in the contact patch will be investigated by means of the so-called *brush model*. Great care will be devoted to clearly stating the assumptions on which this model is based. Moreover, the investigation will also cover the transient tire behavior. The final results are really interesting and enlightening.

11.1 Brush Model Definition

The *brush model* is perhaps the simplest *physical* tire model, yet it is quite significant and interesting. It is a tool to analyze qualitatively what goes on in the contact patch and to understand why the global mechanical behavior of a wheel with tire is, indeed, like in Figs. 2.22, 2.23, 2.24, 2.25, 2.26 and 2.27. Due to its simplicity,[1] the brush model is not always able to provide quantitative results. However, it is of great help in grasping some of the fundamental aspects of tire mechanics.

[1] Actually, the formulation presented here of the brush model is quite general, and hence it is a bit involved.

M. Guiggiani, *The Science of Vehicle Dynamics*,
https://doi.org/10.1007/978-3-319-73220-6_11

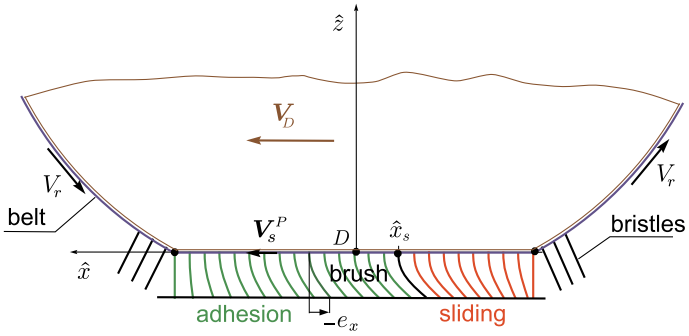

Fig. 11.1 Schematic of the brush model during braking (very important figure)

The Magic Formula, discussed in Sect. 2.12, provides curves that fit fairly well the experimental results, while the brush model attempts to describe the complex interaction between the tire and the road and how forces are generated. They are complementary approaches.

Basically, in the brush model, a belt equipped with infinitely many flexible bristles (the thread) is wrapped around a cylindrical rigid body (the rim), which moves on a flat surface (the roadway). In a well defined area (the contact patch), the tips of the bristles touch the ground, thus exchanging with the road normal pressures p and tangential stresses $\mathbf{t}$, provided the bristles also have a horizontal deflection $\mathbf{e}$. Each bristle is undistorted ($\mathbf{e} = \mathbf{0}$) when it enters the contact patch. A schematic of the brush model is shown in Fig. 11.1.

The brush model, as any mathematical model, relies on very many assumptions, more or less realistic. An attempt is made to clearly establish all of them, so that the impact of possible improvements can be better appreciated.

For generality, the model is first formulated for *transient conditions*. Steady-state behavior follows as a special case. The simplest case of translational slip only is discussed in Sect. 11.5.

11.1.1 Roadway and Rim

The *brush model*, like the tire, is something that connects the rim to the road. The roadway is assumed to be perfectly *flat*, like a geometric plane. The rim is modelled like a non-rolling cylindrical rigid body moving on the road, carrying on its outer surface a belt equipped with infinitely many flexible bristles (like a brush), which touch the road in the contact patch (Figs. 11.1 and 11.2). To simulate the rolling of the wheel, the belt slides on the rigid body with speed V_r (i.e., the rolling velocity defined in (2.53)).

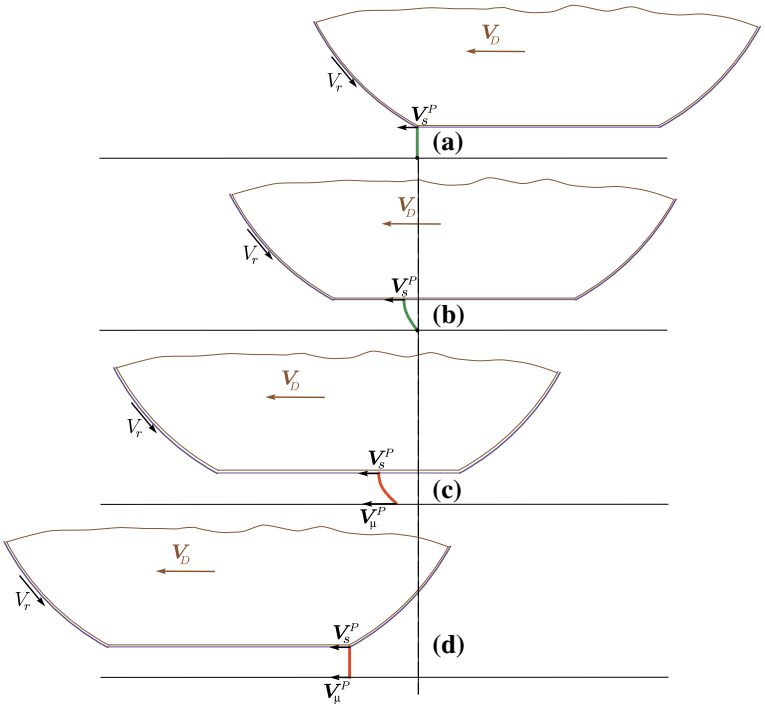

Fig. 11.2 Four sequential positions of the same bristle during braking ($|\mathbf{V}_D| > V_r$): **a** undeformed at the leading edge; **b** with growing deflection due to the tip stuck to the ground; **c** with lowering deflection with tip sliding on the ground; **d** undeformed at the trailing edge, with tip sliding on the ground

11.1.2 Shape of the Contact Patch

As shown in Fig. 11.3, the contact patch $\mathscr{P}$ is assumed to be a convex, simply connected region. Therefore, it is quite different from a real contact patch, like the one in Fig. 2.4 at p. 11, which usually has lugs and voids.

It is useful to define a reference system $\hat{\mathsf{S}} = (\hat{x}, \hat{y}, \hat{z}; D)$ attached to the contact patch, with directions ($\mathbf{i}$, $\mathbf{j}$, $\mathbf{k}$) and origin at point D. Usually D is the center of the contact patch, as in Fig. 11.3. Directions ($\mathbf{i}$, $\mathbf{j}$, $\mathbf{k}$) resemble those of Fig. 2.6, in the sense that $\mathbf{k}$ is perpendicular to the road and $\mathbf{i}$ is the direction of the wheel pure rolling.

More precisely, the contact patch is defined as the region between the *leading edge* $\hat{x} = \hat{x}_0(\hat{y})$ and the *trailing edge* $\hat{x} = -\hat{x}_0(\hat{y})$, that is

$$\mathscr{P} = \{(\hat{x}, \hat{y}) : \hat{x} \in [-\hat{x}_0(\hat{y}), \hat{x}_0(\hat{y})], \hat{y} \in [-b, b]\} \tag{11.1}$$

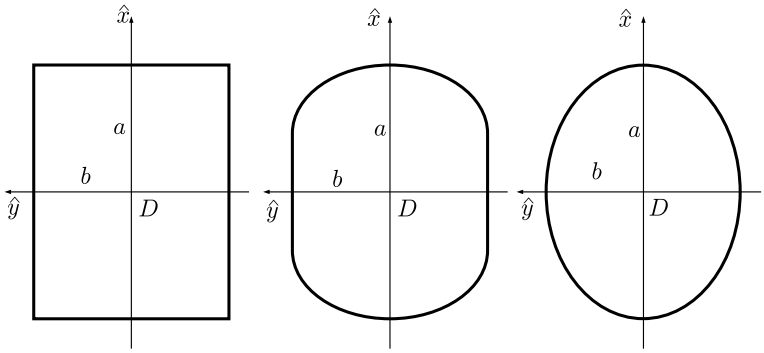

Fig. 11.3 Possible simple shapes of the contact patch

It is assumed for simplicity that the *shape* and *size* of the contact patch are not affected by the operating conditions, including the camber angle γ. Of course, this is not true in real tires.

For mathematical convenience, the contact patch is assumed here to be either a *rectangle*, centered at D, of length $2a$ and width $2b$ (Fig. 11.3, left), or an *ellipse*, again with axes of length $2a$ and $2b$ (Fig. 11.3, right). In the first case we have $\hat{x}_0 = a$, whereas in the second case

$$\hat{x}_0(\hat{y}) = \sqrt{a^2 \left(1 - \frac{\hat{y}^2}{b^2}\right)} \tag{11.2}$$

Typical values for a and b are in the range 0,04–0,08 m. The rectangular shape is not a bad approximation of the contact patch of car tires (Fig. 2.4), while the elliptical one is better for motorcycle tires (Fig. 11.5). Occasionally, also a rounded rectangular contact patch is considered, as in Fig. 11.11.

11.1.3 Pressure Distribution and Vertical Load

Figures 11.4 and 11.5 show a typical pressure distribution as measured in a real motionless tire. The average ground pressure in the tire contact patch, considered as a single region, is not much higher than the tire inflation pressure. Of course there are high peaks near the tread edges.

A very simple pressure distribution $p(\hat{x}, \hat{y})$ on the contact patch $\mathscr{P}$, which roughly mimics the experimental results, may be *parabolic* along $\hat{x}$ and *constant* along $\hat{y}$

$$p = p(\hat{x}, \hat{y}) = p_0(\hat{y}) \frac{(\hat{x}_0(\hat{y}) - \hat{x})(\hat{x}_0(\hat{y}) + \hat{x})}{\hat{x}_0(\hat{y})^2} \tag{11.3}$$

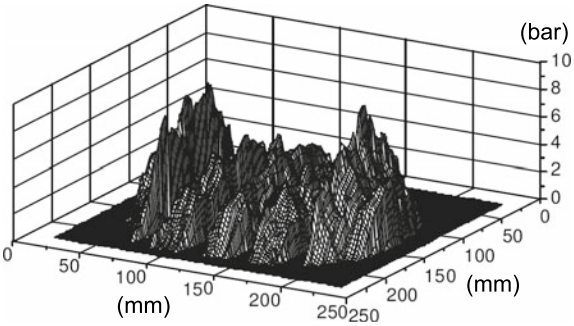

Fig. 11.4 Experimental results: pressure distribution for a motionless motorcycle tire [4]

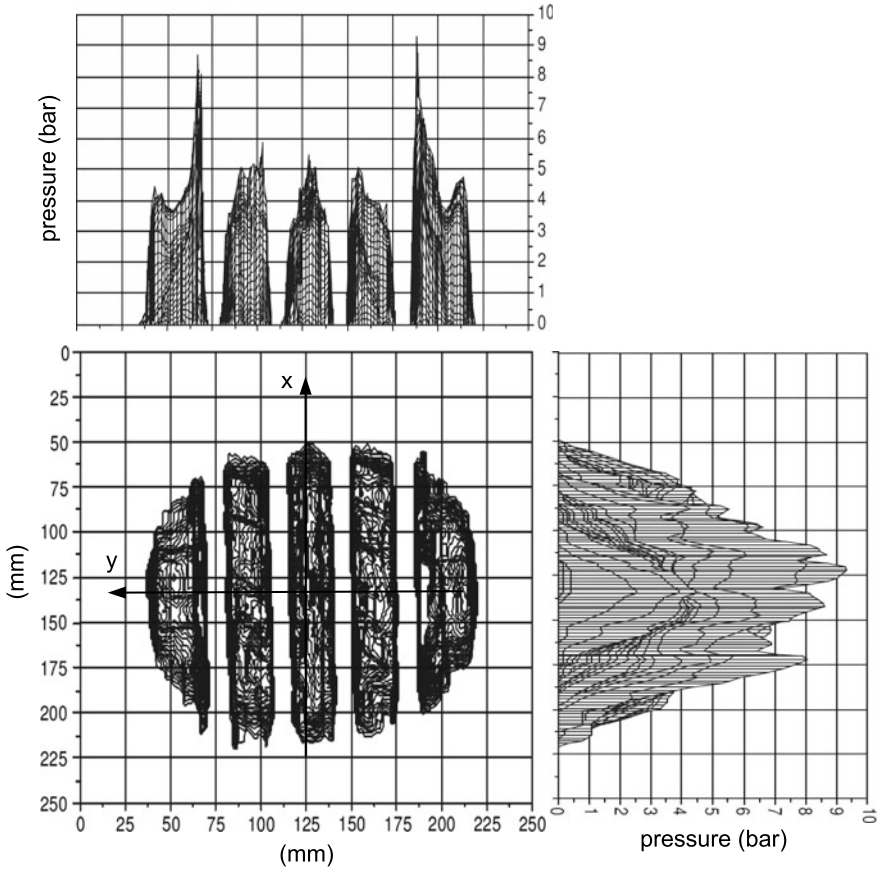

Fig. 11.5 Experimental results: contact patch and envelope of pressure distribution for a motionless motorcycle tire [4]

where $p_0(\hat{y}) = p(0, \hat{y})$ is the pressure peak value. The corresponding vertical load is given by

$$F_z = \int_{-b}^{b} \mathrm{d}\hat{y} \int_{-\hat{x}_0(\hat{y})}^{\hat{x}_0(\hat{y})} p(\hat{x}, \hat{y}) \mathrm{d}\hat{x} \tag{11.4}$$

Other pressure distributions may be used as well in the brush model, including nonsymmetric ones like in Fig. 2.12 to take into account the rolling resistance.

On a *rectangular* contact patch $\hat{x}_0(\hat{y}) = a$. Equation (11.3), with the same p_0 for all $\hat{y}$, becomes simply

$$p = p(\hat{x}, \hat{y}) = p_0 \left[1 - \left(\frac{\hat{x}}{a} \right)^2 \right] \tag{11.5}$$

and hence

$$F_z = \int_{-b}^{b} \mathrm{d}\hat{y} \int_{-a}^{a} p(\hat{x}, \hat{y}) \mathrm{d}\hat{x} = \frac{2}{3} p_0 2a 2b \tag{11.6}$$

which yields

$$p_0 = \frac{3}{2} \frac{F_z}{(2a)(2b)} \tag{11.7}$$

On an *elliptical* contact patch formulæ (11.2) and (11.3) provide

$$p = p(\hat{x}, \hat{y}) = p_0 \left[1 - \frac{\hat{x}^2}{a^2 \left(1 - \dfrac{\hat{y}^2}{b^2} \right)} \right] \tag{11.8}$$

again with the same peak value p_0 for any $\hat{y}$. The total vertical load is given by

$$F_z = \int_{-b}^{b} \mathrm{d}\hat{y} \int_{-\hat{x}_0(\hat{y})}^{\hat{x}_0(\hat{y})} p(\hat{x}, \hat{y}) \mathrm{d}\hat{x} = \frac{1}{6} \pi p_0 2a 2b \tag{11.9}$$

The aspect ratio a/b of the contact patch is mainly determined by the shape of the tire. However, if F_z and p_0 are kept fixed, the product ab, and hence the total area of the contact patch, is not affected by the aspect ratio, as shown in Fig. 11.6.

11.1.4 Force–Couple Resultant

Exactly like in (2.16), the tangential stresses $\mathbf{t}(\hat{x}, \hat{y}, t)$ exerted by the road on the tire at each point of the contact patch yield a tangential force $\mathbf{F}_t$

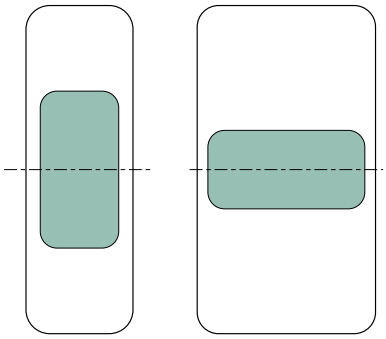

Fig. 11.6 Footprints with different aspect ratio, but equal area

$$\mathbf{F}_t(t) = F_x\,\mathbf{i} + F_y\,\mathbf{j} = \int_{-b}^{b} \mathrm{d}\hat{y} \int_{-\hat{x}_0(\hat{y})}^{\hat{x}_0(\hat{y})} \mathbf{t}(\hat{x}, \hat{y}, t)\mathrm{d}\hat{x} \tag{11.10}$$

and a vertical moment M_z^D with respect to point D

$$M_z^D(t)\,\mathbf{k} = \int_{-b}^{b} \mathrm{d}\hat{y} \int_{-\hat{x}_0(\hat{y})}^{\hat{x}_0(\hat{y})} (\hat{x}\,\mathbf{i} + \hat{y}\,\mathbf{j}) \times \mathbf{t}(\hat{x}, \hat{y}, t)\mathrm{d}\hat{x} \tag{11.11}$$

All inertial effects, of any nature, are neglected.

11.1.5 Elastic Compliance of the Tire Carcass

Under pure rolling steady-state conditions, that is $F_x = F_y = M_z = 0$, let the position of D be the same of the point of virtual contact C, defined in (2.38) and in Fig. 2.16. We recall that, owing to the geometrical effect of camber γ, point C may not coincide with the origin O of the reference system defined in Sect. 2.4.1. However, in a car the camber angle is very small and hence $O \simeq C$.

Under general operating conditions, points D and C may have different positions on the road, mainly due to the *elastic compliance* of the carcass, as can be seen in Fig. 2.10. Therefore, as shown in Fig. 11.7

$$CD = \mathbf{q}(t) = q_x(t)\,\mathbf{i} + q_y(t)\,\mathbf{j} \tag{11.12}$$

To approximately model the lateral and longitudinal compliance of the carcass, it has been assumed that the contact patch (with its reference system $\hat{\mathrm{S}}$) can have small rigid displacements q_x and q_y with respect to the rim, without changing its orientation. A linear relationship between $\mathbf{F}_t$ and $\mathbf{q}$ is the simplest option

$$\mathbf{F}_t = \mathbf{W}\mathbf{q} \tag{11.13}$$

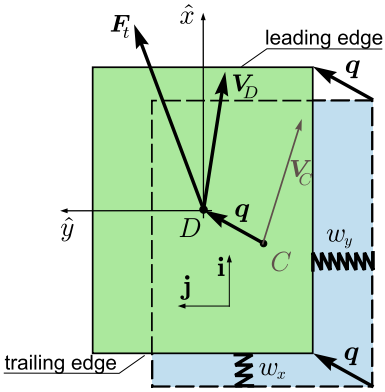

Fig. 11.7 Model of the contact patch for taking into account the carcass compliance

that is, using the vector components

$$F_x = w_x q_x(t) \qquad \text{and} \qquad F_y = w_y q_y(t) \tag{11.14}$$

if

$$\mathbf{W} = \begin{bmatrix} w_x & 0 \\ 0 & w_y \end{bmatrix} \tag{11.15}$$

with constant *carcass stiffnesses* w_x and w_y. Typically, $w_y \ll w_x$. Therefore, $\mathbf{F}_t$ and $\mathbf{q}$ are not parallel vectors.

The displacements q_x and q_y are usually quite small (i.e., $|q_x|, |q_y| \ll a$) and hence they can be neglected with respect to some phenomena, as will be discussed.

More advanced tire models may also include small rigid rotations of the contact patch [9], or employ the stretched string approach to model the carcass flexibility [1, 6, 8].

11.1.6 Friction

Let $V_\mu^P = |\mathbf{V}_\mu^P|$ be the magnitude of the *sliding velocity* $\mathbf{V}_\mu^P$, that is the velocity with respect to the road of a generic bristle tip with root at point $P = (\hat{x}, \hat{y})$,[2] and μ the *local friction coefficient*.[3]

Fairly general rules for *adhesion* and *sliding* between the bristle tip and the road are as follows

[2] For the very first time we look at the kinematics of points in the contact patch.

[3] Not to be confused with the global friction coefficients (2.90) and (2.92).

$$V_\mu^P = 0 \qquad \Longleftrightarrow \qquad |\mathbf{t}| < \mu\, p \qquad \text{(adhesion)} \tag{11.16}$$

$$\mathbf{t} = -\mu\, p\, \frac{\mathbf{V}_\mu^P}{V_\mu^P} \qquad \Longleftrightarrow \qquad V_\mu^P \neq 0 \qquad \text{(sliding)} \tag{11.17}$$

Equation (11.17) simply states that, at sliding, $\mathbf{t}$ and $\mathbf{V}_\mu^P$ have opposite direction and $|\mathbf{t}| = \mu p$. As a matter of fact, the ratio $\mathbf{V}_\mu^P / V_\mu^P$ is just a unit vector directed like the sliding velocity.

If thermal effects are neglected, μ may reasonably depend on the local value of the pressure p and of V_μ^P

$$\mu = \mu(p, V_\mu^P) \tag{11.18}$$

It is common practice to call $\mu_0 = \mu(p, 0)$ the *coefficient of static friction* and $\mu_1 = \mu(p, V_\mu^P \neq 0)$ the *coefficient of kinetic friction*. In the present analysis, to keep it simple, we assume μ_0 and μ_1 to be *constant* all over the contact patch

$$\mu_0 = (1 + \chi)\mu_1, \quad \text{with} \quad \chi > 0 \tag{11.19}$$

thus discarding all dependencies on p and V_μ^P, except the switch from μ_0 to μ_1. Typically, $\mu_0 \approx 1.2\mu_1$, that is $\chi \approx 0.2$. More advanced friction models can be found, e.g., in [2, 3, 9].

11.1.7 Constitutive Relationship

The brush model owes its name to this section. It is indeed the constitutive relation that makes it possible to think of this model as having a moving belt equipped with infinitely many *independent* flexible bristles (Fig. 11.1).

Each massless bristle, while traveling in the contact patch, may have a horizontal deflection $\mathbf{e}(\hat{x}, \hat{y}, t) = e_x\, \mathbf{i} + e_y\, \mathbf{j}$ (Fig. 11.1). The key point is to assume that this deflection $\mathbf{e}(\hat{x}, \hat{y})$ does depend solely on the tangential stress $\mathbf{t}(\hat{x}, \hat{y}, t) = t_x\, \mathbf{i} + t_y\, \mathbf{j}$ at the very same point in the contact patch. In other words, each bristle behaves independently of the others: the constitutive relation is purely *local*. It is quite a strong assumption. Not very realistic, but terribly useful to get a simple model.

Actually, a truly simple model requires three further assumptions. In addition to being *local*, the constitutive relation need to be *linear*, *isotropic* and *homogeneous*, that is simply

$$\mathbf{t}(\hat{x}, \hat{y}, t) = k\, \mathbf{e}(\hat{x}, \hat{y}, t) \tag{11.20}$$

where k is the *bristle stiffness*. In practical terms, it is the local thread stiffness. Usually, k ranges between 30 and 60 $\mathrm{MN/m^3}$.

A linear, but anisotropic and non homogeneous constitutive relation would be like

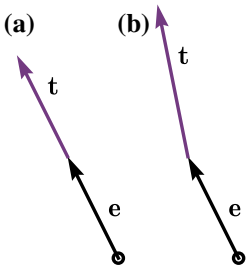

Fig. 11.8 **a** isotropic behavior, **b** anisotropic behavior

$$\begin{bmatrix} t_x \\ t_y \end{bmatrix} = \begin{bmatrix} k_{xx}(\hat{x}, \hat{y}) & k_{xy}(\hat{x}, \hat{y}) \\ k_{yx}(\hat{x}, \hat{y}) & k_{yy}(\hat{x}, \hat{y}) \end{bmatrix} \begin{bmatrix} e_x \\ e_y \end{bmatrix} \quad \text{that is} \quad \mathbf{t} = K\mathbf{e} \tag{11.21}$$

with $k_{xy} = k_{yx}$ and often equal to zero. It is anisotropic if $k_{xx} \neq k_{yy}$. It is non homogeneous, if k's depend on their position $(\hat{x}, \hat{y})$ in the contact patch.

As shown in Fig. 11.8 and according to (11.20), isotropy implies that $\mathbf{t}$ and $\mathbf{e}$ always have the same direction.

It is worth noting that in (11.20) (and also in (11.21)) all quantities, including $\mathbf{t}$ and $\mathbf{e}$, are associated with the coordinates of the root, not of the tip of the bristle. Much like in the classical theory of linear elasticity, we are assuming that the problem can be safely formulated with reference to the undeformed state. This is reasonable provided the bristle deflections $\mathbf{e}$ are small, that is $|\mathbf{e}| \ll a$, which is usually the case.

11.1.8 Kinematics

We can define two fundamental *global* motions in the kinematics of a tire in contact with the ground:

1. the continuous flow of undeformed rubber tread in the contact patch (due to the wheel rolling);
2. the motion of the contact patch with respect to the road.

The superposition of these two motions leads to what we call here the *skating velocity field* of the roots of the bristles.

For an in-depth discussion of some related topics, like the definitions of the translational slip $\boldsymbol{\sigma}$ and of the spin slip φ, we refer to Sect. 2.9.

11.1.8.1 Belt Flow

As shown in Figs. 11.1 and 11.2, the first motion is modelled by assuming that the belt (i.e., the root of each bristle) moves with respect to the rim with a velocity equal to minus the rolling velocity $\mathbf{V}_r$

$$\mathbf{V}_r = V_r\,\mathbf{i} = \omega_c r_r\,\mathbf{i} \tag{11.22}$$

as defined in (2.53). This flow is always along parallel lines directed like $-\mathbf{i}$ in the reference system $\hat{\mathsf{S}}$.

It is worth noting that in the brush model the rolling velocity may change in time ($V_r = V_r(t)$), but it must be the same at all points of the contact patch (it is a *global* parameter).

This property makes it possible to define a sort of global *rolling distance* $s(t)$

$$s(t) = \int_0^t V_r(t)\mathrm{d}t \qquad \text{that is} \qquad \frac{\mathrm{d}s}{\mathrm{d}t} = V_r(t) \tag{11.23}$$

If $V_r > 0$, the function $s(t)$ is one-to-one. It will be shown that, in some cases, the use of s as the independent variable is more convenient than the use of time t.

As already stated, the forefront border of the contact patch is called the leading edge. It is very important to realize that it is through the leading edge that *undeformed* rubber tread enters the contact patch (Fig. 11.1).

11.1.8.2 Motion of the Contact Patch

As shown in Fig. 11.7, the second fundamental motion is modelled by considering the contact patch $\mathscr{P}$ as a rigid region that moves with respect to the road.

The velocity $\mathbf{V}_C = \mathbf{V}_c$, of the point of virtual contact C (see p. 27) is, by definition, the *travel velocity* $\mathbf{V}_c$, defined in (2.58) for a real wheel. From (2.60) and (2.69) it follows that

$$\mathbf{V}_C = \mathbf{V}_r + \mathbf{V}_s = \mathbf{V}_r + V_r\boldsymbol{\sigma} \tag{11.24}$$

where $\mathbf{V}_s = V_r\boldsymbol{\sigma}$ is the *slip velocity*, and $\boldsymbol{\sigma}$ is the theoretical slip vector.

Differentiating (11.12), we obtain the velocity $\mathbf{V}_D$ of the center D of the contact patch (Figs. 11.7)

$$\mathbf{V}_D = \mathbf{V}_C + \dot{\mathbf{q}} = \mathbf{V}_c + \dot{q}_x\,\mathbf{i} + \dot{q}_y\,\mathbf{j} \tag{11.25}$$

The generic point $\hat{P} = (\hat{x}, \hat{y})$ of the contact patch $\mathscr{P}$ (not of the tire) has a velocity $\mathbf{V}_{\hat{P}}$ equal to

$$\mathbf{V}_{\hat{P}} = \mathbf{V}_D + \omega_{s_z}\,\mathbf{k} \times D\hat{P} = \mathbf{V}_c + \dot{\mathbf{q}} + \omega_{s_z}\,\mathbf{k} \times (\hat{x}\,\mathbf{i} + \hat{y}\,\mathbf{j}) \tag{11.26}$$

where ω_{s_z} is the slip yaw rate, as defined in (2.64). In the brush model there is slip yaw rate ω_{s_z} only within the contact patch, as if it were entirely due to the camber angle γ. Of course, if $\omega_{s_z} = 0$, we have $\mathbf{V}_{\hat{P}} = \mathbf{V}_D$.

11.1.8.3 Skating Velocity Field of the Bristle Roots

The combination of these two global motions yields the *local kinematics*, that is the motion of each *bristle root*.

The *root* of the bristle (momentarily) at point $\hat{P} = (\hat{x}, \hat{y}) = (\hat{x}_b(t), \hat{y})$ of the contact patch has a velocity $\mathbf{V}_s^P$ with respect to the ground given by the superimposition of the two global motions

$$\begin{aligned}
\mathbf{V}_s^P(\hat{x}, \hat{y}, t) &= \mathbf{V}_{\hat{P}}(\hat{x}, \hat{y}, t) - \mathbf{V}_r(t) \\
&= \left(\mathbf{V}_c + \omega_{s_z}\,\mathbf{k} \times (\hat{x}\,\mathbf{i} + \hat{y}\,\mathbf{j}) + \dot{\mathbf{q}}\right) - \mathbf{V}_r \\
&= (\mathbf{V}_c - \mathbf{V}_r) + \omega_{s_z}\,\mathbf{k} \times (\hat{x}\,\mathbf{i} + \hat{y}\,\mathbf{j}) + \dot{\mathbf{q}} \\
&= \mathbf{V}_s + (\hat{x}\,\mathbf{j} - \hat{y}\,\mathbf{i})\omega_{s_z} + \dot{\mathbf{q}} \\
&= V_r[\boldsymbol{\sigma} - (\hat{x}\,\mathbf{j} - \hat{y}\,\mathbf{i})\varphi] + \dot{\mathbf{q}}
\end{aligned} \tag{11.27}$$

where $\mathbf{V}_s = V_r\boldsymbol{\sigma}$, and $\omega_{s_z} = -V_r\varphi$ as in (2.68), where φ is the spin slip.

The velocity $\mathbf{V}_s^P$ of each bristle *root* is called here the *skating velocity*.[4] It is the velocity of the root of a bristle with respect to the road, not to be confused with the sliding velocity $\mathbf{V}_\mu^P$ of the bristle tip. Perhaps, a look at Fig. 11.17 can be useful to clarify the matter.

11.1.9 Brush Model Slips

The skating velocity field (11.27) of the brush model depends on the translational slip $\boldsymbol{\sigma}$ and on the spin slip φ, defined in Sect. 2.9 for the rim of any real wheel with tire. This is no coincidence, as the kinematics of the brush model has been built around these slips.

However, the brush model behavior is better described if some other non-dimensional vectorial quantities are defined.

11.1.9.1 Skating Slips

Equation (11.27) suggests to define the *skating slips* $\boldsymbol{\varepsilon}(\hat{x}, \hat{y}, t)$

$$\begin{aligned}
\boldsymbol{\varepsilon} &= \frac{\mathbf{V}_s^P}{V_r} \\
&= \boldsymbol{\sigma} - (\hat{x}\,\mathbf{j} - \hat{y}\,\mathbf{i})\varphi + \frac{\dot{\mathbf{q}}}{V_r}
\end{aligned} \tag{11.28}$$

Equation (11.27) can now be rewritten as

[4] The use of the practical slip $\boldsymbol{\kappa}$ would not have provided an equally neat formula.

$$\mathbf{V}_s^P = V_r \boldsymbol{\varepsilon} \tag{11.29}$$

Quite a compact formula.

A peculiar feature of the skating slips is that, whenever the spin slip $\varphi \neq 0$, they are *local*, in the sense that each point in the contact patch has its own $\boldsymbol{\varepsilon} = \boldsymbol{\varepsilon}(\hat{x}, \hat{y}, t)$. The bristle roots behave according to $\boldsymbol{\varepsilon}$.

11.1.9.2 Steady-State Skating Slips

Since it is very common to analyze the brush model assuming steady-state conditions ($\dot{\mathbf{q}} = \mathbf{0}$), it is convenient to define the *steady-state skating slips* $\boldsymbol{\lambda}(\hat{x}, \hat{y})$

$$\boldsymbol{\lambda} = \boldsymbol{\sigma} - (\hat{x}\,\mathbf{j} - \hat{y}\,\mathbf{i})\varphi \tag{11.30}$$

11.1.9.3 Transient Translational Slip

Also convenient is to define the *transient translational slip* $\boldsymbol{\rho}(t)$

$$\boldsymbol{\rho}(t) = \boldsymbol{\sigma}(t) + \frac{\dot{\mathbf{q}}(t)}{V_r(t)} \tag{11.31}$$

We see that $\boldsymbol{\rho}$ is a *global* quantity, like $\boldsymbol{\sigma}$. However, unlike $\boldsymbol{\sigma}$, it is not defined in a real wheel with tire, because it involves the velocity of the carcass deformation $\dot{\mathbf{q}}$.

We will see shortly that in the transient brush model the bristle roots behave according to $\boldsymbol{\rho}$, whereas the rim, by definition, behaves according to $\boldsymbol{\sigma}$. This is the key to understand the physical meaning of $\boldsymbol{\rho}$.

Of course, both $\boldsymbol{\lambda}(\hat{x}, \hat{y})$ and $\boldsymbol{\rho}(t)$ are special cases of $\boldsymbol{\varepsilon}(\hat{x}, \hat{y}, t)$.

11.1.10 Sliding Velocity of the Bristle Tips

To study the possible *sliding* of each bristle *tip* on the ground, let us consider the bristle root with coordinates $(\hat{x}, \hat{y}) = (\hat{x}_b(t), \hat{y})$.

According to (11.27), its root moves with respect to the road with a skating velocity $\mathbf{V}_s^P(\hat{x}, \hat{y}, t)$ (Figs. 11.1 and 11.2).

At the same time, the bristle has a deflection $\mathbf{e}(\hat{x}, \hat{y}, t)$, and hence, by definition, its tip has a velocity with respect to the root[5]

$$\dot{\mathbf{e}} = \frac{\mathrm{d}\mathbf{e}}{\mathrm{d}t} = \dot{\mathbf{e}}(\hat{x}, \hat{y}, t) \tag{11.32}$$

[5]The total time derivative is evaluated within $\hat{\mathsf{S}}$, that is as if $\mathbf{i}$ and $\mathbf{j}$ were fixed.

Therefore, the (possible) *sliding velocity* $\mathbf{V}_\mu^P$ of a bristle tip with respect to the road is given by the sum of these *two* vectorial contributions

$$\mathbf{V}_\mu^P(\hat{x}, \hat{y}, t) = \mathbf{V}_s^P + \dot{\mathbf{e}} \tag{11.33}$$

However, exactly like in fluid dynamics, it is more convenient to take a so-called Eulerian approach,[6] which provides

$$\dot{\mathbf{e}} = \frac{\mathrm{d}\mathbf{e}(\hat{x}_b(t), \hat{y}, t)}{\mathrm{d}t} = \frac{\partial \mathbf{e}}{\partial \hat{x}} \frac{\mathrm{d}\hat{x}_b}{\mathrm{d}t} + \frac{\partial \mathbf{e}}{\partial t} = -\mathbf{e}_{,\hat{x}} V_r + \mathbf{e}_{,t} \tag{11.34}$$

since $\mathrm{d}\hat{y}/\mathrm{d}t = 0$ and where, for brevity, $\mathbf{e}_{,\hat{x}} = \partial \mathbf{e}/\partial \hat{x}$ and $\mathbf{e}_{,t} = \partial \mathbf{e}/\partial t$. The rationale of this last formula is that, again like in fluid dynamics, it is easier to keep fixed the observation point, rather than follow each bristle.

Combining (11.33) and (11.34), the *sliding velocity* $\mathbf{V}_\mu^P$ of a bristle tip with respect to the road is

$$\begin{aligned} \mathbf{V}_\mu^P(\hat{x}, \hat{y}, t) &= \mathbf{V}_s^P + \dot{\mathbf{e}} \\ &= V_r \boldsymbol{\varepsilon} - V_r \mathbf{e}_{,\hat{x}} + \mathbf{e}_{,t} \\ &= V_r(\boldsymbol{\varepsilon} - \mathbf{e}_{,\hat{x}}) + \mathbf{e}_{,t} \end{aligned} \tag{11.35}$$

Of course, there is *adhesion* (i.e., no sliding) between the tip and the road if and only if $\mathbf{V}_\mu^P = \mathbf{0}$, like in (11.16) (see also Fig. 11.2a and b).

11.1.11 Summary of Relevant Velocities

A number of velocities, either global or local, have been defined or recalled in this Section. It is perhaps useful to list all of them:

1. rolling velocity: $\mathbf{V}_r$, global;
2. sliding velocity: $\mathbf{V}_\mu^P$, local;
3. travel velocity: $\mathbf{V}_C = \mathbf{V}_c$, global;
4. carcass deformation velocity: $\dot{\mathbf{q}}$, global;
5. velocity of the center D: $\mathbf{V}_D$, global;
6. slip velocity: $\mathbf{V}_s$, global;
7. velocity of a generic point of the footprint: $\mathbf{V}_{\hat{P}}$, local;
8. skating velocity: $\mathbf{V}_s^P$, local;
9. bristle deflection velocity: $\dot{\mathbf{e}}$, local.

[6] As reported in [11, p. 4], this approach is actually due to d'Alembert.

11.2 General Governing Equations of the Brush Model

The brush model has been completely defined in the previous section. A schematic was shown in Fig. 11.1. Its distinguishing feature is that each bristle behaves independently of the others.

The fundamental governing equations for the *transient* behavior are to be obtained by combining all the relationships given in the brush model definition. Of course, the goal is

$$\text{rim kinematics} \quad \Longleftrightarrow \quad \text{force and moment} \tag{11.36}$$

like in (2.88).

Therefore, we assume as given the following parameters:

- the shape of the contact patch (rectangular, elliptical, etc.);
- the size of the contact patch: a and b;
- the pressure distribution $p(\hat{x}, \hat{y})$;
- the grip coefficients $\mu_0 = (1 + \chi)\mu_1$;
- the bristle stiffness k;
- the carcass stiffnesses w_x and w_y;

and the following kinematic input functions:

- the rolling speed $V_r(t)$;
- the translational slip $\boldsymbol{\sigma}(t)$;
- the spin slip $\varphi(t)$.

We consider as unknown the functions $\mathbf{e}(\hat{x}, \hat{y}, t)$ and $\mathbf{q}(t)$, that is the field of bristle deflections and the longitudinal and lateral deflections of the carcass. Of course, the differential equations have to be supplied with suitable *initial conditions* on the whole contact patch and *boundary conditions* at the leading edge.

That said, let us dig into equations (relax, they look awful at first, but after a while their interplay will start to fascinate you, maybe…).

According to (11.16) and (11.35), and as exemplified in Fig. 11.2b, wherever there is *adhesion* between the tip and the road, the deflection $\mathbf{e}$ must change with the following time rate

$$\dot{\mathbf{e}} + \mathbf{V}_s^P = \mathbf{0} \qquad \Longleftrightarrow \qquad |k\mathbf{e}| < \mu_0\, p \qquad \text{(adhesion)} \tag{11.37}$$

This is a complicated way to say simply that the tip does not move with respect to the road, while its root does.

The bristle tip starts *sliding* as soon as the friction limit is reached ($|\mathbf{t} = k\mathbf{e}| = \mu_0 p$). In some sense, adhesion has a higher priority than sliding.

Switching from adhesion to sliding means that the governing equation changes abruptly into (11.17), which, owing to (11.20) and (11.35), is equivalent to

$$k\mathbf{e} = -\mu_1 p \frac{\dot{\mathbf{e}} + \mathbf{V}_s^P}{|\dot{\mathbf{e}} + \mathbf{V}_s^P|} \qquad \Longleftrightarrow \qquad |\dot{\mathbf{e}} + \mathbf{V}_s^P| > 0 \qquad \text{(sliding)} \tag{11.38}$$

This vectorial differential equation states that, whenever there is sliding, we have $k|\mathbf{e}| = \mu_1 p$, and the vectors $\mathbf{t} = k\mathbf{e}$ and $\mathbf{V}_\mu^P = \dot{\mathbf{e}} + \mathbf{V}_s^P$ have the same, unknown, direction. Let us expand these observations. Sliding means that the deflection $\mathbf{e}$ is a vector whose intensity is equal to $\mu_1 p/k$, and is directed like the local sliding velocity $\mathbf{V}_\mu^P$. To fulfill simultaneously these two requirements there must be a nice interplay between $\mathbf{V}_s^P$ and $\dot{\mathbf{e}}$.

According to (11.34) and (11.35), Eqs. (11.37) and (11.38) can be recast as follows, where $\varepsilon = \boldsymbol{\rho} - (\hat{x}\,\mathbf{j} - \hat{y}\,\mathbf{i})\varphi$

$$\mathbf{e}_{,\hat{x}} - \mathbf{e}_{,t}/V_r - \varepsilon = \mathbf{0} \qquad \Longleftrightarrow \qquad k|\mathbf{e}| < \mu_0\, p \qquad \text{(adhesion)} \tag{11.39}$$

$$k\mathbf{e} = \mu_1 p \frac{\mathbf{e}_{,\hat{x}} - \mathbf{e}_{,t}/V_r - \varepsilon}{|\mathbf{e}_{,\hat{x}} - \mathbf{e}_{,t}/V_r - \varepsilon|} \qquad \Longleftrightarrow \qquad |\mathbf{e}_{,\hat{x}} - \mathbf{e}_{,t}/V_r - \varepsilon| > 0 \qquad \text{(sliding)} \tag{11.40}$$

with given boundary conditions at the leading edge $\hat{x} = \hat{x}_0(\hat{y})$

$$\mathbf{e}(\hat{x}_0(\hat{y}), \hat{y}, t) = 0 \tag{11.41}$$

and initial conditions

$$\mathbf{e}(\hat{x}, \hat{y}, 0) = \mathbf{e}_0(\hat{x}, \hat{y}) \tag{11.42}$$

This is a two-state system, in the sense that only one partial differential equation applies at each point of the contact patch: we can either have adhesion or sliding, but not both (or none). By definition, adhesion means $|\mathbf{V}_\mu^P| = 0$ and the differential equation (11.40) of sliding is indeed meaningless.

A closer look shows that we have a different two-state system for any value of $\hat{y}$. Indeed, the spatial derivatives in (11.39) and (11.40) are only with respect to $\hat{x}$, that is in the direction $\mathbf{i}$ of the rolling velocity $V_r\,\mathbf{i}$. The rubber flows along parallel lines that do not interact to each other (in this model!).

However, the problem formulation needs an additional vectorial equation since $\dot{\mathbf{q}}$ is unknown, and so is $\boldsymbol{\rho}(t) = \boldsymbol{\sigma} + \dot{\mathbf{q}}/V_r$. Differentiating (11.13) with respect to time and taking (11.31) into account provides

$$\dot{\mathbf{F}}_t = \mathbf{W}\dot{\mathbf{q}} = \mathbf{W}\,(\boldsymbol{\rho} - \boldsymbol{\sigma})V_r \tag{11.43}$$

Also useful is to insert the constitutive relationship (11.20) into (11.10) and then differentiate with respect to time

$$\dot{\mathbf{F}}_t = \frac{\mathrm{d}}{\mathrm{d}t}\left(k\int_{-b}^{b}\mathrm{d}\hat{y}\int_{-\hat{x}_0(\hat{y})}^{\hat{x}_0(\hat{y})}\mathbf{e}\,\mathrm{d}\hat{x}\right) = k\int_{-b}^{b}\mathrm{d}\hat{y}\int_{-\hat{x}_0(\hat{y})}^{\hat{x}_0(\hat{y})}\mathbf{e}_{,t}\,\mathrm{d}\hat{x} \tag{11.44}$$

Combining (11.43) and (11.44) yields the missing additional governing equation

$$k\int_{-b}^{b}\mathrm{d}\hat{y}\int_{-\hat{x}_0(\hat{y})}^{\hat{x}_0(\hat{y})}\mathbf{e}_{,t}\,\mathrm{d}\hat{x} = \mathbf{W}\dot{\mathbf{q}} = \mathbf{W}\,(\boldsymbol{\rho}-\boldsymbol{\sigma})V_r \tag{11.45}$$

Summing up, the behavior of the *transient* brush model, that is the functions $\mathbf{e}(\hat{x},\hat{y},t)$ and $\boldsymbol{\rho}(t)$, for given boundary conditions $\mathbf{e}(\hat{x}_0(\hat{y}),\hat{y},t)=\mathbf{0}$ at the leading edge and initial conditions $\mathbf{e}(\hat{x},\hat{y},0)=\mathbf{e}_0(\hat{x},\hat{y})$ and $\boldsymbol{\rho}(0)=\boldsymbol{\rho}_0$, is completely defined by the *governing equations* (11.39) or (11.40), and (11.45).

Actually, a somehow more compact formulation of the very same problem can be obtained employing, instead of time t, the rolling distance s, defined in (11.23). Since there is a one-to-one correspondence between t and s, that is $t=t(s)$, and all time derivatives in the brush model are divided by $V_r(t)=\mathrm{d}s/\mathrm{d}t$, the general governing equations can be reformulated in terms of $\mathbf{e}(\hat{x},\hat{y},s)$ in the following way, with $\boldsymbol{\varepsilon}=\boldsymbol{\rho}-(\hat{x}\,\mathbf{j}-\hat{y}\,\mathbf{i})\varphi$

$$\mathbf{e}_{,\hat{x}}-\mathbf{e}_{,s}-\boldsymbol{\varepsilon}=\mathbf{0} \quad\Longleftrightarrow\quad k|\mathbf{e}|<\mu_0\,p \qquad \text{(adhesion)} \tag{11.46}$$

$$k\mathbf{e}=\mu_1 p\,\frac{\mathbf{e}_{,\hat{x}}-\mathbf{e}_{,s}-\boldsymbol{\varepsilon}}{|\mathbf{e}_{,\hat{x}}-\mathbf{e}_{,s}-\boldsymbol{\varepsilon}|} \quad\Longleftrightarrow\quad |\mathbf{e}_{,\hat{x}}-\mathbf{e}_{,s}-\boldsymbol{\varepsilon}|>0 \qquad \text{(sliding)} \tag{11.47}$$

along with

$$k\int_{-b}^{b}\mathrm{d}\hat{y}\int_{-\hat{x}_0(\hat{y})}^{\hat{x}_0(\hat{y})}\mathbf{e}_{,s}\,\mathrm{d}\hat{x} = \mathbf{W}\frac{\mathrm{d}\mathbf{q}}{\mathrm{d}s} = \mathbf{W}\,(\boldsymbol{\rho}-\boldsymbol{\sigma}) \tag{11.48}$$

where $\mathbf{e}_{,s}=\partial\mathbf{e}/\partial s$. This formulation shows that the rolling velocity $V_r(t)$ does not have any influence on the behavior of the brush model with respect to the rolling distance s. The main reason is that all inertial effects have been neglected, as in (2.26).

Either in terms of t or s, this is quite a difficult mathematical problem if tackled in its full generality. Indeed, the *transient* behavior of a real wheel with tire (cf. (2.20)) is a rather difficult matter.

Fortunately, the brush model becomes much simpler under steady-state conditions, as discussed in Sect. 11.3. However, to deal with the simplest (and most classical) brush model you have to wait till Sect. 11.5, where the spin slip is set equal to zero and there is only translational slip. With a rectangular contact patch, as in Sect. 11.5.1, the whole model can be worked out analytically. Notwithstanding the very many simplifying assumptions, it is still an interesting and significant model.

11.2.1 Data for Numerical Examples

Almost all figures from here onwards in this chapter have been obtained with the following numerical values:

$$\begin{array}{lll} a = 7.5\,\text{cm} & b = 5.6\,\text{cm} & r_r = 25\,\text{cm} \\ \mu_0 = 1 & \chi = 0.2 & p_0 = 0.3\,\text{Mpa} \\ k = 30\,\text{MN/m}^3 & w_x = 500\,\text{kN/m} & w_y = 125\,\text{kN/m} \end{array} \tag{11.49}$$

11.3 Brush Model Steady-State Behavior

The main, and most common, simplification is assuming the brush model to be in steady-state conditions (Fig. 11.1). Therefore, by definition, the field of bristle deflections $\mathbf{e}$ and the carcass deformation $\mathbf{q}$ are both time independent.

These conditions can be formulated as

- $\mathbf{e}_{,t} = \mathbf{0}$, and hence $\mathbf{e} = \mathbf{e}(\hat{x}, \hat{y})$, with no time dependence;
- $\dot{\mathbf{q}} = \mathbf{0}$, which means that $\boldsymbol{\rho} = \boldsymbol{\sigma}$ is an input quantity for the tire model and it is constant in time.

The problem is substantially simpler, since the only unknown function is the field of bristle deflections $\mathbf{e}(\hat{x}, \hat{y})$, and both the adhesion and sliding zones are governed by first-order *ordinary* differential equations, with respect to the variable $\hat{x}$.

More in detail, the skating slip $\boldsymbol{\varepsilon}$, defined in (11.28), becomes the steady-state skating slip $\boldsymbol{\lambda}$, defined in (11.30)

$$\boldsymbol{\lambda}(\hat{x}, \hat{y}) = \frac{\mathbf{V}_s^P(\hat{x}, \hat{y}, t)}{V_r(t)} = \boldsymbol{\sigma} - (\hat{x}\,\mathbf{j} - \hat{y}\,\mathbf{i})\varphi \tag{11.50}$$

with *constant* translational slip σ and *constant* spin slip φ. Therefore, the skating slip $\boldsymbol{\varepsilon} = \boldsymbol{\lambda}$ is a given, purely kinematic quantity, a known input to the model. It is worth noting that some quantities may be still time dependent, like $\mathbf{V}_s^P$ and V_r.

According to (11.34), the total time derivative of the deflection of each bristle tip is given by

$$\frac{\dot{\mathbf{e}}}{V_r(t)} = -\frac{\mathrm{d}\mathbf{e}}{\mathrm{d}\hat{x}} = -\mathbf{e}'(\hat{x}, \hat{y}) \tag{11.51}$$

where $\mathbf{e}'$ was introduced to stress that it is a total derivative (with respect to $\hat{x}$).[7] Whenever $\mathbf{e}' \neq \mathbf{0}$, the bristle deflection changes as the bristle root changes its position with respect to the footprint (Fig. 11.2).

The sliding velocity (11.35) of each bristle tip becomes

$$\mathbf{V}_\mu^P(\hat{x}, \hat{y}, t) = V_r(\boldsymbol{\lambda} - \mathbf{e}') \tag{11.52}$$

[7] In the brush model, $\hat{y}$ is more a parameter than a variable.

11.3.1 Steady-State Governing Equations

According to (11.50) and (11.51), in the steady-state case the governing equations (11.39) and (11.40) of the brush model become (cf. [1, p. 761] and [8, p. 83])

$$\mathbf{e}' - \boldsymbol{\lambda} = \mathbf{0} \qquad \Longleftrightarrow \qquad k|\mathbf{e}| < \mu_0\, p \qquad \text{(adhesion)} \tag{11.53}$$

$$k\mathbf{e} = \mu_1 p \frac{\mathbf{e}' - \boldsymbol{\lambda}}{|\mathbf{e}' - \boldsymbol{\lambda}|} \qquad \Longleftrightarrow \qquad |\mathbf{e}' - \boldsymbol{\lambda}| > 0 \qquad \text{(sliding)} \tag{11.54}$$

where $\mathbf{e}' = \mathbf{e}_{,\hat{x}}$.

These first-order differential equations in the unknown function $\mathbf{e}(\hat{x}, \hat{y})$, along with the boundary conditions at the leading edge, completely describe the behavior of the brush model.[8] Indeed, in this case the other Eq. (11.45) simply states $\boldsymbol{\rho} = \boldsymbol{\sigma}$.

As already remarked, this is a two-state system, since at each point there is, obviously, either adhesion or sliding. To distinguish between the solutions in the *adhesion* and in the *sliding* regions, we will use the symbols $\mathbf{e}_a$ and $\mathbf{e}_s$, respectively.

11.3.2 Adhesion and Sliding Zones

Each bristle, which behaves independently of the others, is *undeformed* when it enters the contact patch through the leading edge $\hat{x}_0(\hat{y})$. Its tip sticks to the ground (Fig. 11.2a) and, due to the skating velocity $\mathbf{V}_s^P$ between the bristle root and the road, a deflection $\mathbf{e}$ immediately starts to build up (Fig. 11.2b), along with a tangential stress $\mathbf{t} = k\mathbf{e}$. The physical interpretation of the adhesion equation $\mathbf{e}' = \boldsymbol{\lambda}$ is that the growth of the bristle deflection is completely and solely ruled by the wheel kinematics. It is not affected directly by the bristle stiffness k, neither by the pressure distribution.

On the other hand, the physical interpretation of the sliding equation is that the tangential stress $\mathbf{t}$ is always directed like the sliding velocity

To better understand the roles played by adhesion and sliding, we refer to Fig. 11.9, where a fairly unusual pressure pattern has been depicted.

11.3.2.1 Adhesion

At first there is adhesion, and Eq. (11.53) applies with initial condition $\mathbf{e}_a = \mathbf{0}$ at $\hat{x}_0$ (point A in Fig. 11.9). A simple integration provides the behavior of the bristle deflection $\mathbf{e}_a$ in the adhesion zone

[8] More convenient governing equations for the sliding state are given in (11.59) and (11.60).

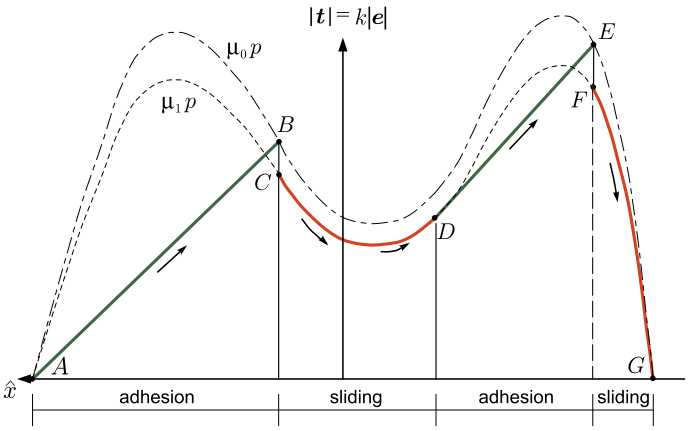

Fig. 11.9 Adhesion and sliding zones in the case $\boldsymbol{\lambda} = \boldsymbol{\sigma} = \text{const.}$ (very unusual pressure distribution!)

$$\begin{aligned}\mathbf{e}_a(\hat{x}, \hat{y}) &= \int_{\hat{x}_0}^{\hat{x}} \mathbf{e}' \mathrm{d}\hat{x} = \int_{\hat{x}_0}^{\hat{x}} \boldsymbol{\lambda} \mathrm{d}\hat{x} = \int_{\hat{x}_0}^{\hat{x}} \left[\boldsymbol{\sigma} - \varphi(\hat{x}\,\mathbf{j} - \hat{y}\,\mathbf{i})\right] \mathrm{d}\hat{x} \\ &= -\boldsymbol{\sigma}\,(\hat{x}_0 - \hat{x}) + \varphi\left[\frac{(\hat{x}_0 - \hat{x})(\hat{x}_0 + \hat{x})}{2}\,\mathbf{j} - \hat{y}(\hat{x}_0 - \hat{x})\,\mathbf{i}\right]\end{aligned} \tag{11.55}$$

It is worth noting that this expression is linear with respect to $\boldsymbol{\sigma}$ and φ. Moreover, it is not affected directly by the pressure distribution.

The magnitude of $\mathbf{e}_a$ is given by

$$|\mathbf{e}_a| = \sqrt{\mathbf{e}_a \cdot \mathbf{e}_a} = (\hat{x}_0 - \hat{x})\sqrt{(\sigma_x + \varphi\hat{y})^2 + \left(\sigma_y - \varphi\frac{\hat{x}_0 + \hat{x}}{2}\right)^2} \tag{11.56}$$

Expressions (11.55) and (11.56) simplify considerably if $\varphi = 0$, that is $\boldsymbol{\lambda} = \boldsymbol{\sigma} = \text{const.}$

Line A–B in Fig. 11.9 shows an example of linear growth ($\boldsymbol{\lambda} = \boldsymbol{\sigma}$). According to (11.53), the adhesion state is maintained as far as $k|\mathbf{e}_a| < \mu_0 p$, that is up to $\hat{x}_s = \hat{x}_s(\boldsymbol{\sigma}, \varphi, \hat{y})$ (point B in Fig. 11.9) where

$$|\mathbf{t}| = k|\mathbf{e}_a(\hat{x}_s, \hat{y})| = \mu_0 p(\hat{x}_s, \hat{y}) \tag{11.57}$$

In the proposed model, as soon as the static friction limit is reached at point $\hat{x} = \hat{x}_s$, the following sudden change in the deflection (massless bristle) occurs

$$\mathbf{e}_s(\hat{x}_s, \hat{y}) = \frac{\mu_1}{\mu_0}\mathbf{e}_a(\hat{x}_s, \hat{y}) \tag{11.58}$$

Therefore, at the transition from adhesion to sliding the deflection preserves its direction, but with a sudden reduction in magnitude (line *B*–*C* in Fig. 11.9).

11.3.2.2 Sliding

The sliding state starts with $\mathbf{e}_s(\hat{x}_s, \hat{y})$ as initial condition and evolves according to (11.54), that is to a system of two nonlinear first-order ordinary differential equations. However, (11.54) can be recast in a simpler, more convenient form

$$\begin{aligned} \mathbf{e}_s \cdot \mathbf{e}_s &= \left(\frac{\mu_1 p}{k}\right)^2 \\ (\mathbf{e}_s \times (\boldsymbol{\lambda} - \mathbf{e}_s')) \cdot \mathbf{k} &= 0 \end{aligned} \tag{11.59}$$

that is, using components

$$\begin{aligned} e_x^2 + e_y^2 &= \left(\frac{\mu_1 p}{k}\right)^2 \\ e_x(\lambda_y - e_y') &= e_y(\lambda_x - e_x') \end{aligned} \tag{11.60}$$

which is a *differential–algebraic* system. Indeed, the sliding state requires:

- the magnitude of the tangential stress $\mathbf{t}$ to be equal to the kinetic coefficient of friction times the pressure (curved line *C*–*D* in Fig. 11.9)
- the direction of $\mathbf{t}$ (and hence of $\mathbf{e}_s$) to be the same as that of the sliding velocity $\mathbf{V}_\mu^P = V_r(\boldsymbol{\lambda} - \mathbf{e}_s')$.

These are precisely the two conditions stated by (11.59) or (11.60).

Although, in general, the exact solution cannot be obtained by analytical methods, some features of the solution are readily available.

Let $\mathbf{s}$ be a unit vector directed like the sliding velocity $\mathbf{V}_\mu^P$, that is such that

$$\mathbf{V}_\mu^P = |\mathbf{V}_\mu^P|\mathbf{s} \tag{11.61}$$

or, equivalently, $\mathbf{t} = -|\mathbf{t}|\mathbf{s}$ and $\mathbf{e} = -|\mathbf{e}|\mathbf{s}$.

As well known, for any unit vector we have $\mathbf{s} \cdot \mathbf{s}' = 0$, where $\mathbf{s}' = \partial\mathbf{s}/\partial\hat{x}$. Therefore, $\mathbf{m} = \mathbf{s}'/|\mathbf{s}'|$ is a unit vector orthogonal to $\mathbf{s}$ (and hence to $\mathbf{V}_\mu^P$), and the skating slip $\boldsymbol{\lambda}$ can be expressed as

$$\boldsymbol{\lambda} = (\boldsymbol{\lambda} \cdot \mathbf{s})\mathbf{s} + (\boldsymbol{\lambda} \cdot \mathbf{m})\mathbf{m} \tag{11.62}$$

Moreover, according to (11.54)

$$\mathbf{e}_s = -\frac{\mu_1 p}{k}\mathbf{s} \qquad \Longrightarrow \qquad \mathbf{e}_s' = -\frac{\mu_1 p'}{k}\mathbf{s} - \frac{\mu_1 p}{k}\mathbf{s}' \tag{11.63}$$

Combining (11.61)–(11.63) we get

$$\begin{aligned} \frac{\mathbf{V}_\mu^P}{V_r} &= \frac{|\mathbf{V}_\mu^P|}{V_r}\mathbf{s} = \boldsymbol{\lambda} - \mathbf{e}_s' \\ &= (\boldsymbol{\lambda}\cdot\mathbf{s})\mathbf{s} + (\boldsymbol{\lambda}\cdot\mathbf{m})\mathbf{m} + \frac{\mu_1 p'}{k}\mathbf{s} + \frac{\mu_1 p}{k}|\mathbf{s}'|\mathbf{m} \\ &= \left(\boldsymbol{\lambda}\cdot\mathbf{s} + \frac{\mu_1 p'}{k}\right)\mathbf{s} \end{aligned} \tag{11.64}$$

which shows which terms actually contribute to the sliding velocity $\mathbf{V}_\mu^P$.

In most cases, the sliding regime is preserved up to the trailing edge, that is till the end of the contact patch. However, it is interesting to find the conditions that can lead the bristle to switch back to adhesion (like point D in Fig. 11.9). From (11.64) it immediately arises that

$$|\mathbf{V}_\mu^P| = 0 \qquad \Longleftrightarrow \qquad k\boldsymbol{\lambda}\cdot\mathbf{s} + \mu_1 p' = 0 \tag{11.65}$$

Since $\mathbf{s}$ depends on the solution $\mathbf{e}_s$ of the algebraic-differential system of equations (11.60), this condition has to be checked at each numerical integration step.

The governing equation (11.54) of the sliding state deserves some further discussion. The "annoying" term $(\boldsymbol{\lambda} - \mathbf{e}_s')/|\boldsymbol{\lambda} - \mathbf{e}_s'|$ is simply equal to $\boldsymbol{\lambda}/|\boldsymbol{\lambda}|$ if $\mathbf{e}_s$ and $\boldsymbol{\lambda}$ are parallel vectors. This observation may suggest the following approximate approach to (11.54)

$$\begin{aligned} k\mathbf{e}_f &= -\mu_1 p \frac{\boldsymbol{\lambda} - \mathbf{e}_f'}{|\boldsymbol{\lambda} - \mathbf{e}_f'|} \\ k\tilde{\mathbf{e}}_s &= -\mu_1 p \frac{\mathbf{e}_f}{|\mathbf{e}_f|} \end{aligned} \tag{11.66}$$

First we solve two *separate linear* differential equations (not a system) for the two components of the "fictitious" deflection $\mathbf{e}_f$. Then, we obtain the *approximate* deflection $\tilde{\mathbf{e}}_s$ in the sliding region as a vector with magnitude $\mu_1 p/k$ and directed like $\mathbf{e}_f$. We remind that linear first-order differential equations can always be solved by integration (see, e.g., [12, p. 410]).[9] In many cases $\tilde{\mathbf{e}}_s$ is a very good approximation of $\mathbf{e}_s$.

[9] The solution of $y' + f(x)y = g(x)$ is

$$y(x) = \exp\left(-\int^x f(t)\mathrm{d}t\right)\left[\int^x \exp\left(\int^z f(t)\mathrm{d}t\right) g(z)\mathrm{d}z + C\right].$$

An even simpler, less accurate, but often employed idea is to assume that the governing equation in the sliding state is just an algebraic equation

$$k\hat{\mathbf{e}}_s = -\mu_1 p \frac{\boldsymbol{\lambda}}{|\boldsymbol{\lambda}|} \tag{11.67}$$

Therefore, we allow a sudden discontinuity in the direction of the deflection at the transition from adhesion to sliding. This is not correct, but very appealing because of its simplicity. Of course, as already mentioned, (11.67) is exact if $\mathbf{e}_s$ and $\boldsymbol{\lambda}$ happen to be parallel throughout the whole sliding region, that is if $\varphi = 0$ and hence $\boldsymbol{\lambda} = \boldsymbol{\sigma}$.

11.3.3 Force–Couple Resultant

The solution of the steady-state brush model shows whether there is adhesion or sliding at each point of the contact patch $\mathscr{P}$ and provides the corresponding bristle deflection $\mathbf{e}_a(\hat{x}, \hat{y})$ or $\mathbf{e}_s(\hat{x}, \hat{y})$. Therefore, the tangential stress $\mathbf{t}$ at each point of $\mathscr{P}$ is

$$\mathbf{t}(\hat{x}, \hat{y}) = \begin{cases} \mathbf{t}_a = k\mathbf{e}_a(\hat{x}, \hat{y}) & \text{(adhesion)} \\ \mathbf{t}_s = k\mathbf{e}_s(\hat{x}, \hat{y}) & \text{(sliding)} \end{cases} \tag{11.68}$$

Like in (2.16) and (11.10), the tangential force $\mathbf{F}_t = F_x\,\mathbf{i} + F_y\,\mathbf{j}$ that the road applies on the tire model is given by the integral of $\mathbf{t}$ over the contact patch

$$\mathbf{F}_t(\boldsymbol{\sigma}, \varphi) = \int_{-b}^{b} \mathrm{d}\hat{y} \int_{-\hat{x}_0(\hat{y})}^{\hat{x}_0(\hat{y})} \mathbf{t}(\hat{x}, \hat{y})\mathrm{d}\hat{x} \tag{11.69}$$

which is a function, among other things, of the global slips $\boldsymbol{\sigma}$ and φ.[10]

It may be convenient to use the nondimensional or *normalized* tangential force $\mathbf{F}_t^n$ and its components [7]

$$\mathbf{F}_t^n = F_x^n\,\mathbf{i} + F_y^n\,\mathbf{j} = \frac{\mathbf{F}_t}{F_z} = \frac{F_x\,\mathbf{i} + F_y\,\mathbf{j}}{F_z} \tag{11.70}$$

Of course, under whichever operating condition of the brush model, we always have $|\mathbf{F}_t^n| < \mu_0$. It is quite interesting to find the combination of σ_x, σ_y and φ which

[10] Since the tangential force is constant in time, it is possible to exploit its dependence on the given slips.

provides the highest possible value. Equations (2.90) and (2.92) address a similar issue in an experimental context.

The overall moment of the tangential stresses with respect to point D is given by

$$M_z^D(\boldsymbol{\sigma}, \varphi)\,\mathbf{k} = \int_{-b}^{b} \mathrm{d}\hat{y} \int_{-\hat{x}_0(\hat{y})}^{\hat{x}_0(\hat{y})} (\hat{x}\,\mathbf{i} + \hat{y}\,\mathbf{j}) \times \mathbf{t}(\hat{x}, \hat{y})\mathrm{d}\hat{x} \tag{11.71}$$

However, in general, we are more interested in the vertical moment (usually called self-aligning torque) M_z, that is the moment with respect to the origin O of S. According to (11.12) and (11.14), we have to take into account the effects of the carcass compliance and of camber (Fig. 2.16) to locate D with respect to O

$$\begin{aligned} M_z(\gamma, \boldsymbol{\sigma}, \varphi) &= M_z^D - F_x(c_r(\gamma) + q_y) + F_y q_x \\ &= M_z^D - F_x\left(c_r(\gamma) + \frac{F_y}{w_y}\right) + F_y\frac{F_x}{w_x} \\ &= M_z^D - F_x c_r(\gamma) + F_x F_y \frac{w_y - w_x}{w_x w_y} \end{aligned} \tag{11.72}$$

11.3.4 Examples of Tangential Stress Distributions

To gain insights into the steady-state brush model behavior, we will address some particular cases. Some of them can be solved analytically, while others require a numerical approach.

The shape of the contact patch is taken to be rectangular or elliptical, although it would not be much more difficult to deal with more realistic shapes, like the one in the center of Fig. 11.3.

Figure 11.10, obtained with the data listed in (11.49), shows the tangential stress pattern in *rectangular* contact patches, along with the adhesion and sliding regions, for four combinations of $(\sigma_x, \sigma_y, \varphi)$. The corresponding values of the normalized longitudinal and lateral forces are also reported. As typical in car tires, the value of φ is small.

Exactly the same combinations of slips, but for *rounded rectangular* contact patches, are shown in Fig. 11.11.

In Fig. 11.12, four cases for *elliptical* contact patches are shown. In these cases, the spin slip φ is quite high, as typical in motorcycle tires.

As expected, large values of φ make the stress distributions strongly non-parallel, thus reducing the value of the maximum achievable resultant tangential force.

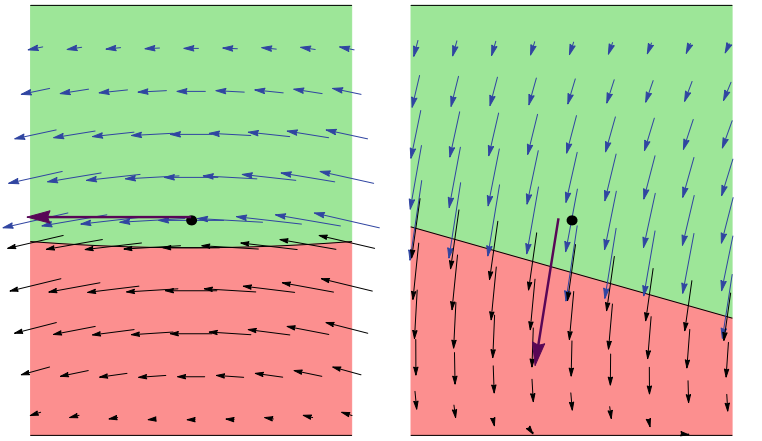

(a) $(\sigma_x, \sigma_y, \varphi) = (0, -0.1, 0.5)$, $(F_x^n, F_y^n) = (0, 0.77)$

(b) $(\sigma_x, \sigma_y, \varphi) = (0.1, 0, 0.5)$, $(F_x^n, F_y^n) = (-0.69, 0.11)$

(c) $(\sigma_x, \sigma_y, \varphi) = (0.1, -0.1, 0)$, $(F_x^n, F_y^n) = (-0.57, 0.57)$

(d) $(\sigma_x, \sigma_y, \varphi) = (0.1, -0.1, 0.5)$, $(F_x^n, F_y^n) = (-0.54, 0.63)$

Fig. 11.10 Examples of tangential stress distributions in rectangular contact patches. Also shown the line separating the adhesion region (top) and the sliding region (bottom), and the components of the normalized tangential force. Values of φ are in m^{-1}

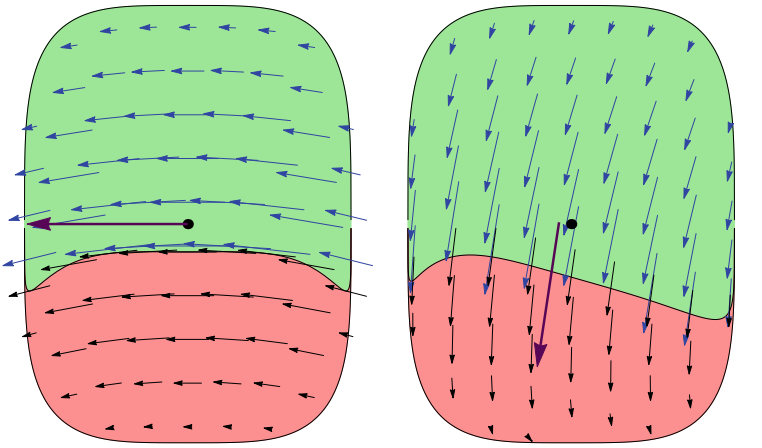

(a) $(\sigma_x, \sigma_y, \varphi) = (0, -0.1, 0.5)$, $(F_x^n, F_y^n) = (0, 0.74)$

(b) $(\sigma_x, \sigma_y, \varphi) = (0.1, 0, 0.5)$, $(F_x^n, F_y^n) = (-0.67, 0.10)$

(c) $(\sigma_x, \sigma_y, \varphi) = (0.1, -0.1, 0)$, $(F_x^n, F_y^n) = (-0.55, 0.55)$

(d) $(\sigma_x, \sigma_y, \varphi) = (0.1, -0.1, 0.5)$, $(F_x^n, F_y^n) = (-0.53, 0.61)$

Fig. 11.11 Examples of tangential stress distributions in rounded rectangular contact patches. Also shown the line separating the adhesion region (top) and the sliding region (bottom), and the components of the normalized tangential force. Values of φ are in m^{-1}

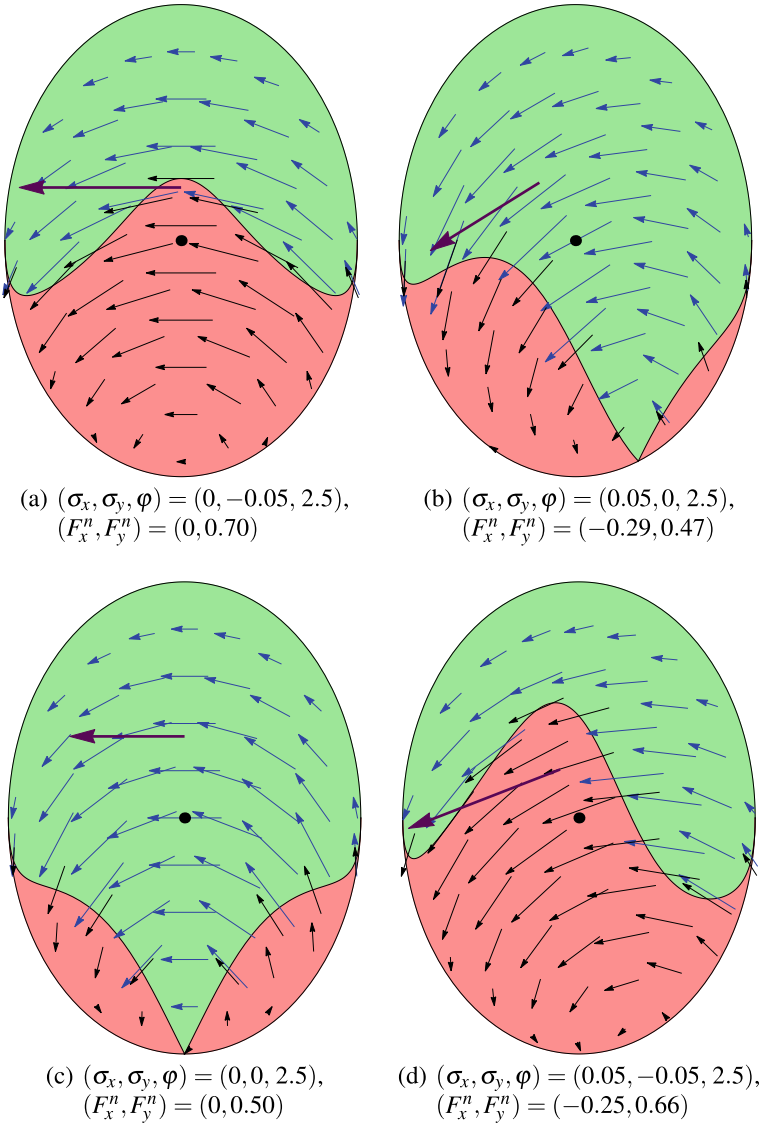

(a) $(\sigma_x, \sigma_y, \varphi) = (0, -0.05, 2.5)$, $(F_x^n, F_y^n) = (0, 0.70)$

(b) $(\sigma_x, \sigma_y, \varphi) = (0.05, 0, 2.5)$, $(F_x^n, F_y^n) = (-0.29, 0.47)$

(c) $(\sigma_x, \sigma_y, \varphi) = (0, 0, 2.5)$, $(F_x^n, F_y^n) = (0, 0.50)$

(d) $(\sigma_x, \sigma_y, \varphi) = (0.05, -0.05, 2.5)$, $(F_x^n, F_y^n) = (-0.25, 0.66)$

Fig. 11.12 Examples of tangential stress distributions in elliptical contact patches. Also shown the line separating the adhesion region (top) and the sliding region(s) (bottom), and the components of the normalized tangential force. Values of φ are in m^{-1} and correspond to a camber angle of about 38 degrees

11.4 Adhesion Everywhere (Linear Behavior)

If the magnitude of the skating slip $\boldsymbol{\lambda}$ is everywhere very small, then there is adhesion almost everywhere in the contact patch. More precisely, small skating slips means

$$|\boldsymbol{\lambda}| \ll \frac{\mu_0 p_0}{2ak} \tag{11.73}$$

that is $|\boldsymbol{\lambda}| < 0.03$ on a dry paved road. Of course, we are still dealing with steady-state conditions.

According to (11.55) and (11.69), the tangential force is

$$\begin{aligned}
\mathbf{F}_t(\boldsymbol{\sigma}, \varphi) &= F_x\,\mathbf{i} + F_y\,\mathbf{j} = \int_{-b}^{b} \mathrm{d}\hat{y} \int_{-\hat{x}_0(\hat{y})}^{\hat{x}_0(\hat{y})} k\mathbf{e}_a(\hat{x}, \hat{y})\mathrm{d}\hat{x} \\
&= \int_{-b}^{b} \mathrm{d}\hat{y} \int_{-\hat{x}_0}^{\hat{x}_0} k \left(-\boldsymbol{\sigma}(\hat{x}_0 - \hat{x}) + \varphi \left[\frac{(\hat{x}_0 - \hat{x})(\hat{x}_0 + \hat{x})}{2}\,\mathbf{j} - \hat{y}(\hat{x}_0 - \hat{x})\,\mathbf{i} \right] \right) \mathrm{d}\hat{x} \\
&= -C_\sigma \boldsymbol{\sigma} + C_\varphi \varphi\,\mathbf{j} \\
&= -C_\sigma \sigma_x\,\mathbf{i} - (C_\sigma \sigma_y - C_\varphi \varphi)\,\mathbf{j}
\end{aligned} \tag{11.74}$$

which, as expected, is *linear* in both $\boldsymbol{\sigma}$ and φ. This is a crude approximation of the real tire behavior, unless all the force components are very small.

It is worth noting that the longitudinal force F_x is a function of σ_x only, whereas the lateral force F_y depends on both σ_y and φ.

The coefficient C_σ may be called *slip stiffness*. In the isotropic brush model, C_σ is the same for any direction of the tangential force, that is for any combination of σ_x and σ_y. Moreover, in the brush model

$$C_\sigma = C_\alpha = C_{\kappa_x} \tag{11.75}$$

where C_α and C_{κ_x} were defined in (2.91) and (2.89).

The coefficient C_φ is the *spin stiffness* for the lateral force. Owing to the symmetric shape of the contact patch, the spin slip does not contribute to the longitudinal force.

It is possible to insert (2.78) and (2.79), that is the practical slip components, into (11.74), but the resulting function is no longer linear

$$\mathbf{F}_t(\boldsymbol{\kappa}, \varphi) = F_x\,\mathbf{i} + F_y\,\mathbf{j} = -C_\sigma \frac{\kappa_x\,\mathbf{i} + \kappa_y\,\mathbf{j}}{1 - \kappa_x} + C_\varphi \varphi\,\mathbf{j} \tag{11.76}$$

Once again, the practical slip does not do a good job.

As shown in (2.71),

$$\varphi = -\frac{\sin\gamma(1 - \varepsilon_r)}{r_r} \tag{2.71'}$$

if the yaw rate ω_z is zero or at least negligible (as discussed at p. 41), the spin slip φ becomes a function of the camber angle γ only (besides F_z). In this case, we can define the *camber stiffness* C_γ

$$C_\gamma = -\frac{C_\varphi}{r_r}(1-\varepsilon_r) < 0 \tag{11.77}$$

and obtain ($\sin\gamma \approx \gamma$)

$$\mathbf{F}_t(\boldsymbol{\sigma}, \gamma) = F_x\,\mathbf{i} + F_y\,\mathbf{j} = -C_\sigma(\sigma_x\,\mathbf{i} + \sigma_y\,\mathbf{j}) + C_\gamma\gamma\,\mathbf{j} \tag{11.78}$$

Typically, $F_z/C_\gamma \approx 1$ for a motorcycle tire. Quite often, $-C_\sigma\sigma_y\,\mathbf{j}$ is called *cornering force* and $C_\gamma\gamma\,\mathbf{j}$ is called *camber force* (or camber thrust). Obviously, only under the very strong assumption of adhesion all over the contact patch, that is for very small values of the skating slip $\boldsymbol{\lambda}$, we have two separate and independent contributions to the lateral force.

Under the same conditions and according to (11.72) we can compute the vertical moment with respect to the center D of the contact patch

$$\begin{aligned} M_z^D(\sigma_y, \varphi)\,\mathbf{k} &= \int_{-b}^{b} \mathrm{d}\hat{y} \int_{-\hat{x}_0(\hat{y})}^{\hat{x}_0(\hat{y})} (\hat{x}\,\mathbf{i} + \hat{y}\,\mathbf{j}) \times k\mathbf{e}_a(\hat{x}, \hat{y})\mathrm{d}\hat{x} \\ &= \left(C_{M_\sigma}\sigma_y + C_{M_\varphi}\varphi\right)\mathbf{k} = -F_y t_c\,\mathbf{k} \end{aligned} \tag{11.79}$$

where t_c is the *pneumatic trail* with respect to the contact center D. The last expression states quite a remarkable fact: that $F_y = 0$ means $M_z^D = 0$ as well. The minus sign makes $t_c > 0$ under standard operating conditions.

Combining (11.72), (11.74) and (11.79) we obtain the vertical moment with respect to point O

$$M_z(\gamma, \boldsymbol{\sigma}, \varphi) = C_{M_\sigma}\sigma_y + C_{M_\varphi}\varphi + C_\sigma\sigma_x\left[c_r(\gamma) + \frac{w_x - w_y}{w_x w_y}(-C_\sigma\sigma_y + C_\varphi\varphi)\right] \tag{11.80}$$

For a *rectangular* contact patch (i.e., $x_0(\hat{y}) = a$) we have

$$C_\sigma = 4ka^2b \tag{11.81}$$

and

$$C_\varphi = C_{M_\sigma} = \frac{a}{3}C_\sigma \qquad C_{M_\varphi} = \frac{b^2}{3}C_\sigma \qquad C_\gamma = -\frac{a(1-\varepsilon_r)}{3r_r}C_\sigma \tag{11.82}$$

Typically, $C_\gamma \ll |C_\sigma|$. From (11.74) (11.79) and (11.82) we can obtain the pneumatic trail t_c for a rectangular contact patch

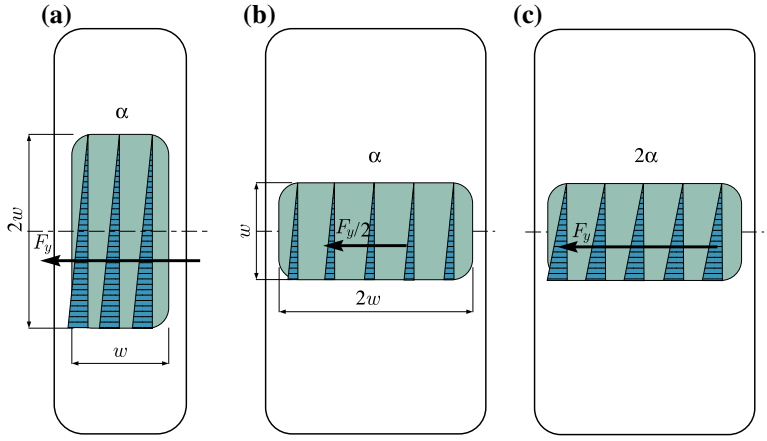

Fig. 11.13 Comparison of tires with the same F_z, p_0 and k, but different width

$$t_c = \frac{\sigma_y a + \varphi b^2}{3(\sigma_y - \varphi a)} \tag{11.83}$$

Special, but quite important cases are:
$\varphi = 0$, which yields

$$t_c = \frac{a}{3} \tag{11.84}$$

and $\sigma_y = 0$, that yields

$$t_c = -\frac{b^2}{3a} \tag{11.85}$$

For an *elliptical* contact patch the algebra is a bit more involved. The final expression of the tangential force $\mathbf{F}_t$ is exactly like in (11.74), but with the following stiffnesses

$$C_\sigma = \frac{8}{3} k a^2 b \quad \text{and} \quad C_\varphi = C_{M_\sigma} = \frac{3\pi a}{32} C_\sigma \tag{11.86}$$

We recall that the contact patch has length $2a$ and width $2b$. The product ab, and hence also the area of the contact patch, are determined by the vertical load F_z and the tire inflation pressure p_0, as obtained in (11.6) and (11.9). However, in the expressions (11.81) and (11.86) of the slip stiffness C_σ there appear the term $a^2 b = a(ab)$. That means that the aspect ratio a/b of the footprint does affect C_σ. The reason for this dependence is promptly explained with the aid of Fig. 11.13.

If we compare Fig. 11.13a and b, we see that, for given slip angle α, the longer the footprint, the higher the final deflection of the bristles. This phenomenon is partly compensated by the fact that bristle deflections act on a wider strip in case (b). As predicted by (11.81), the net result is that tire (a) has a slip stiffness C_σ twice as much

as tire (b). In other words, to obtain the same lateral force F_y from the wider tire we need to double the slip angle, as shown in Fig. 11.13c.

All tires in Fig. 11.13 share the same F_z, p_0 and k.

11.5 Translational Slip Only ($\sigma \neq 0$, $\varphi = 0$)

The investigation of the steady-state behavior of the brush model is much simpler if there is no spin slip φ. Indeed, the first two figures in this chapter referred to the case of pure braking. It is not a bad idea to go back and have another look.

According to (11.27), if $\varphi = 0$ and $\dot{\mathbf{q}} = \mathbf{0}$ all points in the contact patch $\mathscr{P}$ have the same skating velocity $\mathbf{V}_s^P = \mathbf{V}_s$. Therefore, from (11.50) we obtain that the skating slip $\boldsymbol{\lambda}$ is equal to the translational slip $\boldsymbol{\sigma}$

$$\boldsymbol{\lambda} = \boldsymbol{\sigma} \tag{11.87}$$

and the governing equation (11.53) in the *adhesion* region becomes (Fig. 11.14)

$$\mathbf{e}_a' = \boldsymbol{\sigma} = \text{ const.} \tag{11.88}$$

whose solution, which is a *linear* function of $\hat{x}$, is readily obtained as a special case of (11.55)

$$\mathbf{e}_a(\hat{x}, \hat{y}) = -(\hat{x}_0(\hat{y}) - \hat{x})\boldsymbol{\sigma} = -(\hat{x}_0(\hat{y}) - \hat{x})\sigma\mathbf{s} \tag{11.89}$$

As shown in Fig. 11.14, all vectors $\mathbf{e}_a$ have the *same direction* $\mathbf{s} = \boldsymbol{\sigma}/\sigma$, with $\sigma = |\boldsymbol{\sigma}|$. Moreover, they grow linearly in the adhesion region. A look at Fig. 11.14 should clarify the matter.

The physical interpretation of these equations is simply that in the adhesion region everything is ruled by the kinematics of the wheel.

Like in (11.57), the adhesion state is maintained up to $\hat{x}_s = \hat{x}_s(\sigma, \hat{y})$, which marks the point where the friction limit is reached (Fig. 11.14)

$$k|\mathbf{e}_a(\hat{x}_s, \hat{y})| = \kappa\sigma\,(\hat{x}_0(\hat{y}) - \hat{x}_s) = \mu_0 p(\hat{x}_s, \hat{y}) \tag{11.90}$$

For the parabolic pressure distribution (11.3) we obtain

$$\hat{x}_s(\sigma, \hat{y}) = \hat{x}_0(\hat{y})\left[\frac{\kappa\hat{x}_0(\hat{y})}{\mu_0 p_0(\hat{y})}\,\sigma - 1\right] \tag{11.91}$$

It is worth noting that, if $\varphi = 0$, the line separating the adhesion and the sliding regions depends solely on the magnitude σ of the slip. It is not affected by the direction $\mathbf{s}$ of $\boldsymbol{\sigma}$. However, this separating line depends on the shape of the contact patch. It is a straight line for a rectangular footprint, as in Fog. 11.14. For an elliptical contact

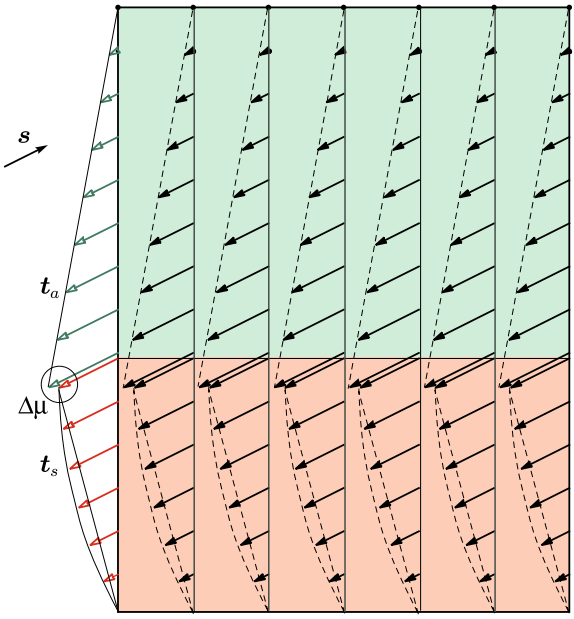

Fig. 11.14 Linear pattern in the adhesion region and parabolic pattern in the sliding region

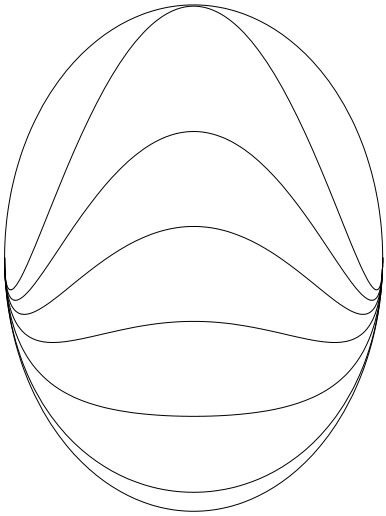

Fig. 11.15 Lines separating the adhesion region (top) and the sliding region (bottom) for $\sigma = (0.01, 0.05, 0.10, 0.15, 0.20, 0.266)$ and $\varphi = 0$. Pressure distribution as in (11.8)

patch, Figure 11.15 shows the lines between adhesion and sliding for a sequence of growing values of σ.

At $\hat{x}_s$ the friction coefficient switches from μ_0 to its kinetic value μ_1, and the sliding state starts according to (11.58), that is with a *parabolic* pattern (Fig. 11.14)

$$k\mathbf{e}_s(\hat{x}_s, \hat{y}) = -\mu_1 p(\hat{x}_s, \hat{y})\mathbf{s} \tag{11.92}$$

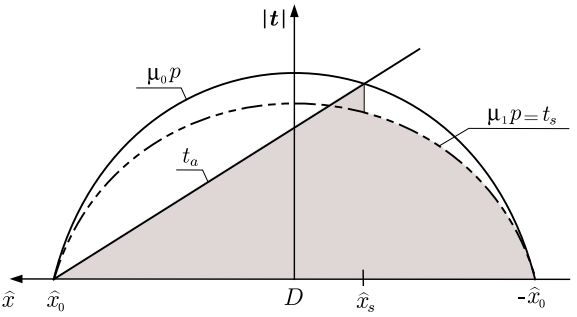

Fig. 11.16 Typical pattern of the tangential stress in the adhesion region (left) and in the sliding region (right)

The really important aspect is that sliding begins with the bristle deflection $\mathbf{e}_a$ that has already the *same direction* $\mathbf{s}$ as $\boldsymbol{\lambda} = \boldsymbol{\sigma}$. Therefore, also $\mathbf{e}'_s$ is directed like $\mathbf{s}$, and the governing equation (11.54) (or (11.59)) for the *sliding* region becomes simply

$$k\mathbf{e}_s(\hat{x}, \hat{y}) = -\mu_1 p(\hat{x}, \hat{y})\mathbf{s} \tag{11.93}$$

which is no longer a differential equation. Actually this is already the definition of $\mathbf{e}_s$ in the sliding region.

Equations (11.89) and (11.93) provide the complete solution for this case. Therefore, the tangential stress $\mathbf{t}$ at each point of the contact patch $\mathscr{P}$ is given by (Fig. 11.14)

$$\mathbf{t}(\hat{x}, \hat{y}) = \begin{cases} \mathbf{t}_a = -t_a\mathbf{s} = -(\hat{x}_0(\hat{y}) - \hat{x})\sigma k\,\mathbf{s}, & \text{(adhesion)} \\ \mathbf{t}_s = -t_s\mathbf{s} = -\mu_1 p(\hat{x}, \hat{y})\,\mathbf{s}, & \text{(sliding)} \end{cases} \tag{11.94}$$

where $\mathbf{s} = \boldsymbol{\sigma}/\sigma$, $t_a = |\mathbf{t}_a|$ and $t_s = |\mathbf{t}_s|$. Actually, as in Fig. 11.16, we have assumed that, for any $\hat{y}$, a single adhesion region ($\hat{x}_s(\sigma, \hat{y}) \leq \hat{x} \leq \hat{x}_0(\hat{y})$) is followed by a single sliding region ($-\hat{x}_0(\hat{y}) \leq \hat{x} < \hat{x}_s(\sigma, \hat{y})$), as it is normally the case. However, as shown in Figure 11.9 for a fairly unrealistic pressure distribution, it is possible, at least in principle, to have multiple regions.

Summing up, we have the following features (Figs. 11.14, 11.16 and 11.17):

- the tangential stress $\mathbf{t}$ is directed like $\boldsymbol{\sigma}$, with opposite sign;
- t_a grows linearly in the adhesion region;
- t_s follows the $\mu_1 p$ parabolic pattern in the sliding region;
- both t_a and t_s are not affected by the direction of $\boldsymbol{\sigma}$;
- the higher σ, the steeper the growth of t_a and hence the closer the transition point $\hat{x}_s$ to the leading edge $\hat{x}_0$.

All these features can be appreciated in Figs. 11.18 and 11.19, which show the tangential stress pattern, as predicted by the brush model, in rectangular and elliptical contact patches under pure *translational* slip $\boldsymbol{\sigma}$. It is worth remarking that in each contact patch all arrows are parallel to each other.

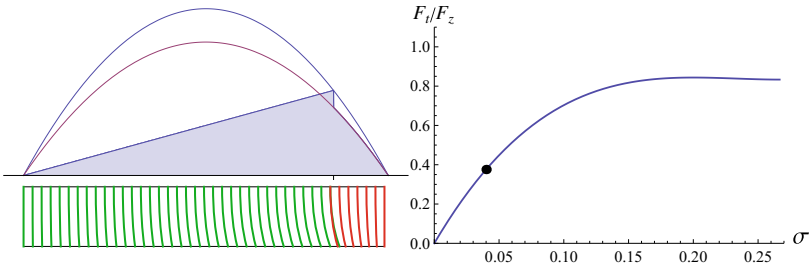

(a) $\sigma = 0.04$: almost linear behavior

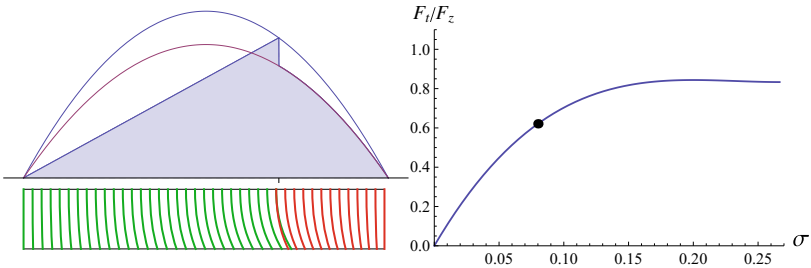

(b) $\sigma = 0.08$: non-linear behavior

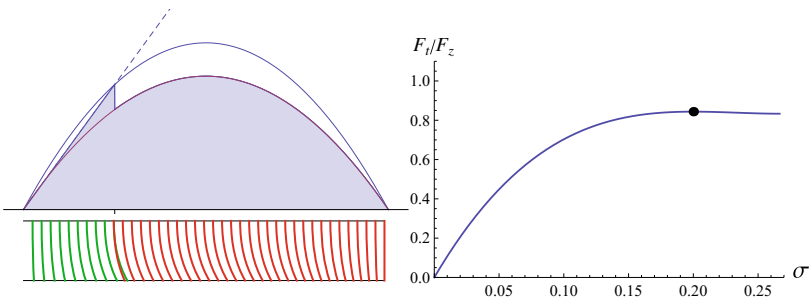

(c) $\sigma = 0.20$: maximum tangential force

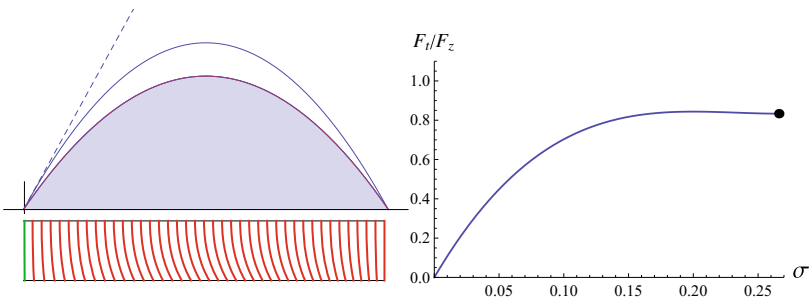

(d) $\sigma = 0.26$: all bristle tips are sliding on the road (but the wheel is not locked)

Fig. 11.17 Brush model for rectangular contact patch under braking conditions. The shaded area (left) is proportional to the global tangential force F_t, marked by a point on the plot (right). Green bristles have the tip stuck to the ground, red bristles have the tip sliding on the ground

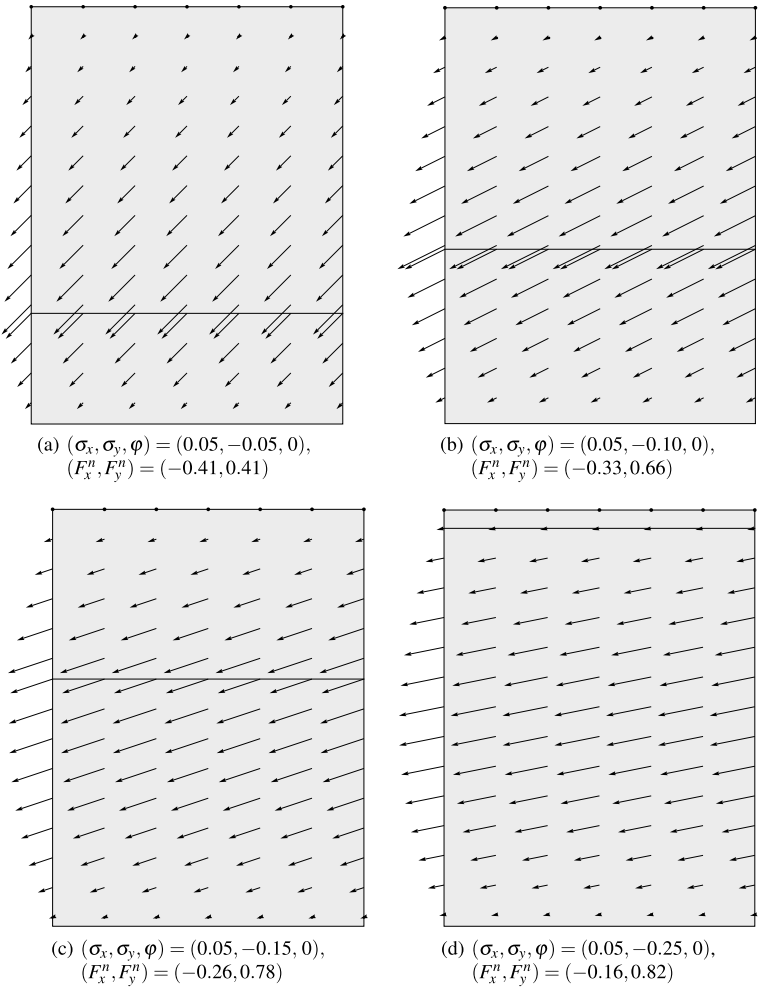

(a) $(\sigma_x, \sigma_y, \varphi) = (0.05, -0.05, 0)$, $(F_x^n, F_y^n) = (-0.41, 0.41)$

(b) $(\sigma_x, \sigma_y, \varphi) = (0.05, -0.10, 0)$, $(F_x^n, F_y^n) = (-0.33, 0.66)$

(c) $(\sigma_x, \sigma_y, \varphi) = (0.05, -0.15, 0)$, $(F_x^n, F_y^n) = (-0.26, 0.78)$

(d) $(\sigma_x, \sigma_y, \varphi) = (0.05, -0.25, 0)$, $(F_x^n, F_y^n) = (-0.16, 0.82)$

Fig. 11.18 Examples of tangential stress distributions in rectangular contact patches under *pure translational slip* $\boldsymbol{\sigma}$. All arrows have the same direction. Also shown is the line separating the adhesion region (top) and the sliding region (bottom)

The global tangential force $\mathbf{F}_t = F_x\,\mathbf{i} + F_y\,\mathbf{j}$ that the road applies to the tire model is given by the integral of $\mathbf{t}$ on the contact patch, like in (11.69). Of course, here the analysis will provide $\mathbf{F}_t(\boldsymbol{\sigma}, 0)$. Since all tangential stresses $\mathbf{t}$ have the same direction $-\mathbf{s}$, the computation simply amounts to integrating $|\mathbf{t}|$ (shaded area in Figs. 11.16 and 11.17)

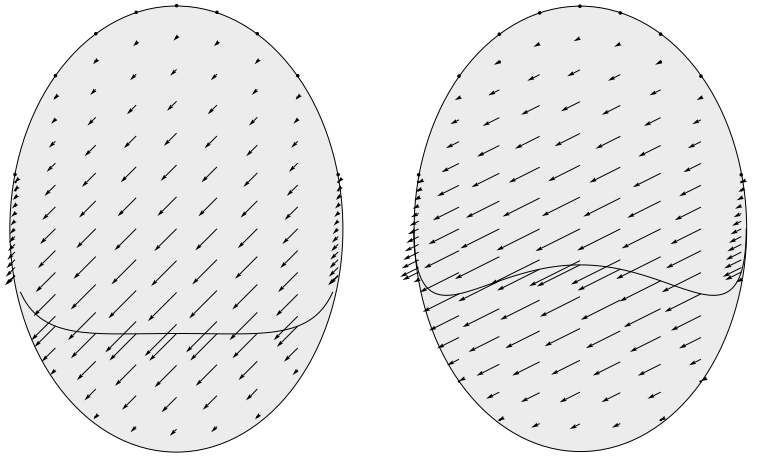

(a) $(\sigma_x, \sigma_y, \varphi) = (0.05, -0.05, 0)$, $(F_x^n, F_y^n) = (-0.36, 0.36)$

(b) $(\sigma_x, \sigma_y, \varphi) = (0.05, -0.10, 0)$, $(F_x^n, F_y^n) = (-0.30, 0.60)$

(c) $(\sigma_x, \sigma_y, \varphi) = (0.05, -0.15, 0)$, $(F_x^n, F_y^n) = (-0.25, 0.76)$

(d) $(\sigma_x, \sigma_y, \varphi) = (0.05, -0.25, 0)$, $(F_x^n, F_y^n) = (-0.16, 0.81)$

Fig. 11.19 Examples of tangential stress distributions in elliptical contact patches under *pure translational slip* $\boldsymbol{\sigma}$. All arrows have the same direction. Also shown is the line separating the adhesion region (top) and the sliding region (bottom)

$$\mathbf{F}_t = -\mathbf{s}\, F_t(\sigma) = -\mathbf{s}\left[\int_{-b}^{b} \mathrm{d}\hat{y} \int_{\hat{x}_s(\sigma,\hat{y})}^{\hat{x}_0(\hat{y})} t_a(\sigma, \hat{x}, \hat{y})\mathrm{d}\hat{x} + \int_{-b}^{b} \mathrm{d}\hat{y} \int_{-\hat{x}_0(\hat{y})}^{\hat{x}_s(\sigma,\hat{y})} t_s(\hat{x}, \hat{y})\mathrm{d}\hat{x}\right] \tag{11.95}$$

where $F_t = |\mathbf{F}_t|$. The two components, that is the longitudinal force F_x and the lateral force F_y, are given by

$$\begin{aligned} F_x &= F_x(\sigma_x, \sigma_y) = -\frac{\sigma_x}{\sigma} F_t(\sigma), \\ F_y &= F_y(\sigma_x, \sigma_y) = -\frac{\sigma_y}{\sigma} F_t(\sigma) \end{aligned} \tag{11.96}$$

which imply $\sigma_x / F_x = \sigma_y / F_y$.

Summing up, in the brush model with $\varphi = 0$, the magnitude $F_t(\sigma)$ of the tangential force $\mathbf{F}_t$ depends on the magnitude $\sigma = \sqrt{\sigma_x^2 + \sigma_y^2}$ of the translational slip, and the vectors $\mathbf{F}_t$ and $\boldsymbol{\sigma}$ have the same direction, but opposite signs

$$\mathbf{F}_t = -\frac{\boldsymbol{\sigma}}{\sigma} F_t(\sigma) \tag{11.97}$$

In practical applications, it is a good idea to employ the Magic Formula for $F_t(\sigma)$ in (11.96), since it follows better the real tire behavior.

Partial derivatives can be readily obtained from (11.96)

$$\begin{aligned} -\frac{\partial F_x}{\partial \sigma_x} &= \frac{\partial}{\partial \sigma_x}\left(\frac{\sigma_x}{\sigma} F_t(\sigma)\right) = \left(\frac{\sigma_x}{\sigma}\right)^2 \left(F_t' - \frac{F_t}{\sigma}\right) + \frac{F_t}{\sigma} \\ -\frac{\partial F_x}{\partial \sigma_y} &= \frac{\partial}{\partial \sigma_y}\left(\frac{\sigma_x}{\sigma} F_t(\sigma)\right) = \left(\frac{\sigma_x \sigma_y}{\sigma^2}\right) \left(F_t' - \frac{F_t}{\sigma}\right) \end{aligned} \tag{11.98}$$

Those of F_y simply need interchanging x and y.

Equation (11.71) provides the vertical moment M_z^D with respect to point D. However, it can be considerably simplified in the case of $\varphi = 0$. As a matter of fact, we see from (11.94) that $\mathbf{t}(\hat{x}, \hat{y}) = \mathbf{t}(\hat{x}, -\hat{y})$[11] and hence

$$M_z^D(\sigma_x, \sigma_y) = -\frac{\sigma_y}{\sigma} \left[\int_{-b}^{b} \mathrm{d}\hat{y} \int_{\hat{x}_s(\sigma, \hat{y})}^{\hat{x}_0(\hat{y})} \hat{x}\, t_a(\sigma, \hat{x}, \hat{y}) \mathrm{d}\hat{x} + \int_{-b}^{b} \mathrm{d}\hat{y} \int_{-\hat{x}_0(\hat{y})}^{\hat{x}_s(\sigma, \hat{y})} \hat{x}\, t_s(\hat{x}, \hat{y}) \mathrm{d}\hat{x} \right] \tag{11.99}$$

It may be convenient to recast this equation in the following form

$$M_z^D(\sigma_x, \sigma_y) = \frac{\sigma_y}{\sigma} F_t(\sigma)\, t_c(\sigma) = -F_y(\sigma_x, \sigma_y)\, t_c(\sigma) \tag{11.100}$$

which is, indeed, the definition of the *pneumatic trail* t_c, that is the (signed) distance from the contact center D of the line of action of the lateral force $F_y \mathbf{j}$. As shown in Fig. 11.20, a positive t_c stands for a lateral force behind D, which is the standard case.

[11] If, as usual, also $\hat{x}_0(\hat{x}, \hat{y}) = \hat{x}_0(\hat{x}, -\hat{y})$ and $p(\hat{x}, \hat{y}) = p(\hat{x}, -\hat{y})$.

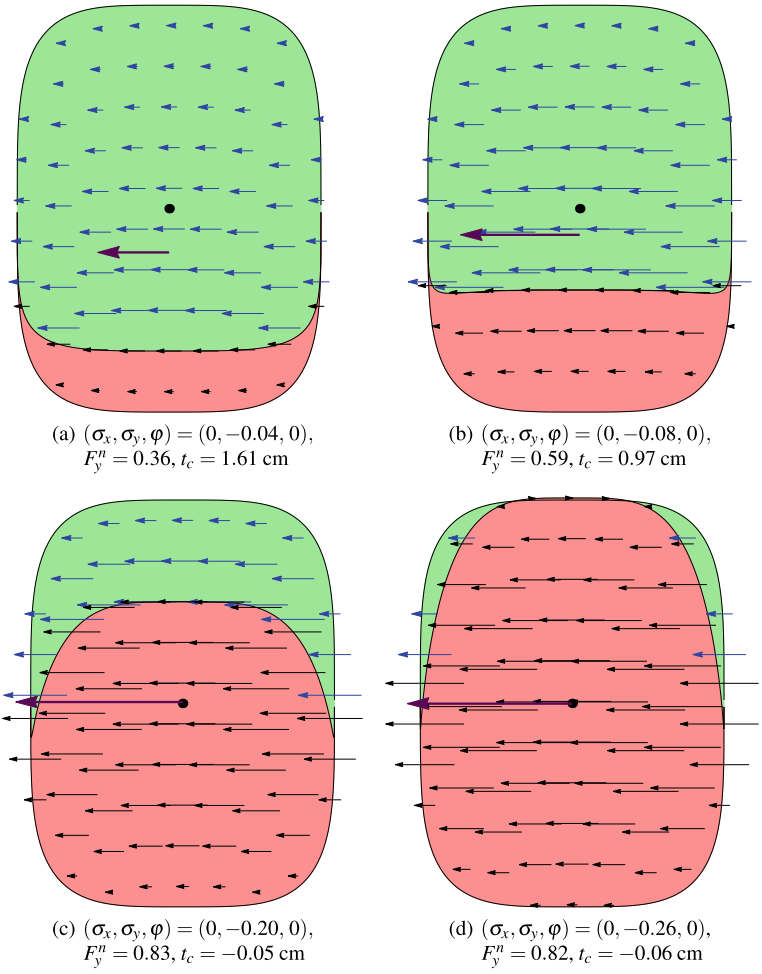

(a) $(\sigma_x, \sigma_y, \varphi) = (0, -0.04, 0)$, $F_y^n = 0.36$, $t_c = 1.61$ cm

(b) $(\sigma_x, \sigma_y, \varphi) = (0, -0.08, 0)$, $F_y^n = 0.59$, $t_c = 0.97$ cm

(c) $(\sigma_x, \sigma_y, \varphi) = (0, -0.20, 0)$, $F_y^n = 0.83$, $t_c = -0.05$ cm

(d) $(\sigma_x, \sigma_y, \varphi) = (0, -0.26, 0)$, $F_y^n = 0.82$, $t_c = -0.06$ cm

Fig. 11.20 Tangential stress distributions in rounded rectangular contact patches under pure lateral slip σ_y. Also shown the global tangential force. Values of σ as in Fig. 11.17

11.5.1 Rectangular Contact Patch

Assuming a rectangular shape (Fig. 11.3) essentially means setting $\hat{x}_0(\hat{y}) = a$ as the equation of the leading edge. Therefore, any dependence on $\hat{y}$ disappears and the problem becomes one-dimensional, that is $\mathbf{e}_a = \mathbf{e}_a(\hat{x})$ and $\mathbf{e}_s = \mathbf{e}_s(\hat{x})$.

As shown in Fig. 11.18, in this case the line between the adhesion and the sliding regions is simply a *straight line* directed like $\mathbf{j}$

$$\hat{x}_s(\sigma) = a\left(\frac{\kappa a}{\mu_0 p_0}\,\sigma - 1\right) = a\left(2\frac{\sigma}{\sigma_s} - 1\right) \tag{11.101}$$

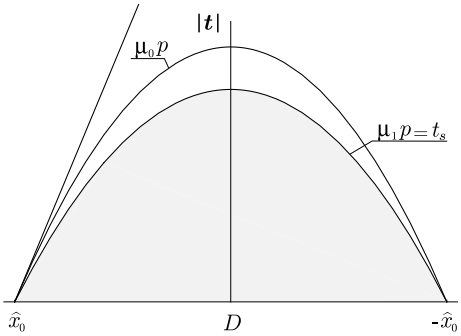

Fig. 11.21 Tangential stress if $\sigma = \sigma_s$ (total sliding)

where

$$\sigma_s = \frac{2\mu_0 p_0}{ka} = \frac{3\mu_0 F_z}{C_\sigma} = \frac{\mu_0}{k}|p'(a)| \tag{11.102}$$

with the slip stiffness C_σ defined in (11.75).

The physical interpretation of σ_s is promptly obtained. If $\sigma \geq \sigma_s$, regardless of the direction of $\boldsymbol{\sigma}$, there is sliding on the whole rectangular contact patch, that is $\hat{x}_s = a$. For instance, with the numerical values of (11.49) on p. 477, we have $\sigma_s = 0.27$, that is a fairly low value.

At first, it may be surprising to have full sliding without wheel locking (i.e., $\sigma = \infty$). The phenomenon is explained in Fig. 11.21 (and also in Fig. 11.17d): to have total sliding it suffices that the straight line to be tangent to the upper parabola at the leading edge. The value (11.102) of σ_s predicted by the brush model is therefore quite "weak", in the sense that it is very much affected by the assumed pressure distribution. However, the existence of full sliding without (necessarily) wheel locking is an important result.

Also interesting is to observe that

$$\sigma_s C_\sigma = 3\mu_0 F_z \tag{11.103}$$

A simple formula that shows the strong relationship between σ_s and C_σ: the stiffer the tire, the smaller σ_s. The quantity μ_1 plays no role.

Application of (11.95) with $\hat{x}_0 = a$ and $\hat{x}_s(\sigma)$ as in (11.101) (and hence $0 \leq \sigma \leq \sigma_s$), provides the expression of the magnitude F_t of the tangential force

$$F_t = F_t(\sigma) = C_\sigma \sigma \left[1 - \frac{\sigma}{\sigma_s}\left(\frac{1+2\chi}{1+\chi}\right) + \left(\frac{\sigma}{\sigma_s}\right)^2 \left(\frac{1+3\chi}{3(1+\chi)}\right) \right] \tag{11.104}$$

where $\mu_0 = (1+\chi)\mu_1$ as in (11.19). In this model and under these specific operating conditions, $F_t(\sigma)$ is a polynomial function of σ, whose typical behavior is shown in Fig. 11.22, along with its linear approximation ("good" only up to $\sigma \approx 0.03$). From

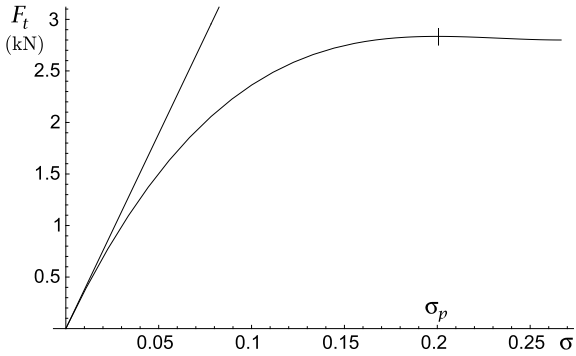

Fig. 11.22 Magnitude F_t of the tangential force as a function of σ, and corresponding linear approximation

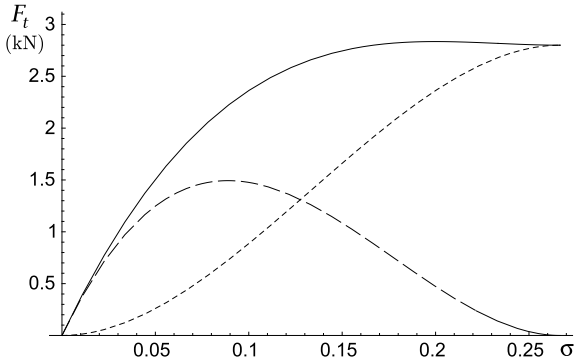

Fig. 11.23 Contributions to F_t (*solid line*) of the adhesion region (*long-dashed line*) and of the sliding region (*short-dashed line*)

Fig. 11.23 we can also appreciate how the adhesion and sliding regions contribute separately to build up the total tangential force.

The derivative of $F_t(\sigma)$ is

$$F_t'(\sigma) = \frac{\mathrm{d}F_t}{\mathrm{d}\sigma} = C_\sigma \left[1 - 2\frac{\sigma}{\sigma_s}\left(\frac{1+2\chi}{1+\chi}\right) + \left(\frac{\sigma}{\sigma_s}\right)^2 \left(\frac{1+3\chi}{1+\chi}\right) \right] \tag{11.105}$$

which, among other things, clearly provides the important result

$$\left.\frac{\mathrm{d}F_t}{\mathrm{d}\sigma}\right|_{\sigma=0} = C_\sigma \tag{11.106}$$

that clarifies why C_σ is called slip stiffness.

As expected, the force with total sliding is

$$F_t(\sigma_s) = \mu_1 F_z \tag{11.107}$$

since all tangential stresses $\mathbf{t}$ have the same direction.

The peak value of F_t is

$$F_t^{\max} = F_t(\sigma_p) = \mu_0 \left[\frac{4 - 3(\mu_1/\mu_0)}{[3 - 2(\mu_1/\mu_0)]^2} \right] F_z = \mu_1 \left[1 + \frac{4\chi^3}{(3\chi + 1)^2} \right] F_z = \mu_p F_z \tag{11.108}$$

and it is achieved at $\sigma = \sigma_p$ (Fig. 11.22)

$$\sigma_p = \frac{1 + \chi}{1 + 3\chi} \sigma_s \tag{11.109}$$

Typically, as in Fig. 11.22, good tires have low values of σ_p. In this model, the global friction coefficient μ_p is given by (cf. (2.90) and (2.92))

$$\mu_p = \frac{F_t^{\max}}{F_z} = \mu_1 \left[1 + \frac{4\chi^3}{(3\chi + 1)^2} \right] \tag{11.110}$$

which means that, as expected

$$\mu_1 < \mu_p \ll \mu_0 \tag{11.111}$$

For instance, if $\mu_0 = 1.2\mu_1$, we have $F_t^{\max} = 0.84\mu_0 F_z = 1.013\mu_1 F_z$, that is a value only marginally higher than $F_t(\sigma_s)$. Indeed, as shown in Fig. 11.26 (and also in Fig. 11.17c), the mechanics of the tire makes it very difficult to have tangential stresses close to $\mu_0 p$. In practical terms, attempts at increasing μ_1 are more worthwhile than those at increasing μ_0.

It may be interesting to fit the curve of $F_t(\sigma)$ shown in Fig. 11.22 by means of the Magic Formula $y(x)$ given in (2.93). According to Sect. 2.12, the four unknown coefficients can be obtained by matching the peak value $y_m = F_t(\sigma_p) = 2.84\,\text{kN}$, the asymptotic value $y_a = F_t(\sigma_s) = 2.80\,\text{kN}$, the slope at the origin $y'(0) = C_\sigma = 37.8\,\text{kN/rad}$ and the abscissa of the peak value $x_m = \sigma_p = 0.2$. The resulting coefficients are $B = 12.1$, $C = 1.10$, $D = 2.835\,\text{kN}$ and $E = -3.63$. The comparison is shown in Fig. 11.24. The agreement between the two curves is quite poor. Par-

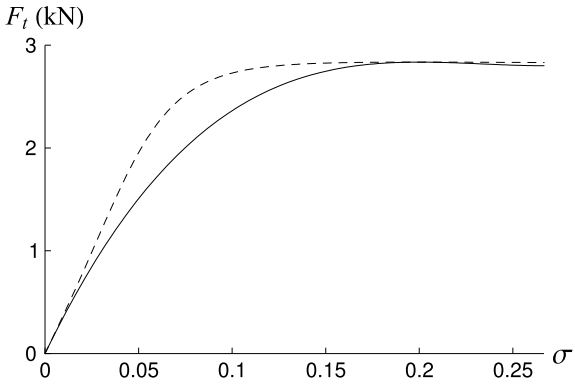

Fig. 11.24 Brush model curve (*solid line*) and the corresponding classical fitting by the Magic Formula (*dashed line*)

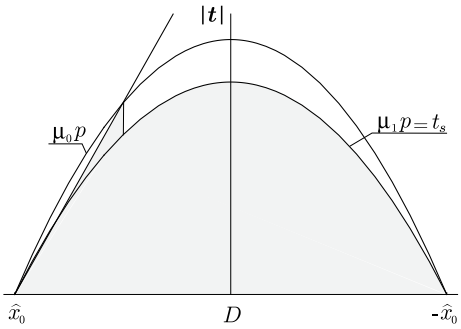

Fig. 11.25 Tangential stress if $\sigma = \sigma_p$ (maximum tangential force). See also Fig. 11.17c

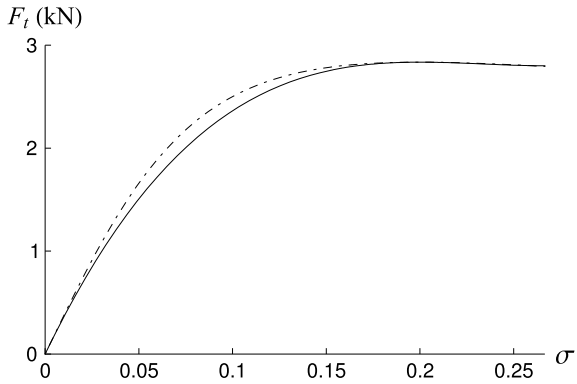

Fig. 11.26 Brush model curve (*solid line*) and another possible fitting by the Magic Formula (*dot-dashed line*)

ticularly unacceptable is the initial increase of the slope, which is never found in experimental curves (cf. Figs. 2.22 and 2.24). Indeed, $E < -(1 + C^2/2)$ and hence $y'''(0) > 0$.

A better agreement is shown in Fig. 11.25, where the asymptotic value was arbitrarily lowered to $y_a = 0.7 F_t(\sigma_s)$, thus obtaining $B = 8.81, C = 1.51, D = 2.84\,\text{kN}$ and $E = 0.1$. The lesson to be learnt is, perhaps, that the Magic Formula may occasionally provide unexpected results and, therefore, should be used with care.

Going back to the brush model, the explicit expressions of $F_x(\sigma_x, \sigma_y)$ and $F_y(\sigma_x, \sigma_y)$, that is of the longitudinal and lateral components, can be obtained by inserting (11.104) into (11.96). Figure 11.27 illustrates the combined effect of σ_x and σ_y. Quite remarkable is the effect on the slope at the origin, that is on the generalized slip stiffness $\widetilde{C}_\sigma$. From (11.98) and (11.104) it follows that

$$\widetilde{C}_\sigma(\sigma_y) = -\left.\frac{\partial F_x}{\partial \sigma_x}\right|_{\sigma_x=0} = C_\sigma \left[1 - \frac{|\sigma_y|}{\sigma_s}\frac{1+2\chi}{1+\chi} + \left(\frac{\sigma_y}{\sigma_s}\right)^2 \frac{1+3\chi}{3(1+\chi)}\right] \tag{11.112}$$

and, interchanging x and y

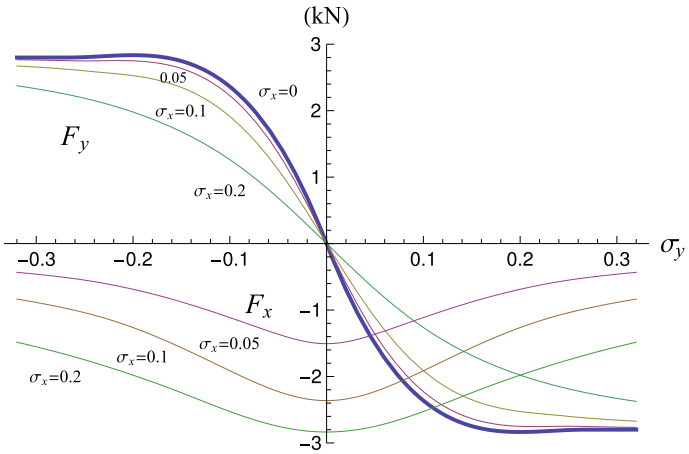

Fig. 11.27 F_y and F_x as functions of σ_y, for $\sigma_x = (0,\ 0.05,\ 0.1,\ 0.2)$

$$\widetilde{C}_\sigma(\sigma_x) = -\left.\frac{\partial F_y}{\partial \sigma_y}\right|_{\sigma_y=0} = C_\sigma \left[1 - \frac{|\sigma_x|}{\sigma_s}\frac{1+2\chi}{1+\chi} + \left(\frac{\sigma_x}{\sigma_s}\right)^2 \frac{1+3\chi}{3(1+\chi)}\right] \tag{11.113}$$

Of course $\widetilde{C}_\sigma(0) = C_\sigma$. This stiffness reduction has strong practical implications on the handling behavior of vehicles. σ_s was defined in (11.102).

It should be observed that the generalized cornering stiffness $\widetilde{C}_\alpha(\sigma_x)$ is no longer equal to $\widetilde{C}_\sigma(\sigma_x)$ (cf. (11.75))

$$\widetilde{C}_\alpha(\sigma_x) = (1+\sigma_x)\widetilde{C}_\sigma(\sigma_x) \tag{11.114}$$

whereas $\widetilde{C}_{\kappa_x}(\sigma_y) = \widetilde{C}_\sigma(\sigma_y)$.

Another useful plot is the one shown in Fig. 11.28. For any combination of (σ_x, σ_y), a point in the plane (F_x, F_y) is obtained such that $\sigma_x/\sigma_y = F_x/F_y$. All these points fall within a circle of radius $F_t^{\max}$, usually called the *friction circle*. Lines with constant σ_y are also drawn in Fig. 11.28. Because of the symmetry of this tire model, lines with constant σ_x are identical, but rotated of 90 degrees around the origin, as shown in Fig. 11.37b.

More often, the plot employed is the one in Fig. 11.29, where lines with constant slip angle α are drawn. Since α is a function of σ_x *and* σ_y (Eq. (2.81)), the two plots contain exactly the same information. While the lines in Fig. 11.28 are symmetric with respect to the vertical axis, lines in Fig. 11.29 are not, as shown in Fig. 11.30. The asymmetry arises simply because the slip angle is not the parameter to be used for a neat description of the tire mechanics. Indeed, as schematically shown in Fig. 11.31, the bristles may have different lateral deformations under the same slip angle.

As already mentioned on p. 37, tires have to be built in such a way to provide the maximum tangential force $\mathbf{F}_t$ *in any direction* with small slip angles α, as shown in

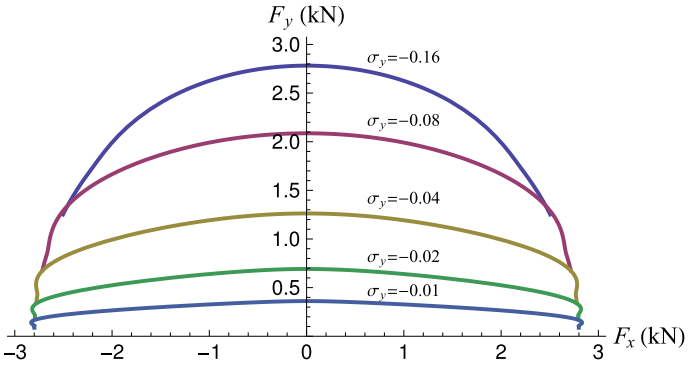

Fig. 11.28 Friction circle with lines at constant σ_y

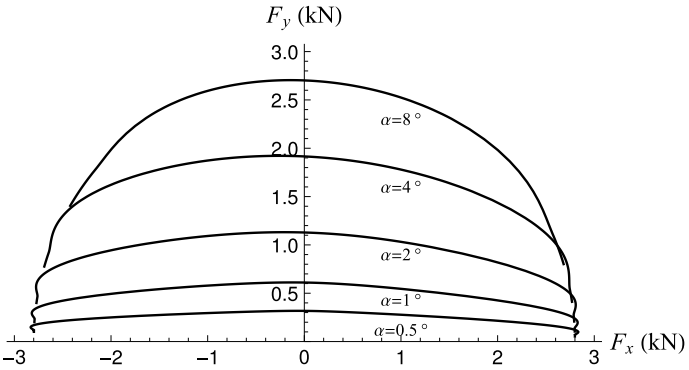

Fig. 11.29 Friction circle of Fig. 11.28, but with lines at constant α

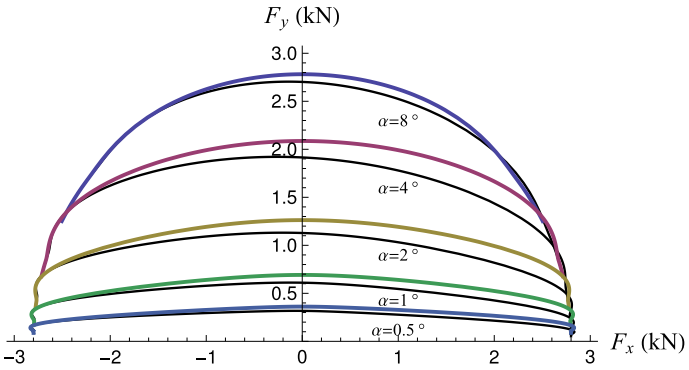

Fig. 11.30 Comparison

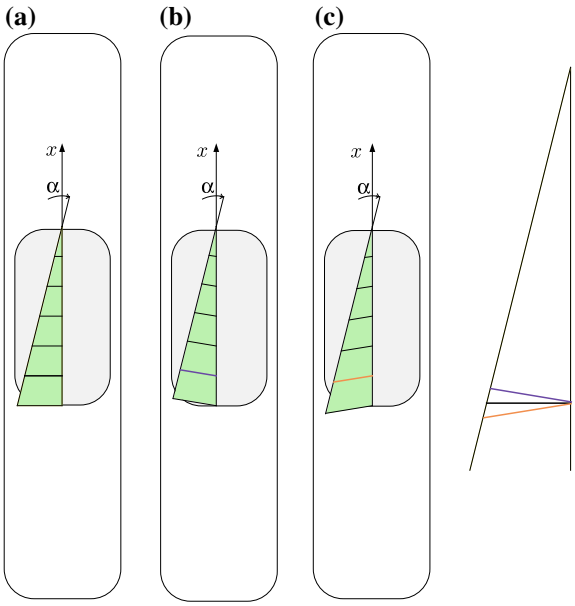

Fig. 11.31 Same slip angle α, but different σ_y if: **a** $\sigma_x = 0$, **b** $\sigma_x < 0$ (driving), **c** $\sigma_x > 0$ (braking)

Fig. 11.32. This is a fundamental requirement for a wheel with tire to behave almost like a wheel, that is to have a *directional capability*. In other words, while $\mathbf{F}_t$ can have any direction, the travel velocity $\mathbf{V}_c$ must undergo just small deviations α. According to (2.81), this condition will be fulfilled if and only if the tire exhibits the peak value of $\mathbf{F}_t$ for small values of the theoretical slip σ_p, typically below 0.2. On the contrary, in a locked wheel the two vectors $\mathbf{F}_t$ and $\mathbf{V}_c$ always point in opposite directions.

Equation (11.99), with $\hat{x}_0 = a$ and $\hat{x}_s$ as in (11.101), provides the vertical moment M_z^D with respect to the center D of the rectangular contact patch

$$M_z^D(\sigma_x, \sigma_y) = \sigma_y C_\sigma \frac{a}{3}\left[1 - 3\frac{\sigma}{\sigma_s}\frac{1+2\chi}{1+\chi} + 3\left(\frac{\sigma}{\sigma_s}\right)^2 \frac{1+3\chi}{1+\chi} - \left(\frac{\sigma}{\sigma_s}\right)^3 \frac{1+4\chi}{1+\chi}\right]$$
$$= \frac{\sigma_y}{\sigma} F_t(\sigma) t_c(\sigma) = -F_y(\sigma_x, \sigma_y) t_c(\sigma) \tag{11.115}$$

where t_c is the pneumatic trail. The typical behavior of M_z^D is shown in Fig. 11.33.

However, under combined slip conditions, to obtain M_z with respect to point O it is necessary to take into account the *carcass compliance*, according to (11.72). The typical behavior of $M_z(\sigma_x, \sigma_y)$ is shown in Fig. 11.34. The difference with Fig. 11.33 is quite relevant.

Also of practical interest may be the plots of M_z versus F_x (Fig. 11.35) and of F_y versus $-M_z$ (Fig. 11.36), this one being often called *Gough plot* if $\sigma_x = 0$.

The three functions $F_x(\sigma_x, \sigma_y)$, $F_y(\sigma_x, \sigma_y)$ and $M_z(\sigma_x, \sigma_y)$ can be seen as the parametric equations of a three-dimensional surface that fully describes, at constant

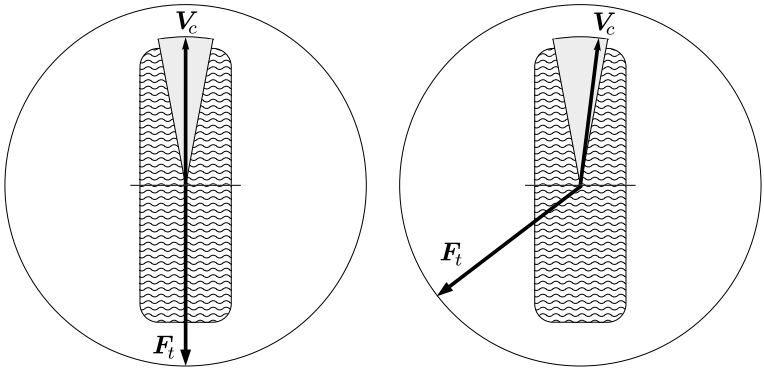

(a) $\sigma_x = \sigma_p$ and $\sigma_y = \mathbf{0}$ (b) $\sigma_x > 0$ and $\sigma_y < 0$

(c) $\sigma_x = 0$ and $\sigma_y = -\sigma_p$ (d) $\sigma_x < 0$ and $\sigma_y < 0$

Fig. 11.32 Typical relationships between the tangential force $\mathbf{F}_t$ and the travel velocity $\mathbf{V}_c$ for a tire with the same theoretical slip $\sigma = \sqrt{\sigma_x^2 + \sigma_y^2} = \sigma_p$, but different σ_x/σ_y

vertical load F_z, the tire mechanical behavior. Such surface is shown in Fig. 11.37a, along with its three projections, which are precisely like Figs. 11.27, 11.35 and 11.36, respectively. The surface in Fig. 11.37a is called here the *tire action surface*.

As already mentioned, a wheel with tire can be called a wheel because:

1. the tire action surface is regular, in the sense that it does not fold onto itself, for a limited set of values (σ_x, σ_y). It has therefore a limited contour and, hence, the slip angle α is always quite low, according to (2.81). The goal of ABS [10] is to avoid wheel locking and also to keep $|\alpha|$ very low, thus maintaining the *directional capability* of the wheels;
2. the vertical moment M_z is always moderate. A wheel must provide forces applied not far from the center of the contact patch.

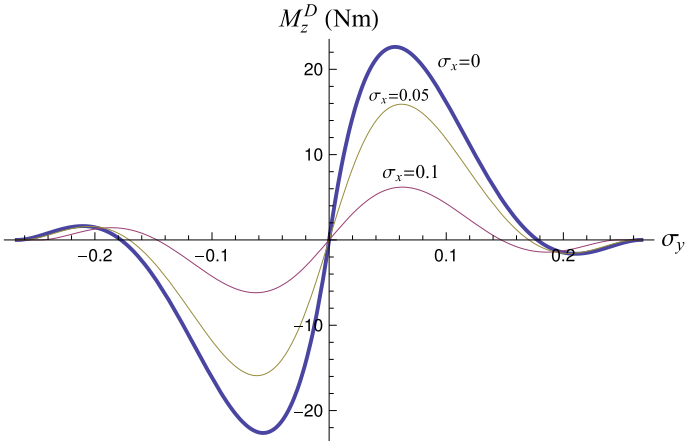

Fig. 11.33 Vertical moment M_z^D versus σ_y, at constant σ_x

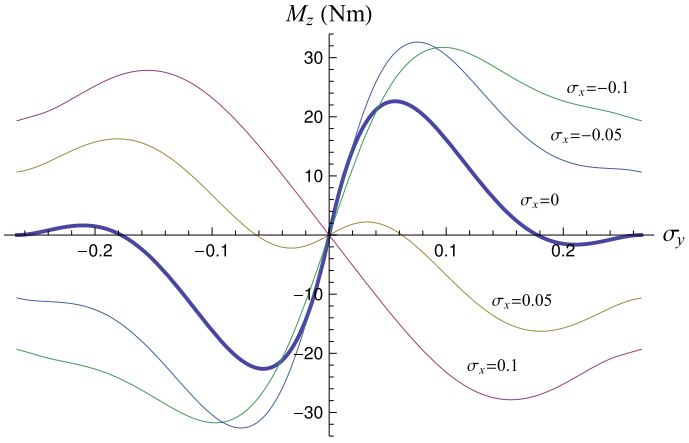

Fig. 11.34 Vertical moment M_z versus σ_y, at constant σ_x and $\gamma = 0$

11.5.2 Elliptical Contact Patch

Assuming an elliptical shape (Fig. 11.3) essentially means setting $\hat{x}_0(\hat{y})$ according to (11.2). As shown in Figs. 11.15 and 11.19, in this case the line between the adhesion and the sliding regions is *curved*. Its explicit equation is obtained inserting (11.2) into (11.91). To have sliding on the whole elliptical contact patch, a very high value of σ is necessary (Fig. 11.15).

Application of (11.95) with suitable $\hat{x}_0(\hat{y})$ and $\hat{x}_s(\sigma, \hat{y})$ provides the expression of the magnitude F_t of the tangential force

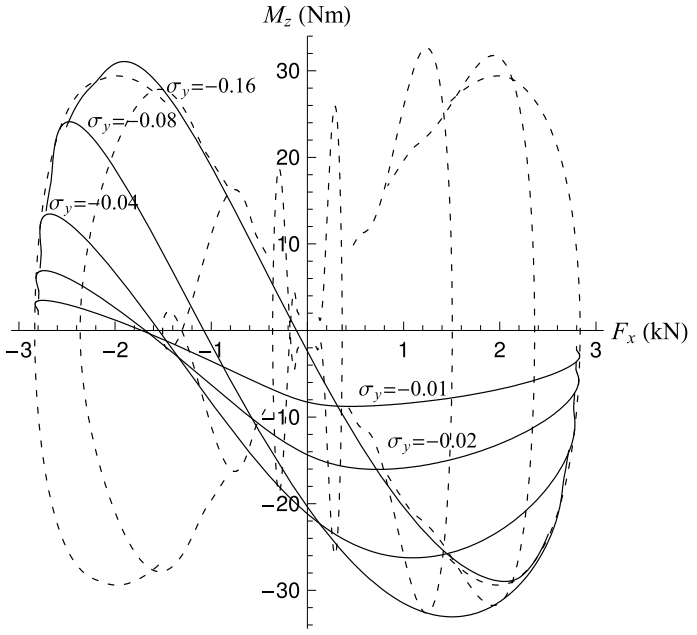

Fig. 11.35 Vertical moment M_z versus longitudinal force F_x, with lines at constant σ_y (*solid*) and constant σ_x (*dashed*: ± 0.01, ± 0.05, ± 0.1, ± 0.2)

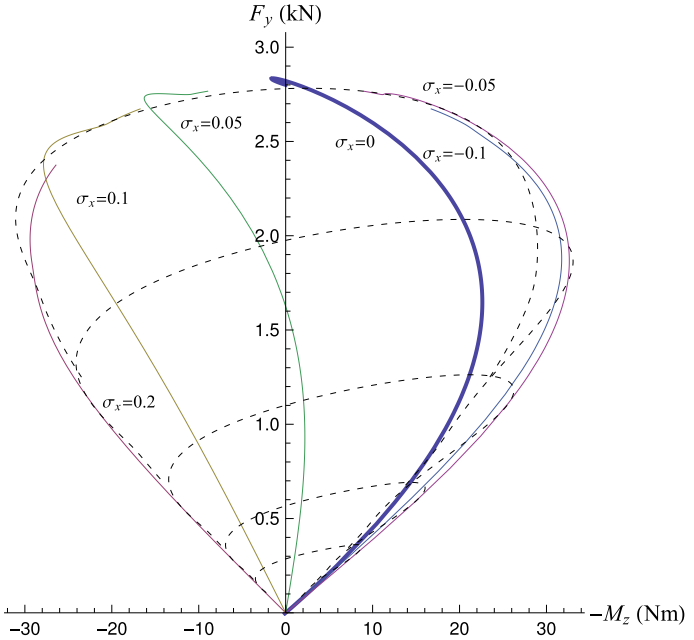

Fig. 11.36 Lateral force F_y versus vertical moment M_z, with lines at constant σ_x (*solid*) and constant σ_y (*dashed*: -0.01, -0.02, -0.04, -0.08, -0.16)

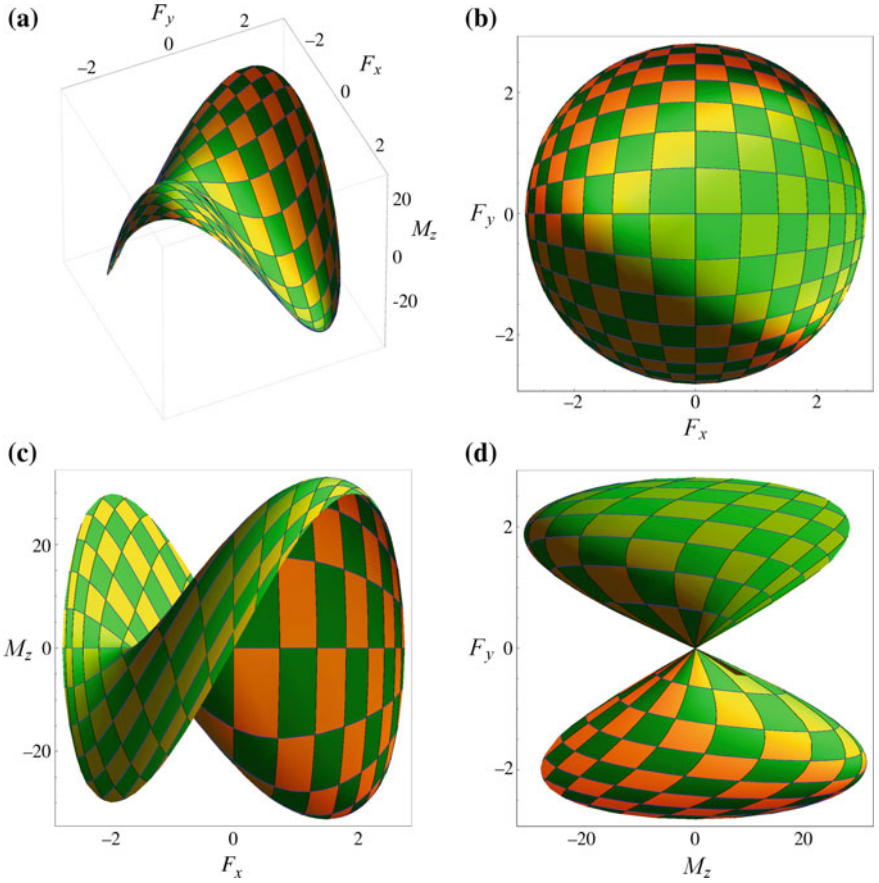

Fig. 11.37 *Tire action surface*, and its three projections (forces in kN and moments in Nm). Also shown lines at constant σ_x (blue) and constant σ_y (black)

$$F_t = F_t(\sigma) = C_\sigma \sigma \left[1 - \frac{18\pi}{64} \frac{\sigma}{\sigma_s} \left(\frac{1+2\chi}{1+\chi} \right) + \frac{12}{45} \left(\frac{\sigma}{\sigma_s} \right)^2 \left(\frac{1+3\chi}{1+\chi} \right) \right] \tag{11.116}$$

where C_σ was obtained in (11.86) and σ_s is as in (11.102), although it has no special meaning in this case. Again, $F_t(\sigma)$ is a polynomial function of σ, whose typical behavior is much like in Fig. 11.22, but with a less evident peak.

11.6 Wheel with Pure Spin Slip ($\sigma = 0, \varphi \neq 0$)

The investigation of the behavior of the brush model becomes much more involved if there is *spin slip* φ. Even if $\boldsymbol{\sigma} = \mathbf{0}$, the problem in the sliding region has to be solved in full generality according to the governing equations (11.60). Therefore, numerical solutions have to be sought.

The definition of φ was given in (2.68) and is repeated here

$$\varphi = -\frac{\omega_z + \omega_c \sin\gamma\,(1 - \varepsilon_r)}{\omega_c\, r_r} \tag{2.68'}$$

It involves ω_z, $\sin\gamma$, ε_r, ω_c and r_r. However, in most applications spin slip means camber angle γ, since $\omega_z/\omega_c \approx 0$. Figure 11.38 reports an example of the relationship between γ and φ, if $\varepsilon_r = 0$ (motorcycle tire), $r_r = 0.25\,\text{m}$ and $\omega_z = 0$.

Large values of φ are attained only in motorcycles.[12] Therefore, in this section the analysis is restricted to *elliptical* contact patches. Figure 11.39 shows the almost linear growth of the (normalized) lateral force $F_y^n(\mathbf{0}, \varphi) = F_y^n(\varphi) = F_y/F_z$, even for very large values of the spin slip. A similar pattern can be observed in Fig. 11.40 for the vertical moment $M_z^D = M_z$. In both cases, the main contribution comes from the adhesion regions.

The lateral force plotted in Fig. 11.39 is precisely what is usually called the *camber force*, that is the force exerted by the road on a tire under pure spin slip.

Some examples of tangential stress distributions are shown in Fig. 11.41. They are quite informative. There is adhesion along the entire central line, and the stress has a parabolic pattern. The value of φ does not affect the direction of the arrows in the adhesion region, but only their magnitude. Even at $\varphi = 3.33\,\text{m}^{-1}$, i.e. a very high value, the two symmetric sliding regions have spread only on less than half the contact patch.

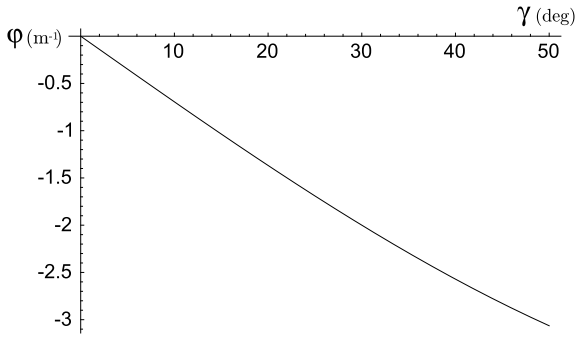

Fig. 11.38 Relationship between the camber angle γ and the spin slip φ, if $\omega_z = 0$, $\varepsilon_r = 0$, and $r_r = 0.25\,\text{m}$

[12] More generally, in tilting vehicles, which may have three wheels, like *MP3* by *Piaggio*, or even four.

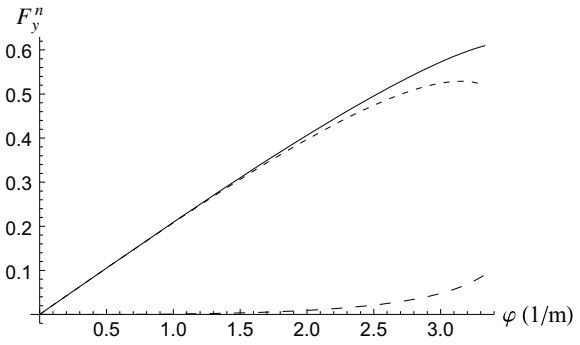

Fig. 11.39 Normalized lateral force versus spin slip (*solid line*). Also shown is the contribution of the adhesion zone (*short-dashed line*) and of the sliding zone (*long-dashed line*)

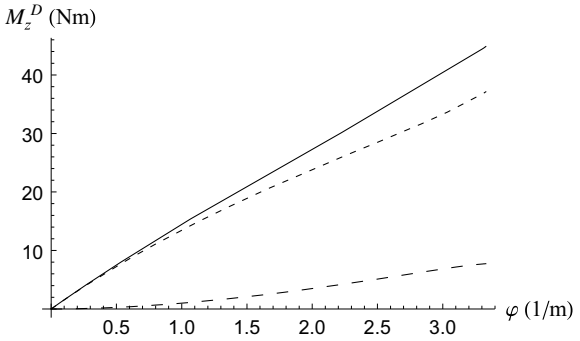

Fig. 11.40 Vertical moment versus spin slip (*solid line*). Also shown is the contribution of the adhesion zone (*short-dashed line*) and of the sliding zone (*long-dashed line*)

Another important observation is that there are longitudinal components of the tangential stress, although the longitudinal force $F_x = 0$. In some sense, these components are wasted, and keeping them as low as possible is a goal in the design of real tires.

The comparison of Figs. 11.41d and 11.42 gives an idea of the effect of the shape of the contact patch. In the second case the lengths of the axes have been inverted, while all other parameters are unchanged. Nevertheless, the normalized lateral force is much lower (0.36 vs 0.61).

In the brush model developed here, the lateral force and the vertical moment depend on φ, but not directly on γ. Therefore, there is no distinction between operating conditions with the same spin slip φ, but different camber angle γ as in Fig. 2.21. This is a limitation of the model with respect to what stated on p. 39.

It should be appreciated that a cambered wheel under pure spin slip cannot be in free rolling conditions. According to (2.12), there must be a torque $\mathbf{T} = M_z \sin\gamma\, \mathbf{j}_c = T\, \mathbf{j}_c$ with respect to the wheel axis. Conversely, $T = 0$ requires a longitudinal force F_x and hence a longitudinal slip σ_x.

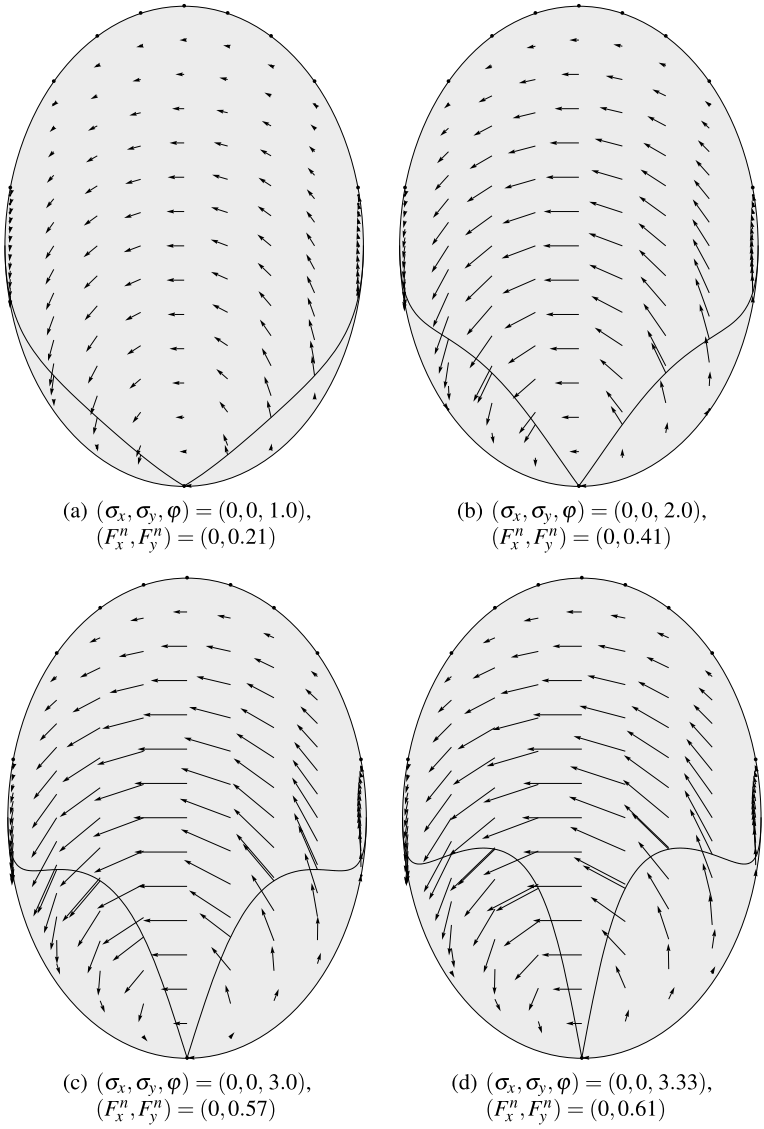

(a) $(\sigma_x, \sigma_y, \varphi) = (0, 0, 1.0)$, $(F_x^n, F_y^n) = (0, 0.21)$

(b) $(\sigma_x, \sigma_y, \varphi) = (0, 0, 2.0)$, $(F_x^n, F_y^n) = (0, 0.41)$

(c) $(\sigma_x, \sigma_y, \varphi) = (0, 0, 3.0)$, $(F_x^n, F_y^n) = (0, 0.57)$

(d) $(\sigma_x, \sigma_y, \varphi) = (0, 0, 3.33)$, $(F_x^n, F_y^n) = (0, 0.61)$

Fig. 11.41 Examples of tangential stress distributions in elliptical contact patches under *pure spin slip* φ. Also shown is the line separating the adhesion region (top) and the two sliding regions (bottom). Values of φ are in m^{-1}

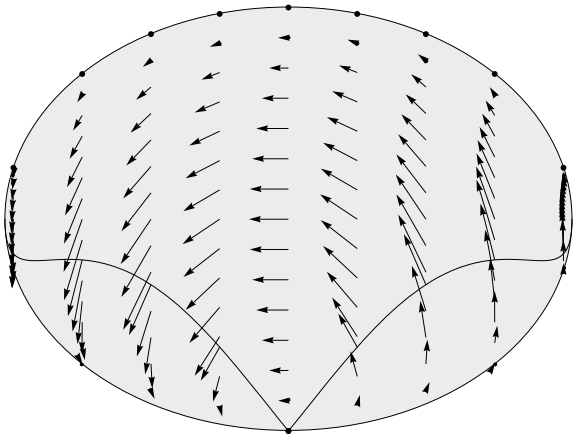

Fig. 11.42 Elliptical contact patch with inverted proportions. $(\sigma_x, \sigma_y, \varphi) = (0, 0, 3.33)$, $(F_x^n, F_y^n) = (0, 0.36)$

11.7 Wheel with Both Translational and Spin Slips

From the tire point of view, there are fundamentally two kinds of vehicles: cars, trucks and the like, whose tires may operate at relatively large values of translational slip and small values of spin slip, and motorcycles, bicycles and other tilting vehicles, whose tires typically operate with high camber angles and small translational slips. In both cases, the interaction between $\boldsymbol{\sigma}$ and φ in the mechanics of force generation is of great practical relevance. The tuning of a vehicle often relies on the right balance between these kinematical quantities.

11.7.1 Rectangular Contact Patch

Rectangular contact patches mimic those of car tires. Therefore, we will address the effect of just a bit of spin slip on the lateral force of a wheel mainly subjected to lateral slips. The goal is to achieve the highest possible value of F_y^n. Unfortunately, it is not possible to obtain analytical results and a numerical approach has to be pursued.

A rectangular contact patch under pure spin slip (arrows magnified by a factor 5) is shown in Fig. 11.43. The global effect is a small lateral force, usually called camber force.

Indeed, as shown in Fig. 11.44, the effect of a small amount of spin slip φ is, basically, to translate *horizontally* the curve of the lateral force versus σ_y.[13] However, the peak value is also affected, as more clearly shown in Fig. 11.45. By means of a trial-and-error procedure it has been found, in the case at hand, that $\varphi = 0.21\ \mathrm{m}^{-1}$ does indeed provide the highest positive value of F_y^n. In general, car tires need just a

[13] Of course, the effect cannot be to "add" the camber force, that is to translate the curve vertically.

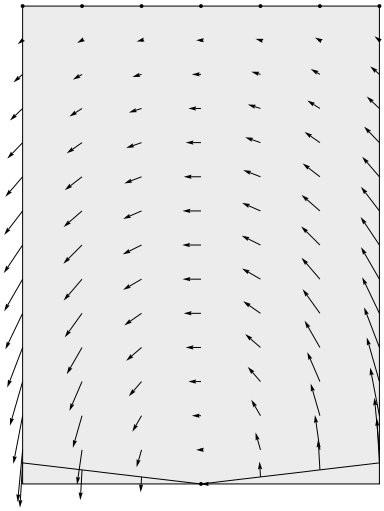

Fig. 11.43 Rectangular contact patch under pure spin slip (arrows magnified by a factor 5 with respect to the other figures). $(\sigma_x, \sigma_y, \varphi) = (0, 0, 0.21)$, $(F_x^n, F_y^n) = (0, 0.06)$

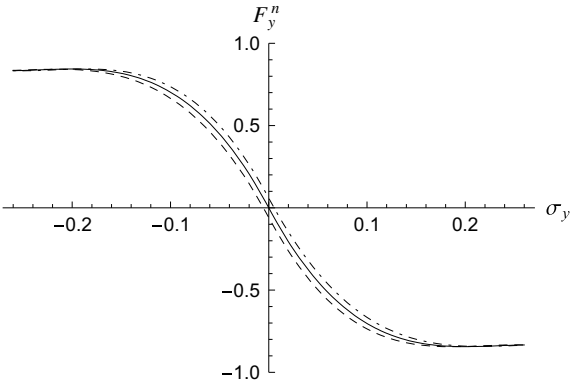

Fig. 11.44 Normalized lateral force F_y^n versus σ_y, for $\varphi = 0$ (*solid line*), $\varphi = -0.21\,\mathrm{m}^{-1}$ (*dashed line*), $\varphi = 0.21\,\mathrm{m}^{-1}$ (*dot-dashed line*). Rectangular contact patch and $\sigma_x = 0$ in all cases

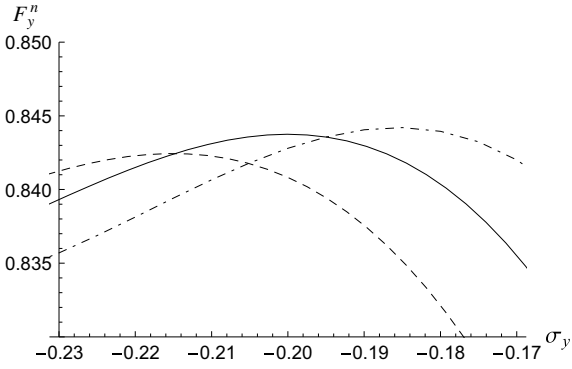

Fig. 11.45 Detail of Fig. 11.44 showing different peak values

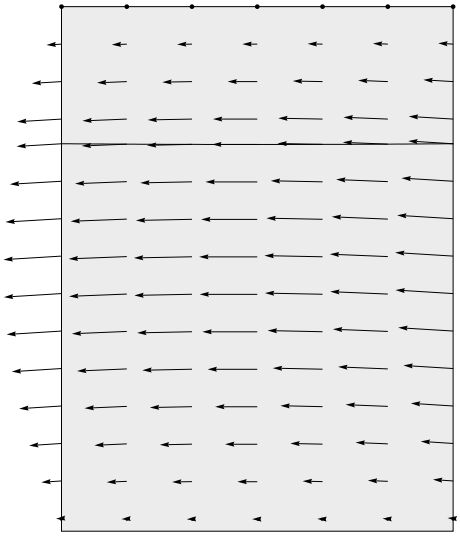

Fig. 11.46 Rectangular contact patch under lateral and spin slips. $(\sigma_x, \sigma_y, \varphi) = (0, -0.185, 0.21)$, $(F_x^n, F_y^n) = (0, 0.84)$

few degrees of camber to provide the highest lateral force as a function of the lateral slip σ_y (Fig. 11.46).

Such small values of spin slip have very little influence on the longitudinal force generation.

11.7.2 Elliptical Contact Patch

Elliptical contact patches mimic those of motorcycle tires. Therefore, in this case we will study the effect of just a bit of lateral slip σ_y on the lateral force of a cambered wheel. Again, the goal is to achieve the highest possible value of F_y^n.

The large effect of even a small amount of σ_y on the normalized lateral force F_y^n as a function of φ is shown in Fig. 11.47. However, this is quite an expected result after (11.86). Consistently, also the vertical moment M_z^D changes a lot under the influence of small variations of σ_y (Fig. 11.48).

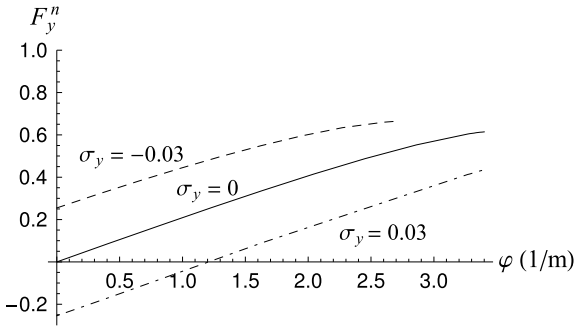

Fig. 11.47 Elliptical contact patch: normalized lateral force versus spin slip, at different values of lateral slip

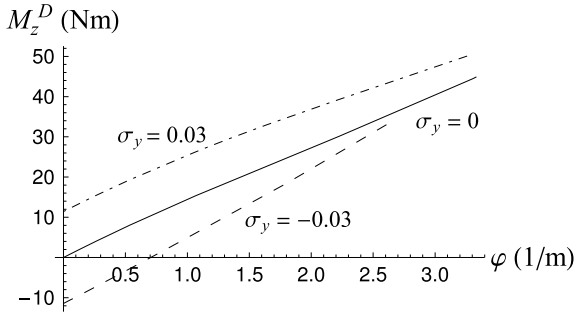

Fig. 11.48 Elliptical contact patch: vertical moment versus spin slip, at different values of lateral slip

Figures 11.49 and 11.50 provide a pictorial representation of the tangential stress in two relevant cases, that is those that yield the highest lateral force. Quite remarkably, a 10% higher value of F_y^n is achieved in case (b) with respect to case (a). In general, a little σ_y has a great influence on the stress distribution in the contact patch. Conversely, the same lateral force can be obtained by infinitely many combinations (σ_y, φ). This is something most riders know intuitively. Obviously, $F_x = 0$ in all cases of Figs. 11.49 and 11.50.

Under these operating conditions, according to (2.81), the slip angle α never exceeds two degrees. Therefore, the wheel has excellent directional capability.

It should be observed that the larger value of F_y^n of case (b) in Fig. 11.49 is associated with a smaller value of M_z^D. Basically, it means that the tangential stress distribution in the contact patch is *better organized* to yield the lateral force, without wasting much in the vertical moment (mainly due to useless longitudinal stress components). The comparison shown in Fig. 11.49c confirms this conclusion.

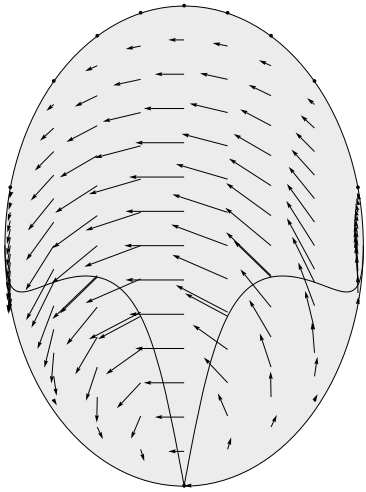

(a) $(\sigma_x, \sigma_y, \varphi) = (0, 0, 3.33)$, $F_y^n = 0.61$, $M_z^D = 44.9$ Nm

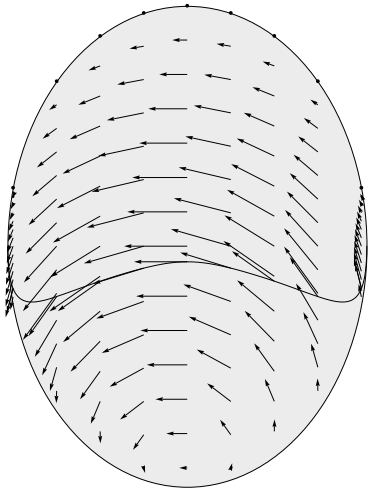

(b) $(\sigma_x, \sigma_y, \varphi) = (0, -0.03, 2.7)$, $F_y^n = 0.66$, $M_z^D = 34.7$ Nm

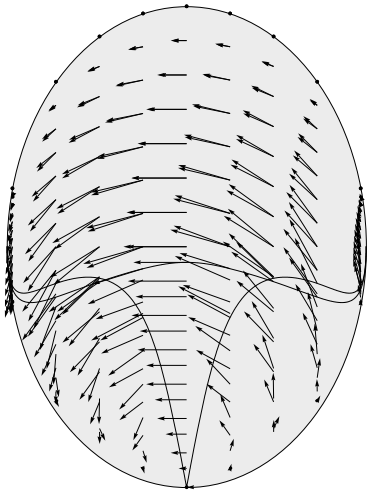

(c) Comparison of (a) and (b)

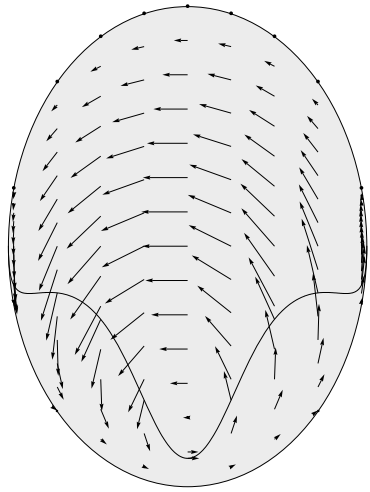

(d) $(\sigma_x, \sigma_y, \varphi) = (0, 0.03, 3.33)$, $F_y^n = 0.42$, $M_z^D = 50.4$ Nm

Fig. 11.49 Comparison between contact patches under **a** large spin slip only and **b** still quite large spin slip with the addition of a little of lateral slip. Case **d** shown for completeness. Values of φ are in m^{-1}

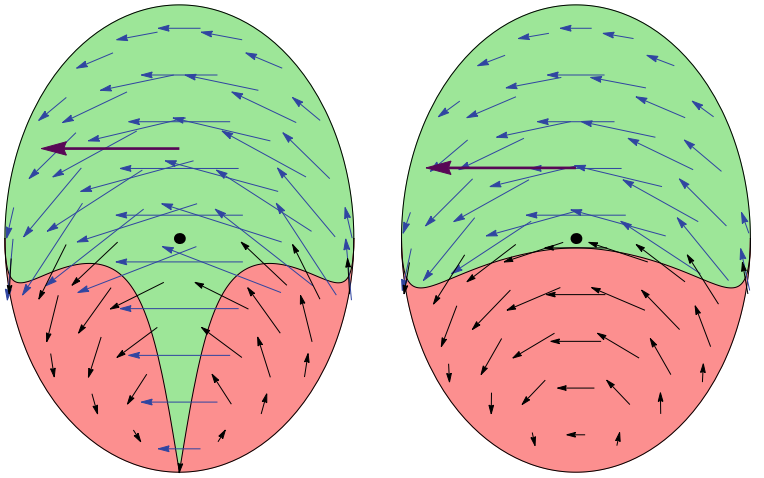

(a) $(\sigma_x, \sigma_y, \varphi) = (0, 0, 3.33)$, $F_y^n = 0.61$ (b) $(\sigma_x, \sigma_y, \varphi) = (0, -0.02, 3)$, $F_y^n = 0.65$

Fig. 11.50 Normalized lateral force in elliptical contact patches under **a** large spin slip only and **b** still quite large spin slip with the addition of a little of lateral slip

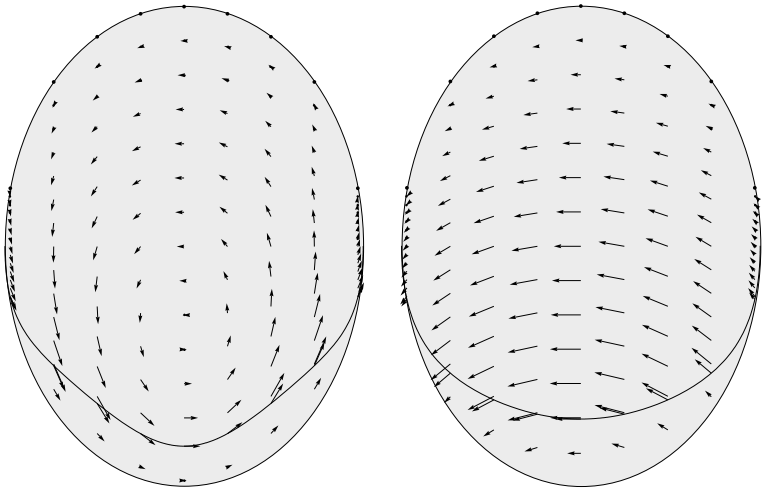

(a) $(\sigma_x, \sigma_y, \varphi) = (0, 0.03, 1.21)$, $F_y^n = 0$, $M_z^D = 28.0\,\mathrm{Nm}$

(b) $(\sigma_x, \sigma_y, \varphi) = (0, -0.03, 0.70)$, $F_y^n = 0.39$, $M_z^D = 0$

Fig. 11.51 Special cases: **a** zero lateral force and **b** zero vertical moment

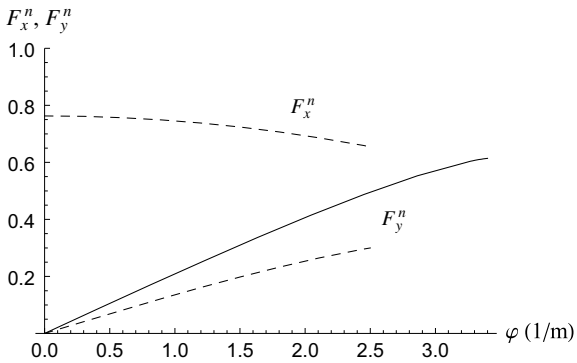

Fig. 11.52 Elliptical contact patch: normalized longitudinal and lateral forces versus spin slip, at $\sigma_x = 0$ (*solid line*) and $\sigma_x = -0.15$ (*dashed lines*)

A lateral slip in the "wrong" direction, like in Fig. 11.49d, yields a reduction of the lateral force and an increase of the vertical moment.

As reported in Figs. 11.47 and 11.48, there are particular combinations of (σ_y, φ) which provide either $F_y^n = 0$ or $M_z^D = 0$. The stress distributions in such two cases are shown in Fig. 11.51.

The interaction of longitudinal slip σ_x and spin slip φ yields the effects reported in Fig. 11.52 on the longitudinal and lateral forces. A fairly high value $\sigma_x = -0.15$ has been employed. Examples of stress distributions are given in Fig. 11.53.

11.8 Brush Model Transient Behavior

Understanding and describing the transient behavior of wheels with tires has become increasingly important with the advent of electronic systems like ABS [10] or traction control, which may impose very rapidly varying slip conditions (up to tens of cycles per second).

Addressing the problem in its full generality like in Sect. 11.2, even in the simple brush model, looks prohibitive ¡8but not impossible to good will researchers). However, with the aid of some additional simplifying assumptions, some interesting results can be achieved which, at least, give some hints on what is going on when a tire is under transient operating conditions.

In the next Sections some simplified transient models will be developed. In all cases, inertia effects are totally neglected.

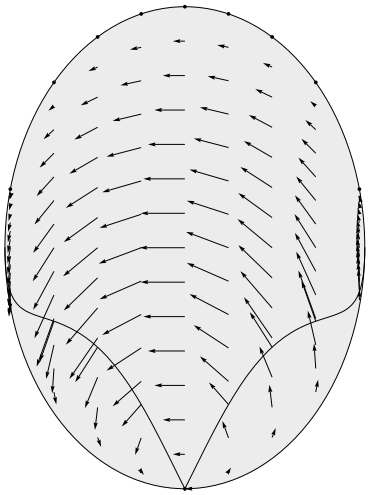

(a) $(\sigma_x, \sigma_y, \varphi) = (0, 0, 2.5)$,
$(F_x^n, F_y^n) = (0, 0.50)$

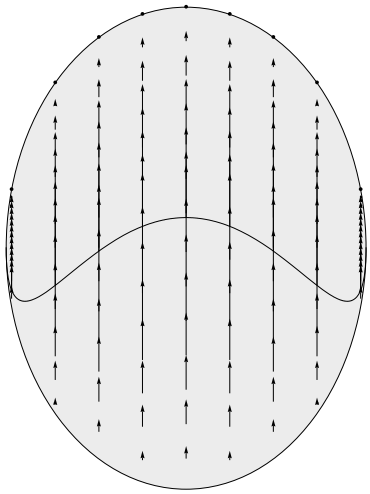

(b) $(\sigma_x, \sigma_y, \varphi) = (-0.15, 0, 0)$,
$(F_x^n, F_y^n) = (0.76, 0)$

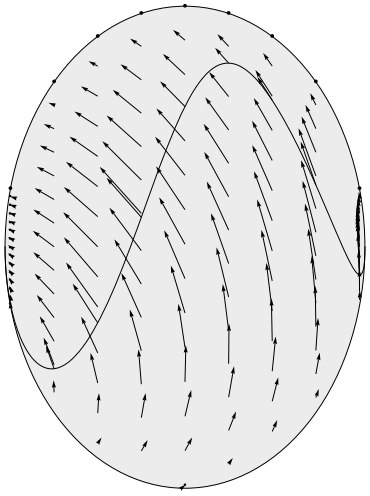

(c) $(\sigma_x, \sigma_y, \varphi) = (-0.15, 0, 2.5)$,
$(F_x^n, F_y^n) = (0.65, 0.30)$

Fig. 11.53 Examples of tangential stress distributions: **a** pure spin slip φ, **b** pure longitudinal slip σ_x and **c** both φ and σ_x. Values of φ are in m^{-1}

11.8.1 Transient Models with Carcass Compliance Only

A possible way to partly generalize the steady-state brush model discussed in Sect. 11.3 is to relax only the second condition of p. 478, while still retaining the first one, that is:

- $\mathbf{e}_{,t} = \mathbf{0}$, which means $\mathbf{e} = \mathbf{e}(\hat{x}, \hat{y})$, with no time dependence;
- $\dot{\mathbf{q}} \neq \mathbf{0}$, which means that $\boldsymbol{\rho}(t) \neq \boldsymbol{\sigma}$(t).

This approach, which leads to some simple and very popular transient tire models, discards the transition in the bristle deflection pattern $\mathbf{e}$ and takes care only of the transient deformation $\mathbf{q}(t)$ of the carcass.

This kind of models are often referred to as *single contact point* transient tire models [8]. Actually, the contact is not at one point. More precisely, it is assumed that all points of the contact patch have the same motion, as in Fig. 11.7.

Although rarely stated explicitly, these models can be safely employed whenever the carcass stiffnesses w_x and/or w_y are much lower than the total tread stiffness k_t

$$w_i \ll k_t, \qquad i = x, y \tag{11.117}$$

Indeed, owing to (11.44), this condition allows for $\dot{\mathbf{F}}_t \neq \mathbf{0}$ even if $\mathbf{e}_{,t} \approx \mathbf{0}$. The physical interpretation of these inequalities is that the transient phenomenon in the contact patch is much faster than that of the carcass.

In a rectangular contact patch $2a \times 2b$, the total tread stiffness k_t is related to the local tread stiffness k by this very simple formula

$$k_t = 4abk \tag{11.118}$$

For instance, with the data reported on p. 477, we have $w_x = k_t$ and $w_y = 0.25k_t$. Therefore, we see that (11.117) in *not fulfilled* in the longitudinal direction!

In these models, the transient translational slip

$$\boldsymbol{\rho}(t) = \boldsymbol{\sigma}(t) + \dot{\mathbf{q}}(t)/V_r(t) \tag{11.119}$$

is an unknown function, like $\mathbf{q}(t)$, while $\boldsymbol{\sigma}(t)$ is, as usual, an input function, along with $\varphi(t)$ and $V_r(t)$.

11.8.1.1 Transient Nonlinear Tire Model

The general governing equations (11.39) and (11.40), with the assumption $\mathbf{e}_{,t} = \mathbf{0}$, become

$$\mathbf{e}' - \boldsymbol{\varepsilon} = \mathbf{0} \qquad \Longleftrightarrow \qquad k|\mathbf{e}| < \mu_0\, p \qquad \text{(adhesion)} \tag{11.120}$$

$$k\mathbf{e} = -\mu_1 p\, \frac{\mathbf{e}' - \boldsymbol{\varepsilon}}{|\mathbf{e}' - \boldsymbol{\varepsilon}|} \qquad \Longleftrightarrow \qquad |\mathbf{e}' - \boldsymbol{\varepsilon}| > 0 \qquad \text{(sliding)} \tag{11.121}$$

where $\boldsymbol{\varepsilon} = \boldsymbol{\rho} - (\hat{x}\,\mathbf{j} - \hat{y}\,\mathbf{i})\varphi$ and $\mathbf{e}' = \mathbf{e}_{,\hat{x}}$.

These equations are *formally identical* to the governing equations (11.53) and (11.54) of the steady-state case. Both cases share the assumption $\mathbf{e}_{,t} = \mathbf{0}$. Therefore, the whole analysis developed in Sect. 11.3 holds true in this case as well, with the important difference that $\boldsymbol{\rho} = \boldsymbol{\sigma} + \dot{\mathbf{q}}/V_r(t)$ has to replace any occurrence of $\boldsymbol{\sigma}$, since now $\dot{\mathbf{q}} \neq 0$.

Of particular importance is to understand that the global tangential force $\mathbf{F}_t = \mathbf{F}_t(\boldsymbol{\rho}, \varphi)$ is exactly the *same function* of (11.69). For instance, in a *rectangular* contact patch with $\varphi = 0$ the magnitude of $\mathbf{F}_t$ is given by a formula identical to (11.104), that is

$$F_t = F_t(\rho(t)) = C_\sigma \rho \left[1 - \frac{\rho}{\sigma_s} \left(\frac{1+2\chi}{1+\chi} \right) + \left(\frac{\rho}{\sigma_s} \right)^2 \left(\frac{1+3\chi}{3(1+\chi)} \right) \right] \tag{11.122}$$

with $\rho = |\boldsymbol{\rho}|$.

Consequently, the components $F_x(\rho_x, \rho_y)$ and $F_y(\rho_x, \rho_y)$ of F_t are

$$F_x = -\frac{\rho_x}{\rho} F_t(\rho), \qquad F_y = -\frac{\rho_y}{\rho} F_t(\rho) \tag{11.123}$$

Of course, $\boldsymbol{\rho} = \rho_x\,\mathbf{i} + \rho_y\,\mathbf{j}$. The partial derivatives are given by (11.98), again with $\boldsymbol{\rho}$ replacing $\boldsymbol{\sigma}$.

Since $\boldsymbol{\rho}(t) = \boldsymbol{\sigma}(t) + \dot{\mathbf{q}}(t)/V_r(t)$, the transient slip $\boldsymbol{\rho}(t)$ is an unknown function and an additional vectorial equation is necessary (it was not so in the steady-state case, which had $\dot{\mathbf{q}} = \mathbf{0}$). The key step to obtain the missing equation is getting $\dot{\mathbf{F}}_t$ and inserting it into (11.43), as already done in Sect. 11.2 for the general case.

The simplification with respect to the transient general case, as already stated, is that here $\mathbf{F}_t(\boldsymbol{\rho}, \varphi)$ is a *known* function and hence

$$\begin{cases} \dot{F}_x = \dfrac{\partial F_x}{\partial \rho_x}\dot{\rho}_x + \dfrac{\partial F_x}{\partial \rho_y}\dot{\rho}_y + \dfrac{\partial F_x}{\partial \varphi}\dot{\varphi} = w_x V_r(\rho_x - \sigma_x) \\ \dot{F}_y = \dfrac{\partial F_y}{\partial \rho_x}\dot{\rho}_x + \dfrac{\partial F_y}{\partial \rho_y}\dot{\rho}_y + \dfrac{\partial F_y}{\partial \varphi}\dot{\varphi} = w_y V_r(\rho_y - \sigma_y) \end{cases} \tag{11.124}$$

is a system of linear differential equations with nonconstant coefficients in the unknown functions $\rho_x(t)$ and $\rho_y(t)$. In general, it requires a numerical solution. The influence of the spin slip rate $\dot{\varphi}$ is negligible and will be discarded from here onwards.

Generalized relaxation lengths can be defined in (11.124)

$$\begin{aligned} s_{xx}(\rho_x, \rho_y) &= -\frac{\partial F_x}{\partial \rho_x}\frac{1}{w_x}, \qquad s_{xy}(\rho_x, \rho_y) = -\frac{\partial F_x}{\partial \rho_y}\frac{1}{w_x} \\ s_{yx}(\rho_x, \rho_y) &= -\frac{\partial F_y}{\partial \rho_x}\frac{1}{w_y}, \qquad s_{yy}(\rho_x, \rho_y) = -\frac{\partial F_y}{\partial \rho_y}\frac{1}{w_y} \end{aligned} \tag{11.125}$$

where the minus sign is there to have positive lengths. System (11.124) can be rewritten as

$$\begin{cases} -s_{xx}\dot{\rho}_x - s_{xy}\dot{\rho}_y = V_r(\rho_x - \sigma_x) \\ \\ -s_{yx}\dot{\rho}_x - s_{yy}\dot{\rho}_y = V_r(\rho_y - \sigma_y) \end{cases} \tag{11.126}$$

In [8, p. 346] this kind of model is called *nonlinear single point*.

In classical handling analysis, only lateral slips are supposed to be significant. The model becomes simply

$$-s_{yy}\dot{\rho}_y = V_r(\rho_y - \sigma_y) \tag{11.127}$$

11.8.1.2 Transient Linear Tire Model

The simplest version of (11.124) assumes a linear function $\mathbf{F}_t(\boldsymbol{\rho}) = -C_\sigma(\rho_x\,\mathbf{i} + \rho_y\,\mathbf{j})$, like in (11.74). Accordingly, Eq. (11.124) become

$$\begin{aligned} -C_\sigma\dot{\rho}_x &= w_x V_r(\rho_x - \sigma_x) \\ -C_\sigma\dot{\rho}_y &= w_y V_r(\rho_y - \sigma_y) \end{aligned} \tag{11.128}$$

often conveniently rewritten as

$$\begin{aligned} s_x\dot{\rho}_x + V_r\rho_x &= V_r\sigma_x \\ s_y\dot{\rho}_y + V_r\rho_y &= V_r\sigma_y \end{aligned} \tag{11.129}$$

where the positive constants

$$s_x = \frac{C_\sigma}{w_x} \qquad \text{and} \qquad s_y = \frac{C_\sigma}{w_y} \tag{11.130}$$

are called, respectively, longitudinal and lateral *relaxation lengths*. With the data listed in (11.49), we have $s_x = a$ and $s_y = 4a$: as expected the lateral relaxation length is much higher than the longitudinal one. The two equations in (11.129) are now uncoupled, which simplifies further this model, called *linear single point*.

If we compare the linear and the non linear single point models, we see that $s_x \geq s_{xx}$ and $s_y \geq s_{yy}$.

Consistently with the assumption of linear tire behavior, inserting $\mathbf{F}_t = -C_\sigma\boldsymbol{\rho}$ into (11.129) leads to the most classical *transient linear tire model* ($i = x, y$)

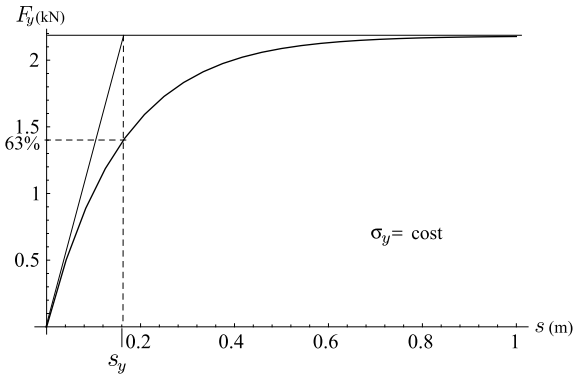

Fig. 11.54 Lateral force asymptotic response to a step change of σ_y and measurement of the relaxation length s_y

$$s_i \dot{F}_i + V_r(t) F_i = -V_r(t) C_\sigma \sigma_i(t) \tag{11.131}$$

that is, to nonhomogeneous linear first-order differential equations [5]. It is worth noting that (11.129) and (11.131) are perfectly equivalent.

The simplest, canonical, case is with *constant* V_r, which makes the equations with *constant* coefficients. The homogeneous counterpart of (11.131) has solution

$$F_i^{\,O}(t) = \mathscr{A} \mathrm{e}^{-\frac{V_r}{s_i} t} \tag{11.132}$$

If also σ_i is *constant*, a particular solution F_i^p is simply

$$F_i^p = -C_\sigma \sigma_i \tag{11.133}$$

Therefore, in this case the general solution of (11.131), with initial condition $F_i(0) = 0$, is

$$F_i(t) = F_i^{\,O}(t) + F_i^p = -C_\sigma \sigma_i \left(1 - \mathrm{e}^{-\frac{V_r}{s_i} t}\right) \tag{11.134}$$

In Fig. 11.54 this solution is plotted using the travel distance $s = V_r t$ instead of time. Also shown is how to experimentally measure the relaxation length. Just take the value of s that makes 63% of the asymptotic value of the force. This is much more reliable than trying to use the tangent in the origin of a noisy experimental signal.

Also interesting is the particular solution if $\sigma_i(t) = \sigma_0 \sin(\omega t)$ (the homogeneous solution decays very rapidly)

$$F_i^p(t) = -\frac{C_\sigma \sigma_0}{\sqrt{1 + (\omega s_i / V_r)^2}} \sin\left(\omega t - \arctan(\omega s_i / V_r)\right) \tag{11.135}$$

It is worth noting how the term $\omega s_i / V_r$ affects both the amplitude (reducing it) and the phase shift. The tire force is delayed with respect to the sinusoidal input.

However, this completely linear model provides acceptable results only if the tire slips are very small. An alternative, a little better approach is presented hereafter.

11.8.1.3 Transient Semi-Nonlinear Tire Model

It is very common in vehicle dynamics to combine the linear equations (11.129) for $\boldsymbol{\rho}(t)$ with a nonlinear function for the tangential force, like, e.g., $\mathbf{F}_t = -(\boldsymbol{\rho}/\rho)F_t(\rho)$, as in (11.122). Things are a bit mixed up, but the allure of simplicity is quite powerful. Indeed, the differential equations in (11.124) are much more involved than those in (11.129), while combining (11.124) with a nonlinear function for $\mathbf{F}_t$ is fairly straightforward. In [8, p. 345] this kind of model is called *semi-nonlinear single point*.

Results are much more realistic than those provided by the linear model.

11.8.2 Transient Model with Carcass and *Tread Compliance*

If the carcass and tread stiffnesses are comparable, that is if (11.117) does not hold, the effects of $\mathbf{e}_{,t}$ should also be taken into account, particularly under severe transient conditions. Therefore, both conditions listed at p. 478 are relaxed, that is:

- $\mathbf{e}_{,t} \neq \mathbf{0}$;
- $\dot{\mathbf{q}} \neq \mathbf{0}$.

To keep the formulation rather simple, while still grasping the main phenomena, it is useful to work under the following simplifying assumptions:

1. rectangular shape of the contact patch, which means $x_0(\hat{y}) = a$;
2. no spin slip φ;
3. either pure longitudinal slip σ_x or pure lateral slip σ_y, but not both;
4. $\mu_0 = \mu_1$, that is both equal to μ.

It is worth noting that complete adhesion in the contact patch is *not* assumed (cf. [8, p. 220]). Like in Sect. 11.2, boundary conditions at the leading edge and initial conditions on the whole contact patch need to be supplied, that is

$$\mathbf{e}(a, \hat{y}, t) = 0, \qquad \text{and} \qquad \mathbf{e}(\hat{x}, \hat{y}, 0) = \mathbf{0} \tag{11.136}$$

Nonzero initial conditions are possible, but may lead to more involved formulations.

Like in Sect. 11.5.1, the first two simplifying assumptions (rectangular shape and no φ), along with zero initial conditions, make $\mathbf{e}$, and actually the whole formulation, *not dependent* on $\hat{y}$. That means that we have to deal with ordinary differential equations, instead of partial differential equations. The additional effect of the third assumption ($\sigma_x \sigma_y = 0$) is to have $\boldsymbol{\rho}(t)$, $\mathbf{q}$, and $\mathbf{e}(\hat{x}, t)$ with only one nonzero component (i.e., directed like either $\mathbf{i}$ or $\mathbf{j}$). That means that we have to deal with scalar

functions, not vectorial functions. The fourth assumption ($\Delta\mu = 0$) makes all function continuous.

With $\varphi = 0$, the first general governing equation (11.39) (adhesion region) becomes

$$V_r \mathbf{e}_{,\hat{x}} - \mathbf{e}_{,t} = V_r \boldsymbol{\rho} \tag{11.137}$$

which is a nonhomogeneous transport equation in the unknown function $\mathbf{e}(\hat{x}, t) = \mathbf{e}_a(\hat{x}, t)$. The tangential stress in the adhesion region is given by $\mathbf{t}_a(\hat{x}, t) = k\mathbf{e}_a$.

The adhesion state starts at the leading edge $\hat{x} = a$ and is maintained up to $\hat{x} = \hat{x}_s(t)$, which marks, at time t, the moving point where the friction limit is reached

$$k|\mathbf{e}_a(\hat{x}_s(t), t)| = \mu p(\hat{x}_s(t)) \tag{11.138}$$

and hence where the sliding region begins.

Exactly like in (11.93), the onset of sliding is with the bristle deflection that has the *same direction* as $\mathbf{e}_a(\hat{x}_s(t), t)$. Therefore, the governing equation (11.40) for the *sliding* region becomes simply

$$\mathbf{t}_s(\hat{x}) = k\mathbf{e}_s(\hat{x}) = \mu p(\hat{x}) \frac{\mathbf{e}_a(\hat{x}_s(t), t)}{|\mathbf{e}_a(\hat{x}_s(t), t)|}, \qquad \text{with } -a \le \hat{x} < \hat{x}_s(t) \tag{11.139}$$

which is already the definition of $\mathbf{e}_s$ and hence of $\mathbf{t}_s$. It is important to note that in the sliding region the bristle deflections $\mathbf{e}_s$ *do not depend on time* and, therefore, are *known*. It is the *moving transition point* $\hat{x}_s(t)$ that has to be found as a function of time.

The global tangential force $\mathbf{F}_t(t) = F_x\,\mathbf{i} + F_y\,\mathbf{j}$ that the road applies to the tire model is given by the integral of $\mathbf{t} = k\mathbf{e}$ on the contact patch, like in (11.69), with all tangential stresses $\mathbf{t}$ having the *same direction*

$$\mathbf{F}_t(t) = -\mathbf{s}\, F_t(t) = k \left[2b \int_{\hat{x}_s(t)}^{a} \mathbf{e}_a(\hat{x}, t) \mathrm{d}\hat{x} + 2b \int_{-a}^{\hat{x}_s(t)} \mathbf{e}_s(\hat{x}) \mathrm{d}\hat{x} \right] \tag{11.140}$$

Since also $\boldsymbol{\rho}(t) = \boldsymbol{\sigma}(t) + \dot{\mathbf{q}}(t)/V_r(t)$ is unknown, an additional equation is necessary. Exactly like in (11.44), it is obtained by differentiating $\mathbf{F}_t(t)$. But here, owing to the simplifying assumptions, some further steps can be carried out,[14] thus getting

$$\begin{aligned} \dot{\mathbf{F}}_t &= 2bk \int_{\hat{x}_s(t)}^{a} \mathbf{e}_{,t} \mathrm{d}\hat{x} = 2bkV_r \int_{\hat{x}_s(t)}^{a} \big(\mathbf{e}_{,\hat{x}} - \boldsymbol{\rho}\big) \mathrm{d}\hat{x} \\ &= 2bkV_r \big[-\mathbf{e}(\hat{x}_s(t), t) - \big(a - \hat{x}_s(t)\big)\boldsymbol{\rho}(t) \big] \end{aligned} \tag{11.141}$$

since $\mathbf{e}(a, t) = 0$. This result can be inserted into (11.45) to get the sought for equation

[14] The crucial aspects are: $\mathbf{e}_s$ not depending on time, $\mathbf{e}_a(\hat{x}_s, t) = \mathbf{e}_s(\hat{x}_s)$.

$$-2bk\big[\mathbf{e}(\hat{x}_s(t),t)+\big(a-\hat{x}_s(t)\big)\boldsymbol{\rho}(t)\big]=\mathbf{W}\big[\boldsymbol{\rho}(t)-\boldsymbol{\sigma}(t)\big] \tag{11.142}$$

where $\mathbf{W}$ is a diagonal matrix, as in (11.15).

Summing up, the problem is therefore governed by either of the two following (formally identical) systems of differential–algebraic equations, with suitable boundary and initial conditions

$$\begin{cases} V_r\, e_{x,\hat{x}}-e_{x,t}=V_r\rho_x, \quad \hat{x}_s(t)<\hat{x}<a \\ k|e_x(\hat{x}_s(t),t)|=\mu p(\hat{x}_s(t)) \\ \rho_x(t)=\dfrac{w_x\sigma_x(t)-2bk\, e_x(\hat{x}_s(t),t)}{w_x+2bk(a-\hat{x}_s(t))} \\ e_x(a,t)=0 \\ e_x(\hat{x},0)=0 \end{cases} \qquad \begin{cases} V_r\, e_{y,\hat{x}}-e_{y,t}=V_r\rho_y \\ k|e_y(\hat{x}_s(t),t)|=\mu p(\hat{x}_s(t)) \\ \rho_y(t)=\dfrac{w_y\sigma_y(t)-2bk\, e_y(\hat{x}_s(t),t)}{w_y+2bk(a-\hat{x}_s(t))} \\ e_y(a,t)=0 \\ e_y(\hat{x},0)=0 \end{cases} \tag{11.143}$$

where, possibly, $V_r=V_r(t)$. Zero initial conditions imply that

$$\rho_i(0)=\frac{w_i\sigma_i(0)}{w_i+4abk} \tag{11.144}$$

It is quite counterintuitive that if we apply a step function to $\sigma(t)$, we obtain $\rho_i(0)\neq 0$.

This model can be called *nonlinear full contact patch*.

It should be remarked that, unlike the commonly used approaches described in the previous section, the proposed model accounts not only for the transient deformation of the carcass (i.e., $\dot{\mathbf{q}}\neq\mathbf{0}$), but also for the transient behavior of the bristle deflection pattern (i.e., $\mathbf{e}_{,t}\neq\mathbf{0}$). It will be shown that this last effect may be far from negligible in some important cases, particularly in braking/driving wheels. More precisely, the larger any of the ratios

$$\theta_x=\frac{w_x}{k_t} \qquad \theta_y=\frac{w_y}{k_t} \tag{11.145}$$

where $k_t=4abk$ is the tread stiffness, the more relevant the effect of the bristle deflection in that direction. Since $w_x\gg w_y$, the transient behavior in the bristle deflection pattern has more influence when the wheel is subject to time-varying longitudinal slip. For instance, with the data reported on p. 477, we have $\theta_x=1$ and $\theta_y=0.25$. In practical terms, bristle transient pattern has some relevance in ABS systems and also in launch control systems.

11.8.3 Model Comparison

The proposed models for the transient behavior of tires are compared on a few numerical tests. The goal is to show the range of applicability and to warn about employing a model without really understanding its capabilities.

In particular, three models of increasing complexity are compared:

- semi-nonlinear single point, (11.129) with (11.122);
- nonlinear single point, (11.124);
- nonlinear full contact patch, (11.143).

The linear single point model is not considered because of its limitations.

Of course, all the simplifying assumptions listed at the beginning of Sect. 11.8.2 have to be fulfilled. Therefore, tests are performed with the data listed in (11.49), except for $\chi = 0$, and under either pure longitudinal slip or pure lateral slip. Moreover, a *rectangular* contact patch and *parabolic* pressure distribution is assumed.

All models are tested applying step functions to either σ_x or σ_y, the step values being -0.21 and -0.07. In all cases, the index i means either x (longitudinal) or y (lateral) direction.

The *first model* (semi-nonlinear single contact point, Sect. 11.8.1.2) takes into account only the carcass compliance and employs a *constant relaxation length* s_i, with $i = x, y$. This model is by far the most popular model for the transient behavior of tires, if limited to pure lateral conditions. According to (11.129), the model is defined by

$$\begin{cases} s_i \dot{\rho}_i + V_r \rho_i = V_r \sigma_i \\ \rho_i(0) = 0 \end{cases} \tag{11.146}$$

where $s_i = C_\sigma / w_i$, with $C_\sigma = 4ka^2b$ as in (11.81). Once the function $\rho_i(t)$ has been obtained, the global tangential force is given by the nonlinear function

$$F_i(\rho_i) = -C_\sigma \rho_i \left[1 - \frac{|\rho_i|}{\sigma_s} + \frac{1}{3} \left(\frac{\rho_i}{\sigma_s} \right)^2 \right] \tag{11.147}$$

much like in (11.96) with (11.104).

The *second model* (nonlinear single contact point, Sect. 11.8.1) is similar, but employs a *nonconstant relaxation length*, as in (11.124)

$$\begin{cases} -\dfrac{F_i'(\rho_i)}{w_i} \dot{\rho}_i + V_r \rho_i = V_r \sigma_i \\ \rho_i(0) = 0 \end{cases} \tag{11.148}$$

where (cf. (11.105) with $\chi = 0$)

$$F_i'(\rho_i) = -C_\sigma \left[1 - 2\frac{|\rho_i|}{\sigma_s} + \left(\frac{\rho_i}{\sigma_s} \right)^2 \right] \tag{11.149}$$

is the derivative of (11.147). A numerical solution is usually required. As in the first model, the function $\rho_i(t)$ is then inserted into (11.147) to obtain the longitudinal/lateral force.

The *third model* (nonlinear full contact patch, Sect. 11.8.2) takes into account both the carcass and tread compliances, as in (11.143)

$$\begin{cases} V_r\, e_{i,\hat{x}} - e_{i,t} = V_r \rho_i \\ k|e_i(\hat{x}_s(t), t)| = \mu p(\hat{x}_s(t)) \\ \rho_i(t) = \dfrac{w_i \sigma_i(t) - 2bk\, e_i(\hat{x}_s(t), t)}{w_i + 2bk(a - \hat{x}_s(t))} \\ e_i(a, t) = 0 \\ e_i(\hat{x}, 0) = 0 \end{cases} \tag{11.150}$$

To obtain a numerical solution, an iterative method can be employed. First make an initial guess for $\rho_i^{(0)}(t)$ (for instance $\rho_i^{(0)}(t) = (\sigma_i(t) + \rho_i^s(t))/2$, where $\rho_i^s(t)$ is the solution of (11.146)). By means of the first equation, numerically obtain $e_x^{(0)}(\hat{x}, t)$, and then, using the second equation, evaluate the function $\hat{x}_s^{(0)}$. At this stage, the first iteration can be completed by computing $\rho_i^{(1)}(t)$ by means of the third equation. The whole procedure has to be repeated (usually 5 to 15 times) until convergence is attained.

Once a good approximation of $e_i(\hat{x}, t)$ and $\hat{x}_s(t)$ (and also of $\rho_i(t)$) has been computed, the tangential force can be obtained from the following integral over the contact patch

$$F_i(t) = 2bk \left[\int_{\hat{x}_s(t)}^{a} e_i(\hat{x}, t) \mathrm{d}\hat{x} + \mu\ \mathrm{sign}(e_i(\hat{x}_s(t), t)) \int_{-a}^{\hat{x}_s(t)} p(\hat{x}) \mathrm{d}\hat{x} \right] \tag{11.151}$$

11.8.4 Selection of Tests

A *step change* in the input (forcing) function $\sigma_i(t)$ works well to highlight the differences between the three models. With the data of (11.49), except $\chi = 0$, the static tangential force (11.147) has maximum magnitude for $\sigma = 0.266$. To test the models in both the (almost) linear and nonlinear ranges, a small ($\sigma_i = -0.07$) and a large ($\sigma_i = -0.21$) step have been selected. Since $w_x = 4w_y$, both longitudinal and lateral numerical tests are performed.

In all cases, results are plotted versus the rolling distance s, instead of time, thus making $V_r(t)$ irrelevant.

11.8.5 Longitudinal Step Input

The longitudinal force $F_x(s)$, as obtained from the three tire models with step inputs $\sigma_x = -0.07$ and $\sigma_x = -0.21$, is shown in Fig. 11.55. Because of the high value of

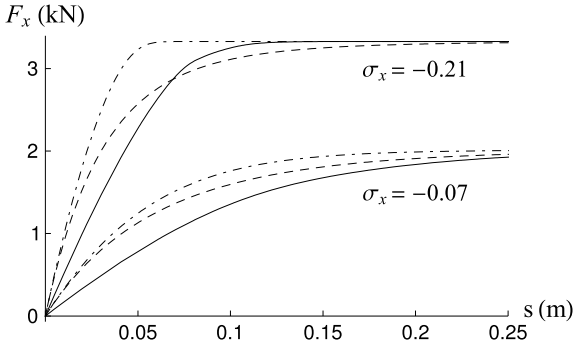

Fig. 11.55 Longitudinal force asymptotic response to a small and to a large step change of σ_x. Comparison of three tire models: semi-nonlinear single contact point (*dashed line*), nonlinear single contact point (*dot-dashed line*), nonlinear full contact patch (*solid line*)

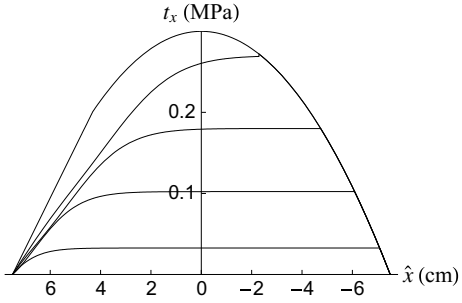

Fig. 11.56 Transient patterns of the tangential stress t_x in the contact patch (third model)

the longitudinal carcass stiffness w_x (equal to the tread stiffness k_t), the transient phenomenon is quite fast. Indeed, in the first model (*dashed line*) the relaxation length $s_x = 7.5\,\text{cm}$.

Quite remarkably, the three models provide very different results for $s < 0.25\,\text{cm}$, thus showing that the selection of the transient tire model may be a crucial aspect in vehicle dynamics, particularly when considering vehicles equipped with ABS.

Obviously, all models converge to the same asymptotic (i.e, steady-state) value of F_x.

The behavior of the first model (*dashed lines*) is the same in both cases, except for a vertical scaling. This is not the case for the second model (*dot-dashed lines*) because of the nonconstant generalized relaxation length. The more detailed third model (*solid lines*) behaves in quite a peculiar way, thus confirming that the contribution of the transient tread deflection is far from negligible.

Figure 11.56 shows the transient pattern of the tangential longitudinal stress t_x in the contact patch as provided by the third model with $\sigma_x = -0.21$. It is worth noting how greatly, in the adhesion region, the pattern departs from the linear behavior of the static case (Fig. 11.16).

11.8.6 Lateral Step Input

The lateral force $F_y(s)$, as obtained from the three tire models with step inputs $\sigma_y = -0.07$ and $\sigma_y = -0.21$, is shown in Fig. 11.57. Because of the low value of the lateral carcass stiffness w_y (equal to one fourth of the tread stiffness k_t), the transient phenomenon is not as fast as in the longitudinal case. Indeed, in the first model the relaxation length $s_y = 30\,\text{cm}$.

In this case, the three models provide not very different results in the linear range, that is with $\sigma_y = -0.07$, while they depart significantly from each other in the nonlinear range, that is with $\sigma_y = -0.21$. Therefore, the selection of the transient tire model may be crucial in lateral dynamics as well.

It should be observed from Figs. 11.55 and 11.57 that the first and second models have the same "formal" behavior. Therefore, changing the carcass stiffness results only in a horizontal scaling. This is not true for the third model.

Obviously, all models converge to the same asymptotic (i.e, steady-state) value of F_y.

Figure 11.58 shows the transient pattern of the tangential lateral stress in the contact patch as provided by the third model with $\sigma_y = -0.21$. There are still differences with respect to the static case, although not as much as in Fig. 11.56.

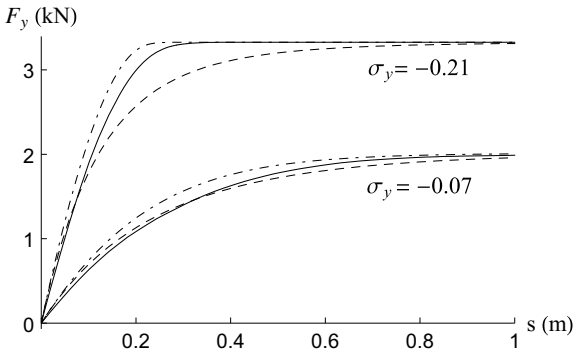

Fig. 11.57 Lateral force asymptotic response to a small and to a large step changes of σ_y. Comparison of three tire models: semi-nonlinear single contact point (*dashed line*), nonlinear single contact point (*dot-dashed line*), nonlinear full contact patch (*solid line*)

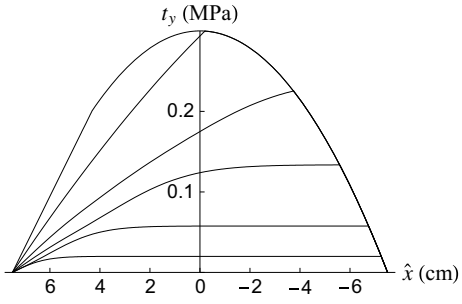

Fig. 11.58 Transient patterns of the tangential stress t_y in the contact patch (third model)

11.9 Exercises

11.9.1 Braking or Driving?

Figure 11.1 shows a schematic of the brush model. Is it braking or driving? Explain why.

Solution

It is obviously braking because all bristles are deflected backward. It is braking pretty much like in Fig. 11.17b: the sliding part is about 1/3 of the footprint.

11.9.2 Carcass Compliance

Do you expect the tire carcass to be more compliant in the longitudinal or in the lateral direction?

Solution

It is quite intuitive that it is more compliant in the lateral direction, at least in road tires (Fig. 11.7).

11.9.3 Brush Model: Local, Linear, Isotropic, Homogeneous

To which of these four properties does the brush model owe its name?

Solution

The answer is "local". Indeed, this is the main simplification. Not very realistic, but dramatically important to keep the model formulation amenable to an almost analytic treatment.

11.9.4 Anisotropic Brush Model

Assuming, as in (11.20), the same tread stiffness k in both longitudinal and lateral directions may be not always correct. Try to figure out how to generalize the brush model to have different stiffnesses.

Solution

The solution is already in (11.21). Just replace any occurrence of $k\mathbf{e}$ with $K\mathbf{e}$, maybe with K being diagonal. Particularly important is to upgrade the comments around (11.93). Even under pure translational slip the transition from adhesion to sliding involves a change in the direction of the bristle deflections, as governed by (11.54).

11.9.5 Carcass Compliance 2

Does the carcass compliance affect the mechanical behavior of tire under steady-state conditions?

Solution

Well, yes and no. In this model the tangential force is not affected by the carcass compliance. On the other hand, the moments with respect to the origin O of the reference system S_w (Fig. 2.6) does indeed depend also on the carcass compliance, as shown in Fig. 11.34.

11.9.6 Skating Versus Sliding

What is the difference between skating velocity and sliding velocity?

Solution

Let us consider a bristle in the tire brush model. The *skating* velocity is the velocity of its *root* with respect to the ground. The *sliding* velocity is the velocity of its *tip* with respect to the ground.

11.9.7 Skating Slip

Is the skating slip ε local or global?

Solution

The skating slip is, in general, a local quantity. It becomes global if the is no spin slip φ. Moreover, we can observe that ε is a transient slip, since it takes into account also $\dot{\mathbf{q}}$.

11.9.8 Simplest Brush Model

Select the options to have the simplest brush model.

Solution

A fairly simple brush model is obtained with the following options (Fig. 11.14):

footprint shape: rectangular;
slips: translational;
working condition: steady-state.

11.9.9 Velocity Relationships

Find out under which operating conditions the following equations hold true:

1. $\mathbf{V}_D = \mathbf{V}_C$;
2. $\mathbf{V}_s^P = \mathbf{V}_s$;
3. $\mathbf{V}_s^P = -\dot{\mathbf{e}}$
4. $\boldsymbol{\rho} = \boldsymbol{\sigma} + \frac{\dot{\mathbf{q}}}{V_r}$;
5. $\boldsymbol{\varepsilon} = \boldsymbol{\rho}$;
6. $\mathbf{V}_s^P = \boldsymbol{\varepsilon} V_r$;
7. $\mathbf{V}_s^P = \boldsymbol{\sigma} V_r$;
8. $\mathbf{V}_s = \boldsymbol{\sigma} V_r$.

Solution

1. $\dot{\mathbf{q}} = \mathbf{0}$;
2. $\dot{\mathbf{q}} = \mathbf{0}$ and $\omega_{s_z} = 0$;
3. adhesion region;
4. always;
5. $\varphi = 0$;
6. always;
7. $\dot{\mathbf{q}} = \mathbf{0}$ and $\varphi = 0$;
8. always.

11.9.10 Slip Stiffness Reduction

Figure 11.27 shows the effects of the combined action of σ_x and σ_y on F_x and F_y. *According to* (11.113) *and with the data in* (11.49), *evaluate the reduction of the slip stiffness* C_σ *(i.e., the slope in the origin) under the combined working conditions of Fig.* 11.27.

Solution

We know from p. 499 that in this case $\sigma_s = 0.27$. Moreover, we have $\chi = 0.2$. It is a simple calculation to find that $\widetilde{C}_\sigma(0.05) = 0.80\, C_\sigma$, $\widetilde{C}_\sigma(0.1) = 0.63\, C_\sigma$, $\widetilde{C}_\sigma(0.2) = 0.38\, C_\sigma$. These results show how strong is the interaction between σ_x and σ_y.

Let us do the same calculation, but with $\chi = 0.1$. First we observe that σ_s does not change. The results are as follows: $\widetilde{C}_\sigma(0.05) = 0.81\, C_\sigma$, $\widetilde{C}_\sigma(0.1) = 0.65\, C_\sigma$, $\widetilde{C}_\sigma(0.2) = 0.41\, C_\sigma$. Not a big difference.

11.9.11 Total Sliding

Can a non-locked wheel have all bristle tips sliding on the road surface?

Solution

Yes. Just have a look at Fig. 11.17d.

11.9.12 Spin Slip and Camber Angle

According to Fig. 11.38, obtain the camber angle γ corresponding to spin slip φ equal to -1, -2 and $-3\ \mathrm{m}^{-}1$.

Solution

The camber angles are 14.5, 30.0 and 48.6 degrees, respectively. We see it is slightly non linear.

11.9.13 The Right Amount of Camber

In which Figure it was shown that just a bit of camber can improve the maximum lateral force?

Solution

This topic was addressed in Fig. 11.45. See also Fig. 11.46. In motorcycle tire it is often the other way around: lot of camber and a little of lateral slip to adjust the lateral force to the required value.

11.9.14 Slip Stiffness

Let us consider tires all with the same F_z, p_0 and k. According to (11.81)*, the brush model predicts a lower slip stiffness for wider tires. Elaborate mathematically this concept with reference to Fig.* 11.13

Solution

Tire (a) has a footprint with length $2w$ and width w. Tires (b) and (c) have a footprint with length w and width $2w$. The area of the footprint is the same in all cases. From (11.81) we obtain that the narrower tire has C_σ twice as much as that of the wider tires.

11.10 Summary

In this chapter a relatively simple, yet significant, tire model has been developed. It is basically a brush model, but with some noteworthy additions with respect to more common formulations. For instance, the model takes care of the transient phenomena that occur in the contact patch. A number of figures show the pattern of the local actions within the contact patch (rectangular and elliptical).

11.11 List of Some Relevant Concepts

p. 472 — the skating slip takes into account both transient translational slip and spin slip;
p. 480 — each bristle is undeformed when it enters the contact patch;
p. 491 — the analysis of the steady-state behavior of the brush model is quite simple if there is no spin slip;
p. 499 — full sliding does not imply wheel locking;
p. 505 — the slip angle α is not a good parameter for a neat description of tire mechanics;
p. 509 — tires have to be built in such a way to provide the maximum tangential force in any direction with small slip angles. This is a fundamental requirement for a wheel with tire to have a directional capability;
p. 508 — the tire action surface summarizes the tire characteristics under a constant vertical load;
p. 510 — the tire action surface summarizes the steady-state behavior of a tire;
p. 515 — good wheel directional capability means small slip angles.

11.12 Key Symbols

a	longitudinal semiaxis of the contact patch
b	lateral semiaxis of the contact patch
C	point of virtual contact
C_γ	camber stiffness
C_σ	slip stiffness
C_φ	spin stiffness
D	center of the contact patch
$\mathbf{e}$	bristle deflection
$\mathbf{e}_a$	bristle deflection in the adhesion zone
$\mathbf{e}_s$	bristle deflection in the sliding zone
$\mathbf{F}_t$	tangential force
F_x	longitudinal component of $\mathbf{F}_t$
F_y	lateral component of $\mathbf{F}_t$
F_z	vertical load
k	bristle stiffness
M_z^D	vertical moment with respect to D
O	origin of the reference system
p	pressure
p_0	pressure peak value
$\mathbf{q}$	horizontal deformation of the carcass
q_x, q_y	components of $\mathbf{q}$
r_r	rolling radius
s_x, s_y	components of the relaxation length
$\mathbf{t}$	tangential stress
$\mathbf{V}_c$	travel velocity
$\mathbf{V}_r$	rolling velocity
$\mathbf{V}_s$	slip velocity
$\mathbf{V}_s^P$	skating velocity
$\mathbf{V}_\mu^P$	sliding velocity
w_x, w_y	carcass stiffnesses
α	slip angle
γ	camber angle
$\boldsymbol{\varepsilon}$	skating slip
ε_r	camber reduction factor
$\boldsymbol{\lambda}$	steady-state skating slip
μ	local friction coefficient
μ_0	coefficient of static friction
μ_1	coefficient of kinetic friction
$\boldsymbol{\rho}$	transient translational slip
$\boldsymbol{\sigma}$	theoretical slip vector
φ	spin slip
ω_{s_z}	slip yaw rate

References

1. Clark SK (ed) (1971) Mechanics of pneumatic tires. National Bureau of Standards, Washington
2. Deur J, Asgari J, Hrovat D (2004) A 3D brush-type dynamic tire friction model. Veh Syst Dyn 42:133–173
3. Deur J, Ivanovic V, Troulis M, Miano C, Hrovat D, Asgari J (2005) Extension of the LuGre tyre friction model related to variable slip speed along the contact patch length. Veh Syst Dyn 43(Supplement):508–524
4. Hüsemann T (2007) Tire technology: simulation and testing. Technical report, Institut für Kraftfahrwesen, Aachen, Vehicle: www.ika.rwth-aachen.de/lehre/kfz-labor/2_tires_en.pdf
5. Kreyszig E (1999) Advanced Engineering Mathematics, 8th edn. John Wiley & Sons, New York
6. Lugner P, Pacejka H, Plöchl M (2005) Recent advances in tyre models and testing procedures. Veh Syst Dyn 43:413–436
7. Milliken WF, Milliken DL (1995) Race Car Veh Dyn. SAE International, Warrendale
8. Pacejka HB (2002) Tyre and vehicle dynamics. Butterworth-Heinemann, Oxford
9. Pacejka HB, Sharp RS (1991) Shear force development by pneumatic tyres in steady state conditions: a review of modelling aspects. Veh Syst Dyn 20:121–176
10. Savaresi SM, Tanelli M (2010) Active braking control systems design for vehicles. Springer, London
11. Truesdell C, Rajagopal KR (2000) An introduction to the mechanics of fluids. Birkhäuser, Boston
12. Zwillinger D (ed) (1996) CRC standard mathematical tables and formulae, 30th edn. CRC Press, Boca Raton